Geochemistry & Stratigraphy of the Mesozoic & Cenozoic Sedimentary Rocks Encountered in the Mandawa Basin, South Eastern Tanzania

Volume 2 of 2

Ross McCabe

Degree of Doctor of Philosophy

University of Dublin, Trinity College

Supervisor: Dr Christopher Nicholas

Submitted to the University of Dublin, Trinity College,

2021

Table of Contents

TABLE OF CONTENTS ..... **II**
LIST OF FIGURES ..... **III**
LIST OF TABLES ..... **XI**
APPENDIX 1: DIGITAL INFORMATION & DATA **1**
APPENDIX 2: TECHNICAL DISCUSSION OF ANALYTICAL METHODOLOGIES EMPLOYED IN THIS THESIS **4**
A2.1. INDUCTIVELY-COUPLED PLASMA ANALYSIS 5
A2.2. PYROLYSIS 12
A2.3. RAMAN SPECTROSCOPY 23
APPENDIX 3: CHARACTERISATION & / OR CORRELATION OF TDP CORES OVER KEY CHEMOSTRATIGRAPHIC BOUNDARIES **39**
APPENDIX 4: CHEMOSTRATIGRAPHIC SUMMARY PANELS OF THE DEEP TEST WELLS **46**
APPENDIX 5: PER-TRANSECT BINARY DIAGRAMS DISTINGUISHING THE CHEMOSTRATIGRAPHIC SEQUENCES AND PACKAGES OF THE MANDAWA BASIN OUTCROP SAMPLES **51**
APPENDIX 6: RECOGNISING REDOX STATES AND POTENTIAL ORGANIC MATTER-RICH SEDIMENTS IN THE MANDAWA BASIN USING INORGANIC GEOCHEMICAL DATA **107**
REFERENCES **125**

List of Figures

Figure A2.1: Atomic absorption and atomic emission of a magnesium electron.

Figure A2.2: Schematic representation of an ICP OES instrument.

Figure A2.3: Schematic representation of an ICP MS instrument.

Figure A2.4: Schematic representation of a Rock Eval 6 instrument (after Lafarge *et al.*, 1998).

Figure A2.5: Diagram depicting the different fractions of the total organic matter of rocks analysed, the corresponding parameters and their recordings (after Lafarge *et al.*, 1998).

Figure A2.6: Pyrogram for sample 315m in well Mbuo-1.

Figure A2.7: Photographs of selected cuttings samples from wells Mbuo-1, Mihambia-1, and Mita Gamma-1.

Figure A3.1: The Sequence EC - MLC chemostratigraphic boundary picked in TDP-40A.

Figure A3.2: The Sequence MLC - Pg chemostratigraphic boundary picked within TDP-37.

Figure A3.3: The Sequence Pg - LPg-Ng chemostratigraphic boundary picked between TDP-12 and TDP-1.

Figure A3.4: The Package MLC1 - MLC2 chemostratigraphic boundary picked within TDP-23.

Figure A3.5: The Package Pg1 - Pg2 chemostratigraphic boundary picked within TDP-14.

Figure A3.6: The Package Pg2 - Pg3 chemostratigraphic boundary picked between TDP-2 and TDP-3.

Figure A3.7: The Package Pg3 - Pg4 chemostratigraphic boundary picked within TDP-12.

Figure A4.1: Chemostratigraphic characterisation summary of well Mbuo-1.

Figure A4.2: Chemostratigraphic characterisation summary of well Mihambia-1.

Figure A4.3: Chemostratigraphic characterisation summary of well Kizimbani-1.

Figure A4.4: Chemostratigraphic characterisation summary of well Mita Gamma-1.

Figure A5.1: Claystone and sandstone-based binary diagrams distinguishing the chemostratigraphic sequences encountered at outcrop along North Mandawa Transect-1: samples colour coded by the lithostratigraphic assignment of Hudson (2010).

Figure A5.2: Claystone and sandstone-based binary diagrams distinguishing the chemostratigraphic sequences encountered at outcrop along North Mandawa Transect-1: samples colour coded by the chemostratigraphic assignment made in this thesis.

Figure A5.3: Claystone-based binary diagrams distinguishing the chemostratigraphic sequences encountered at outcrop along North Mandawa Transect-2: samples colour coded by the lithostratigraphic assignment of Hudson (2010).

Figure A5.4: Claystone-based binary diagrams distinguishing the chemostratigraphic sequences encountered at outcrop along North Mandawa Transect-2: samples colour coded by the chemostratigraphic assignment made in this thesis.

Figure A5.5: Sandstone-based binary diagram distinguishing the chemostratigraphic sequences encountered at outcrop along North Mandawa Transect-2: samples colour coded by the lithostratigraphic assignment of Hudson (2010) and chemostratigraphic assignment made in this thesis.

Figure A5.6: Claystone-based binary diagrams distinguishing the chemostratigraphic sequences encountered at outcrop along North Mandawa Transect-3: samples colour coded by the lithostratigraphic assignment of Hudson (2010).

Figure A5.7: Claystone-based binary diagrams distinguishing the chemostratigraphic sequences encountered at outcrop along North Mandawa Transect-3: samples colour coded by the chemostratigraphic assignment made in this thesis.

Figure A5.8: Sandstone-based binary diagram distinguishing the chemostratigraphic sequences encountered at outcrop along North Mandawa Transect-3: samples colour coded by the lithostratigraphic assignment of Hudson (2010) and chemostratigraphic assignment made in this thesis.

Figure A5.9: Claystone-based binary diagrams distinguishing the chemostratigraphic sequences encountered at outcrop along South Mandawa Transect-1: samples colour coded by the lithostratigraphic assignment of Hudson (2010).

Figure A5.10: Claystone-based binary diagrams distinguishing the chemostratigraphic sequences encountered at outcrop along South Mandawa Transect-1: samples colour coded by the chemostratigraphic assignment made in this thesis.

Figure A5.11: Sandstone-based binary diagram distinguishing the chemostratigraphic sequences encountered at outcrop along South Mandawa Transect-1: samples colour coded by the lithostratigraphic assignment of Hudson (2010) and chemostratigraphic assignment made in this thesis.

Figure A5.12: Claystone-based binary diagrams distinguishing the chemostratigraphic sequences encountered at outcrop along South Mandawa Transect-2: samples colour coded by the lithostratigraphic assignment of Hudson (2010).

Figure A5.13: Claystone-based binary diagrams distinguishing the chemostratigraphic sequences encountered at outcrop along South Mandawa Transect-2: samples colour coded by the chemostratigraphic assignment made in this thesis.

Figure A5.14: Sandstone-based binary diagram distinguishing the chemostratigraphic sequences encountered at outcrop along South Mandawa Transect-2: samples colour coded by the lithostratigraphic assignment of Hudson (2010) and chemostratigraphic assignment made in this thesis.

Figure A5.15: Claystone-based binary diagrams distinguishing the chemostratigraphic sequences encountered at outcrop along South Mandawa Transect-3: samples colour coded by the lithostratigraphic assignment of Hudson (2010).

Figure A5.16: Claystone-based binary diagrams distinguishing the chemostratigraphic sequences encountered at outcrop along South Mandawa Transect-3: samples colour coded by the chemostratigraphic assignment made in this thesis.

Figure A5.17: Sandstone-based binary diagram distinguishing the chemostratigraphic sequences encountered at outcrop along South Mandawa Transect-3: samples colour coded by the lithostratigraphic assignment of Hudson (2010) and chemostratigraphic assignment made in this thesis.

Figure A5.18: Claystone-based binary diagrams distinguishing the chemostratigraphic sequences encountered at outcrop along South Mandawa Transect-4: samples colour coded by the lithostratigraphic assignment of Hudson (2010).

Figure A5.19: Claystone-based binary diagrams distinguishing the chemostratigraphic sequences encountered at outcrop along South Mandawa Transect-4: samples colour coded by the chemostratigraphic assignment made in this thesis.

Figure A5.20: Sandstone-based binary diagram distinguishing the chemostratigraphic sequences encountered at outcrop along South Mandawa Transect-4: samples colour coded by the lithostratigraphic assignment of Hudson (2010) and chemostratigraphic assignment made in this thesis.

Figure A5.21: Claystone-based binary diagrams distinguishing the chemostratigraphic sequences encountered at outcrop along South Mandawa Transect-5: samples colour coded by the lithostratigraphic assignment of Hudson (2010).

Figure A5.22: Claystone-based binary diagrams distinguishing the chemostratigraphic sequences encountered at outcrop along South Mandawa Transect-5: samples colour coded by the chemostratigraphic assignment made in this thesis.

Figure A5.23: Sandstone-based binary diagram distinguishing the chemostratigraphic sequences encountered at outcrop along South Mandawa Transect-5: samples colour coded by the lithostratigraphic assignment of Hudson (2010) and chemostratigraphic assignment made in this thesis.

Figure A5.24: Claystone-based binary diagrams distinguishing the chemostratigraphic sequences encountered at outcrop along South Mandawa Transect-6: samples colour coded by the lithostratigraphic assignment of Hudson (2010).

Figure A5.25: Claystone-based binary diagrams distinguishing the chemostratigraphic sequences encountered at outcrop along South Mandawa Transect-6: samples colour coded by the chemostratigraphic assignment made in this thesis.

Figure A5.26: Sandstone-based binary diagram distinguishing the chemostratigraphic sequences encountered at outcrop along South Mandawa Transect-6: samples colour coded by the lithostratigraphic assignment of Hudson (2010) and chemostratigraphic assignment made in this thesis.

Figure A5.27: Claystone-based binary diagrams distinguishing the chemostratigraphic sequences encountered at outcrop along South Mandawa Transect-7: samples colour coded by the lithostratigraphic assignment of Hudson (2010).

Figure A5.28: Claystone-based binary diagrams distinguishing the chemostratigraphic sequences encountered at outcrop along South Mandawa Transect-7: samples colour coded by the chemostratigraphic assignment made in this thesis.

Figure A5.29: Sandstone-based binary diagram distinguishing the chemostratigraphic sequences encountered at outcrop along South Mandawa Transect-7: samples colour coded by the lithostratigraphic assignment of Hudson (2010) and chemostratigraphic assignment made in this thesis.

Figure A5.30: Claystone and sandstone-based binary diagrams distinguishing the chemostratigraphic sequences encountered at outcrop along South Mandawa Transect-8: samples colour coded by the lithostratigraphic assignment of Hudson (2010).

Figure A5.31: Claystone and sandstone-based binary diagrams distinguishing the chemostratigraphic sequences encountered at outcrop along South Mandawa Transect-8: samples colour coded by the chemostratigraphic assignment made in this thesis.

Figure A5.32: Claystone and sandstone-based binary diagrams distinguishing the chemostratigraphic sequences encountered at outcrop along South Mandawa Transect-9: samples colour coded by the lithostratigraphic assignment of Hudson (2010).

Figure A5.33: Claystone and sandstone-based binary diagrams distinguishing the chemostratigraphic sequences encountered at outcrop along South Mandawa Transect-9: samples colour coded by the chemostratigraphic assignment made in this thesis.

Figure A5.34: Claystone and sandstone-based binary diagrams distinguishing the chemostratigraphic sequences encountered at outcrop along South Mandawa Transect-10: samples colour coded by the lithostratigraphic assignment of Hudson (2010).

Figure A5.35: Claystone and sandstone-based binary diagrams distinguishing the chemostratigraphic sequences encountered at outcrop along South Mandawa Transect-10: samples colour coded by the chemostratigraphic assignment made in this thesis.

Figure A5.36: Claystone-based binary diagrams distinguishing the chemostratigraphic sequences encountered at outcrop along South Mandawa Transect-11: samples colour coded by the lithostratigraphic assignment of Hudson (2010).

Figure A5.37: Claystone-based binary diagrams distinguishing the chemostratigraphic sequences encountered at outcrop along South Mandawa Transect-11: samples colour coded by the chemostratigraphic assignment made in this thesis.

Figure A5.38: Sandstone-based binary diagram distinguishing the chemostratigraphic sequences encountered at outcrop along South Mandawa Transect-11: samples colour coded by the lithostratigraphic assignment of Hudson (2010) and chemostratigraphic assignment made in this thesis.

Figure A5.39: Claystone and sandstone-based binary diagrams distinguishing the chemostratigraphic sequences encountered at outcrop along South Mandawa Transect-12: samples colour coded by the lithostratigraphic assignment of Hudson (2010).

Figure A5.40: Claystone and sandstone-based binary diagrams distinguishing the chemostratigraphic sequences encountered at outcrop along South Mandawa Transect-12 samples colour coded by the chemostratigraphic assignment made in this thesis.

Figure A5.41: Claystone-based binary diagrams distinguishing the chemostratigraphic packages encountered at outcrop along North Mandawa Transect-1: samples colour coded by the chemostratigraphic assignment made in this thesis.

Figure A5.42: Claystone-based binary diagrams distinguishing the chemostratigraphic packages encountered at outcrop along North Mandawa Transect-2: samples colour coded by the chemostratigraphic assignment made in this thesis.

Figure A5.43: Claystone-based binary diagrams distinguishing the chemostratigraphic packages encountered at outcrop along North Mandawa Transect-3: samples colour coded by the chemostratigraphic assignment made in this thesis.

Figure A5.44: Claystone-based binary diagrams distinguishing the chemostratigraphic packages encountered at outcrop along South Mandawa Transect-1: samples colour coded by the chemostratigraphic assignment made in this thesis.

Figure A5.45: Claystone-based binary diagrams distinguishing the chemostratigraphic packages encountered at outcrop along South Mandawa Transect-2: samples colour coded by the chemostratigraphic assignment made in this thesis.

Figure A5.46: Claystone-based binary diagrams distinguishing the chemostratigraphic packages encountered at outcrop along South Mandawa Transect-3: samples colour coded by the chemostratigraphic assignment made in this thesis.

Figure A5.47: Claystone-based binary diagrams distinguishing the chemostratigraphic packages encountered at outcrop along South Mandawa Transect-4: samples colour coded by the chemostratigraphic assignment made in this thesis.

Figure A5.48: Claystone-based binary diagrams distinguishing the chemostratigraphic packages encountered at outcrop along South Mandawa Transect-5: samples colour coded by the chemostratigraphic assignment made in this thesis.

Figure A5.49: Claystone-based binary diagrams distinguishing the chemostratigraphic packages encountered at outcrop along South Mandawa Transect-6: samples colour coded by the chemostratigraphic assignment made in this thesis.

Figure A5.50: Claystone-based binary diagrams distinguishing the chemostratigraphic packages encountered at outcrop along South Mandawa Transect-7: samples colour coded by the chemostratigraphic assignment made in this thesis.

Figure A5.51: Claystone-based binary diagrams distinguishing the chemostratigraphic packages encountered at outcrop along South Mandawa Transect-8: samples colour coded by the chemostratigraphic assignment made in this thesis.

Figure A5.52: Claystone-based binary diagrams distinguishing the chemostratigraphic packages encountered at outcrop along South Mandawa Transect-9: samples colour coded by the chemostratigraphic assignment made in this thesis.

Figure A5.53: Claystone-based binary diagrams distinguishing the chemostratigraphic packages encountered at outcrop along South Mandawa Transect-10: samples colour coded by the chemostratigraphic assignment made in this thesis.

Figure A5.54: Claystone-based binary diagrams distinguishing the chemostratigraphic packages encountered at outcrop along South Mandawa Transect-11: samples colour coded by the chemostratigraphic assignment made in this thesis.

Figure A5.55: Claystone-based binary diagrams distinguishing the chemostratigraphic packages encountered at outcrop along South Mandawa Transect-12: samples colour coded by the chemostratigraphic assignment made in this thesis.

Figure A6.1: Per chemostratigraphic sequence Cr vs. Al binary diagrams of the Mandawa Basin claystones.

Figure A6.2: Per chemostratigraphic sequence Mo vs. Al binary diagrams of the Mandawa Basin claystones.

Figure A6.3: Per chemostratigraphic sequence U vs. Al binary diagrams of the Mandawa Basin claystones.

Figure A6.4: Per chemostratigraphic sequence V vs. Al binary diagrams of the Mandawa Basin claystones.

Figure A6.5: Per chemostratigraphic sequence Ni vs. Al binary diagrams of the Mandawa Basin claystones.

Figure A6.6: Per chemostratigraphic sequence Cu vs. Al binary diagrams of the Mandawa Basin claystones.

Figure A6.7: Per chemostratigraphic sequence Cu vs. Al binary diagrams of the Mandawa Basin claystones with all samples with >150ppm Cu removed.

Figure A6.8: Comparison of the average element values calculated from all the Mandawa Basin claystone samples and the average shale values of PAAS and NASC.

Figure A6.9: Per chemostratigraphic sequence EF Mo vs. EF U binary diagrams of the Mandawa Basin claystone.

Figure A6.10: Per chemostratigraphic sequence EF Ni vs. EF Cu binary diagrams of the Mandawa Basin claystones.

List of Tables

Table A2.1: Guideline values for interpreting the type and quality of source rocks from pyrolysis data (after Carvajal-Ortiz & Gentzis, 2015).

Table A2.2: Performance test results of the Rock-Eval 6 instrument at the University of Greenwich using geochemical standards SR-1 and JR-1.

Table A2.3: Counts of all minerals acquired by Raman Spectroscopy on selected TDP cores.

Table A6.1: Per sequence statistical information derived from the EF of Mo, U, Ni and Cu.

APPENDIX 1: DIGITAL INFORMATION & DATA

All digital data and calculations accompany this volume. The data tables include.

Data Sheet A1.1: Details of TDP core samples

Data Sheet A1.2: Inorganic geochemical data and key ratios of TDP-1

Data Sheet A1.3: Inorganic geochemical data and key ratios of TDP-2

Data Sheet A1.4: Inorganic geochemical data and key ratios of TDP-3

Data Sheet A1.5: Inorganic geochemical data and key ratios of TDP-4

Data Sheet A1.6: Inorganic geochemical data and key ratios of TDP-7B

Data Sheet A1.7: Inorganic geochemical data and key ratios of TDP-8

Data Sheet A1.8: Inorganic geochemical data and key ratios of TDP-9

Data Sheet A1.9: Inorganic geochemical data and key ratios of TDP-10

Data Sheet A1.10: Inorganic geochemical data and key ratios of TDP-12

Data Sheet A1.11: Inorganic geochemical data and key ratios of TDP-13

Data Sheet A1.12: Inorganic geochemical data and key ratios of TDP-14

Data Sheet A1.13: Inorganic geochemical data and key ratios of TDP-17

Data Sheet A1.14: Inorganic geochemical data and key ratios of TDP-18

Data Sheet A1.15: Inorganic geochemical data and key ratios of TDP-19

Data Sheet A1.16: Inorganic geochemical data and key ratios of TDP-23

Data Sheet A1.17: Inorganic geochemical data and key ratios of TDP-24A

Data Sheet A1.18: Inorganic geochemical data and key ratios of TDP-31

Data Sheet A1.19: Inorganic geochemical data and key ratios of TDP-37

Data Sheet A1.20: Inorganic geochemical data and key ratios of TDP-39

Data Sheet A1.21: Inorganic geochemical data and key ratios of TDP-40A

Data Sheet A1.22: Kilwa Group chemostratigraphic composite data and key ratios

Data Sheet A1.23: Inorganic geochemical data and key ratios of outcrop samples collected along North Mandawa Transect-1

Data Sheet A1.24: Inorganic geochemical data and key ratios of outcrop samples collected along North Mandawa Transect-2

Data Sheet A1.25: Inorganic geochemical data and key ratios of outcrop samples collected along North Mandawa Transect-3

Data Sheet A1.26: Inorganic geochemical data and key ratios of outcrop samples collected along South Mandawa Transect-1

Data Sheet A1.27: Inorganic geochemical data and key ratios of outcrop samples collected along South Mandawa Transect-2

Data Sheet A1.28: Inorganic geochemical data and key ratios of outcrop samples collected along South Mandawa Transect-3

Data Sheet A1.29: Inorganic geochemical data and key ratios of outcrop samples collected along South Mandawa Transect-4

Data Sheet A1.30: Inorganic geochemical data and key ratios of outcrop samples collected along South Mandawa Transect-5

Data Sheet A1.31: Inorganic geochemical data and key ratios of outcrop samples collected along South Mandawa Transect-6

Data Sheet A1.32: Inorganic geochemical data and key ratios of outcrop samples collected along South Mandawa Transect-7

Data Sheet A1.33: Inorganic geochemical data and key ratios of outcrop samples collected along South Mandawa Transect-8

Data Sheet A1.34: Inorganic geochemical data and key ratios of outcrop samples collected along South Mandawa Transect-9

Data Sheet A1.35: Inorganic geochemical data and key ratios of outcrop samples collected along South Mandawa Transect-10

Data Sheet A1.36: Inorganic geochemical data and key ratios of outcrop samples collected along South Mandawa Transect-11

Data Sheet A1.37: Inorganic geochemical data and key ratios of outcrop samples collected along South Mandawa Transect-12

Data Sheet A1.38: Outcrop sample evaluation matrix table

APPENDIX 2: TECHNICAL DISCUSSION OF ANALYTICAL METHODOLOGIES EMPLOYED IN THIS THESIS

A2.1. INDUCTIVELY-COUPLED PLASMA ANALYSIS

All samples in this study have been subjected to inductively coupled plasma (ICP) optical emission spectroscopy (OES) and mass spectrometry (MS) analysis. When used together, data is acquired for a wide range of elements at low limits of analytical detection.

The ICP OES instrument is capable of determining up to 70 elements with high precision and accuracy, at low limits of analytical detection (to parts per billion: ppb) and in less than two minutes per sample. ICP OES instruments also have a wide dynamic range of up to 5-6 orders of magnitude, which permits the determination of major elements, minor elements and trace elements from a single sample preparation. A detailed discussion of ICP OES is given by Jarvis and Jarvis (1992a 1992b) and summarised here.

The ICP OES instrument excites the electrons of atoms and ions, and measures the energy they release upon reversion to a normal state. In an excited state, electrons absorb energy produced by a plasma source and jump to a higher energy level (electron shell: **Figure A2.1**). Upon reversion to a normal state, the electron jumps back to its original position and, in so doing, releases energy in the form of light (photons) at specific wavelengths and intensities. The number of photon wavelengths and intensities produced during reversion of electrons to a normal state, known as an atomic spectrum, are element-specific and are directly related to the number of electrons that orbit the atom. Depending on the element, the atomic spectrum can be very simple, consisting of only a few wavelengths, to very complex; consisting of tens, or even hundreds of wavelengths.

Figure A2.1. Atomic absorption and atomic emission of a magnesium electron.

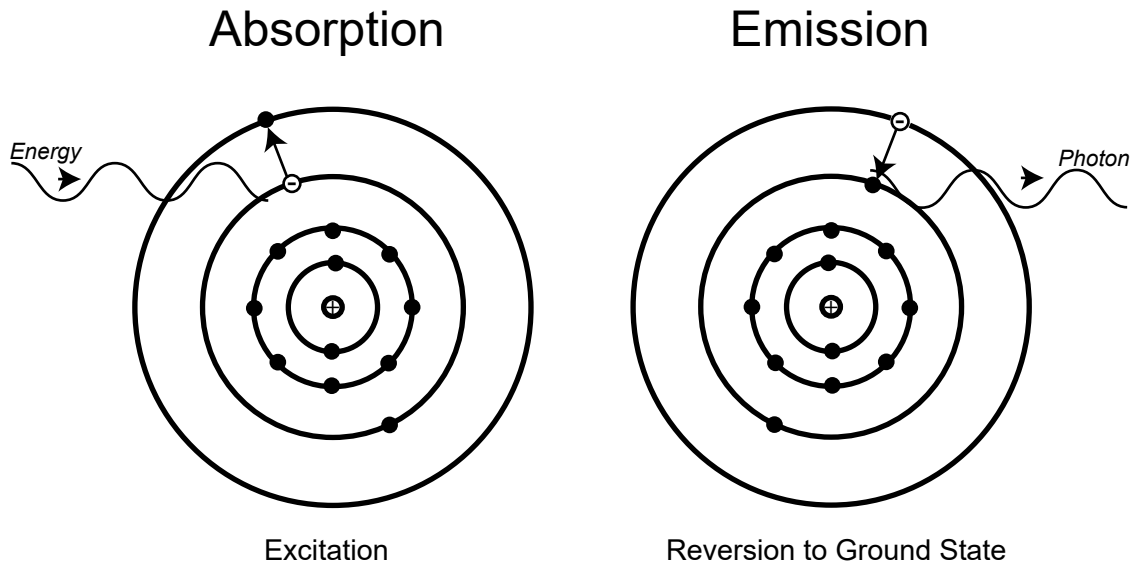

After Jarvis & Jarvis (1992b)

Geological samples are invariably made up of a multitude of elements, the compositions and concentrations of which will vary depending in the rock type and mineralogical composition. The atomic spectrum produced for any given sample therefore, is the combination of wavelengths and intensities of all elements present within it. The abundance of each element in the spectrum is quantified by measuring the intensity of the photons produced at specific wavelengths that are characteristic of that element and comparing them back to standard reference materials (SRMs): samples of a known elemental (and therefore, spectral) composition.

The ICP OES instrument acquires its spectral data from geological material by introducing the sample to the ICP as a solution (**Figure A2.2**). The ways in which the solid sample material can be converted into a solution will be discussed in more detail later in this section. The solution is converted into a fine aerosol in a nebulizer, where it is mixed with argon (Ar) gas and introduced into a spray chamber where the desired finer spray particles (< 10μ) are filtered from the larger particles. The fine aerosol particles are then carried by the Ar gas through a glass torch where they are introduced to the ICP source.

Figure A2.2. Schematic representation of an ICP OES instrument.

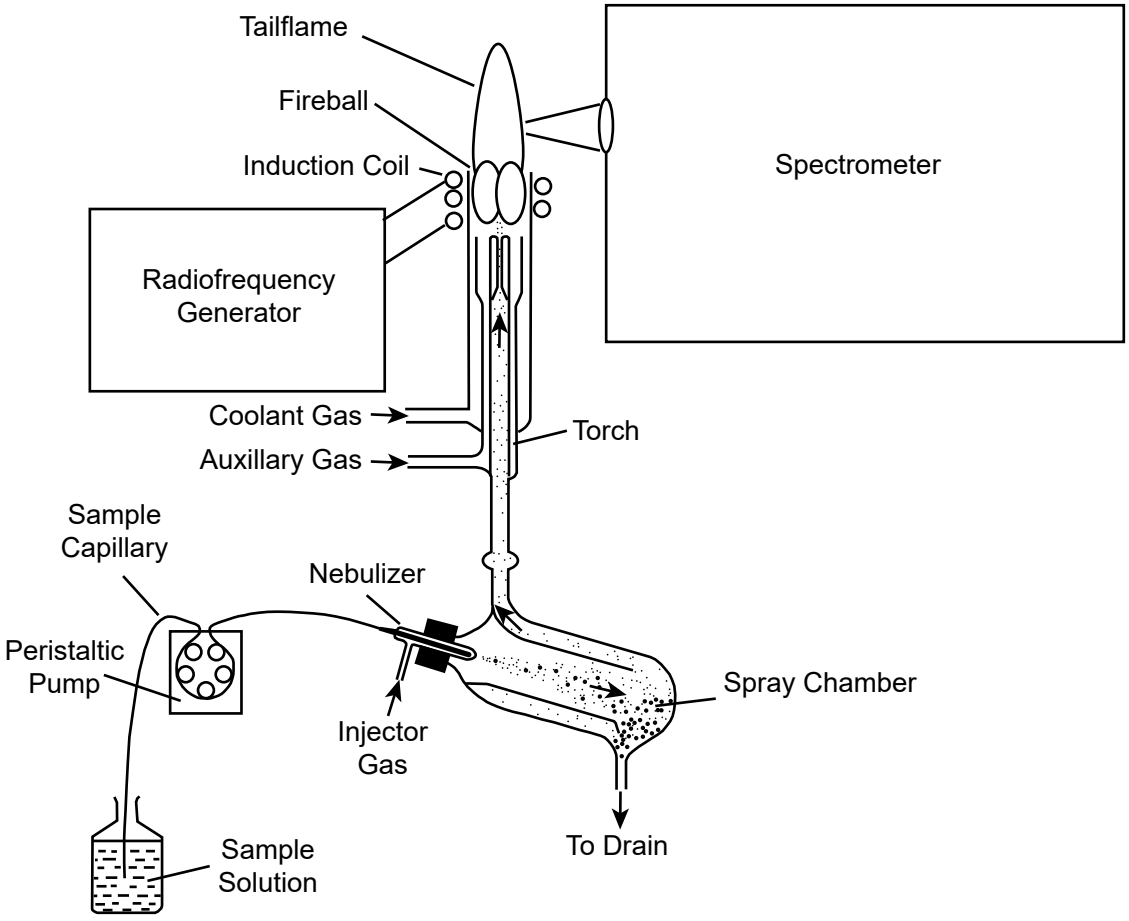

After Jarvis & Jarvis (1992b)

The plasma is generated by oscillating radiofrequency (RF) magnetic fields, induced by a water-cooled copper coil wrapped around the torch, through the Ar gas (Jarvis & Jarvis. 1992b). The plasma is composed of three regions: the fireball, secondary region and tail flame (**Figure A2.2**). The fireball and secondary flame experience the highest temperatures in the plasma (>9726 and 7726°C, respectively) and contain large populations of excited Ar ions. These regions however, are unsuitable as the analytical emission source, as both generate high intensity background radiation that hamper accurate detection of atomic spectra. In contrast, the region of the tail flame experiences lower temperatures (5926 to 6226°C) and so has a low intensity of background electron emissions, which is more suited as being the analytical emission source. It is in the tail flame that the analyte is broken down into its constituent atoms and ions, which then enter into, and revert from, their excited state, producing the characteristic spectra that define each element. Once passed through the ICP, both the wavelengths and their intensities are then measured using a polychromator: a spectrometer that simultaneously detects multiple spectra (**Figure A2.2**).

The ICP MS instrument is also capable of determining almost all elements in the periodic table, with high precision and accuracy, at low limits of analytical detection (to parts per trillion: ppt) and in 3 - 5 minutes per sample Jarvis (1992a 1992b). The ICP MS instrument also has a wide dynamic range of up to 5-6 orders of magnitude and can determine element concentrations from the same solution as used for the ICP-OES.

Rather than measuring photon wavelengths and intensities emitted by atoms and ions, the ICP MS instrument measures the mass of ions produced via the introduction of the sample to a plasma source. The ions are channelled through a quadrupole system within the mass spectrometer (**Figure A2.3**). However, only ions of a particular mass can pass through the quadrupole at any one time. The mass of the ions passing through the quadrupole system can be increased or decreased by modifying the radio frequency and direct current of the quadrupole rods. The abundance of different elements in a sample are therefore quantified by the ICP MS instrument by sweeping through a range of ionic masses during analysis. Compared to OES, MS spectra are simple and spectral peaks for elements are identifiable from mass tables (Jarvis & Jarvis. 1992b).

Figure A2.3. Schematic representation of an ICP MS instrument.

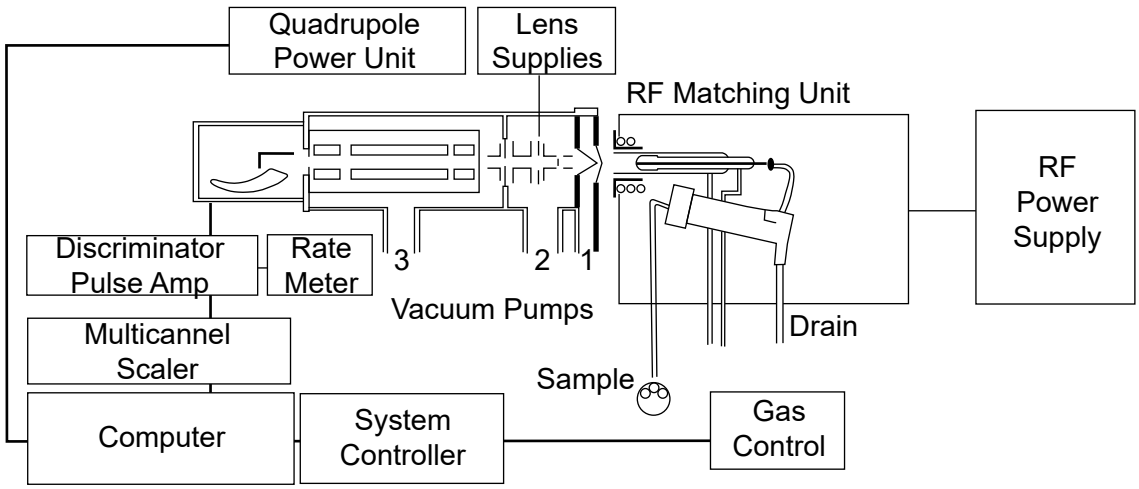

1) Focussing Ion beam using nickel skimmer & a series of electrostatic lenses
2) Ion beam eneters a high vacuum chamber of a quadrupole mass spectrometer
3) Ions are rapidly sorted and counted using an electron multiplier detector

After Jarvis & Jarvis (1992a)

According to Longerich *et al.* (1990), Jarvis (1990), Jarvis & Jarvis (1992a & b) and Kamber (2009), the primary factor limiting elemental detection by ICP OES and MS is sample preparation. By and large, solid material needs to be converted to a solution prior to ICP analysis. This process has the distinct advantage of reducing any heterogeneous material, such as rock samples, into a homogenous mass and thus eliminates any elemental bias caused by matrix/grain size. In this study, approximately 5g of material per sample is ground in an agate mortar, with the resultant powder being employed for both ICP OES & MS analysis. The powder created from outcrop and core samples is dried in an oven at 60ºC for 5 minutes in order to drive off any internal moisture.

Two common methods are employed for sample dissolution: total and partial. Total dissolution requires the complete digestion of the sample material and, by association, all its constituent elements. Total dissolution is a difficult task to achieve. Depending on the dissolution procedure employed, key elements may either not digest completely, or be driven off in a gaseous phase. The two main methods for total dissolution of a sample are acid digestion and alkali fusion. Acid digestion involves dissolving a sample in concentrated nitric acid (HNO_3) and is recommended if volatile phases are to be determined with a high degree of precision and accuracy. However, this may be at the cost of inaccurate determination of elements such as Si, Cr, Hf and Zr that can reside in more resistant mineralogical phases (i.e. zircon and spinel) and thus may not be digested in their entirety. If the accurate determination of elements present in chemically resistant minerals is required, then high temperature fusion of the sample with a lithium metaborate ($LiBO_2$) flux may be the preferred method of dissolution, although this will be achieved at the expense of the volatile phases including S, Cd, Pb, Sn and Zn.

Increasing the volume of material dissolved (i.e., the flux) means that the resultant solution will have to undergo additional dilution to reach levels of 'total dissolved solid' (TDS) that are manageable for the instrument. According to Kamber (2009), modern MS instruments are not tolerant of more than 1‰ TDS. Samples with higher TDS volumes run the risk of clogging the instrument through precipitation of residues on its components and, therefore, hamper accurate elemental detection.

Accurately capturing both the refractory and volatile elements is achievable by applying an acid digestion method to the sample in a sealed high-pressure Teflon-lined 'bomb', although, according to Jarvis and Jarvis (1992b), such techniques are rarely undertaken in commercial laboratories, as they are time and labour intensive.

Partial dissolution involves the isolation and dissolution of specific groups of elements in a sample, rather than all elements. This approach is particularly useful if the requirement is the accurate determination of low abundance trace elements, such as the REEs that suffer greatly from spectral interference from other elements (Jarvis & Jarvis. 1992a&b).

Clearly, no single preparation procedure is suited to the digestion of all sample types or the precise and accurate determination of all elements. Compromises have to be made and the selection of a particular preparation protocol must be made in view of the ultimate objective of any given study. In this study, samples were prepared and analysed by technicians at Origin Analytical Ltd in the UK by applying the alkali fusion procedure largely identical to that described by Jarvis (1990). The procedure involves fusing 0.25g of sample with 1.25g of $LiBO_2$ flux in a carbon crucible at 1050ºC for 15 minutes. The mixture is then immediately transferred into beakers containing 120ml of 3.5%v/v of HNO_3. The alkali fusion procedure is favoured over acid digestion as it allows for total digestion of the more resistant silicate minerals such as zircon, monazite and Ti-oxide heavy minerals. The decision comes at the cost of the more volatile phases such as S.

For ICP-OES analysis, the samples were run on a Thermo ICAP 6500 instrument. For ICP-MS analysis, samples were run on a Thermo XSeries 2 instrument. Both instruments are calibrated using internal rock standards that are matrix matched for both clastic and carbonate lithologies separately. SRMs are run in line with the geological material at 20 sample intervals, allowing for instrumental anomalies and analytical drift to be corrected.

Origin Analytical Ltd acquire data from 26 elements using the ICP-OES instrument. These include ten major and minor elements (Al_2O_3, SiO_2, TiO_2, Fe_2O_3, MnO, MgO, CaO, Na_2O, K_2O, P_2O_5) and sixteen trace elements (Ba, Ce, Cr, Cu. La, Nb, Ni, S, Sc, Sr, Th, V, Y, U, Zn, Zr). Whilst S is determined by ICP-OES analysis, the alkali fusion procedure is likely to have driven a portion of it away as a gaseous phase. As such, Origin Analytical Ltd regard S data as semi-quantitative. Origin Analytical Ltd acquire data from 34 elements using the ICP-MS instrument. These include Ba, Be, Cs, Co, Cr, Cu, Ga, Hf, Mo, Nb, Ni, Rb, Sr, Ta, Th, U, V, Y, Zn, Zr) including fourteen rare earth elements (La, Ce, Pr, Nd, Sm, Eu, Gd, Tb, Dy, Ho, Er, Tm. Yb, Lu). Origin Analytical Ltd quote the precision error for the major element data as being less than 1% to 2% overall and is between c.3% to 5% for the high abundance trace element data.

14 trace elements are reported by both OES and MS. Whilst both sets of elements are regarded as being of good quality in terms of precision and error and certainly fit for purpose, the decision has been made to use the trace element data from the MS and the major elements, minor elements, S and Sc from the OES. In so doing, any potential minor analytical bias between the trace elements is reduced.

A2.2. PYROLYSIS

In nature, organic matter-rich sedimentary rocks go through a maturation process caused by progressive burial-related heating over time to a point at which oil is first expelled from the rock, then gas. Eventually, a geothermal point is reached at which no more hydrocarbons can be expelled. Pyrolysis can be regarded as a laboratory-based technique that mimics the natural heating process that acts on sedimentary rocks and in so doing, the type and abundance of organic compounds present within are determined (Peters, 1986; Lafarge *et al.*, 1998; Peters *et al.*, 2005; Carvajal-Ortiz & Gentzis, 2015).

The analytical methodology for pyrolysis is described in detail by Peters (1986) and modified by Lafarge *et al.* (1998) to take account of improvements in technology in the newer pyrolysis instrument, the Rock Eval 6 (**Figure A2.4**), which is now the industry standard machine. Up to 100mg of a powdered rock sample is heated in two micro ovens. The first oven heats the sample in an inert (Helium or Nitrogen) atmosphere from 100ºC to a constant 300ºC for 3 minutes, followed by a programmed increase in temperature (25ºC/minute) until a temperature of 650ºC is achieved. In the second oven, the sample is heated in oxygen from 400ºC to 850ºC. By the time the maximum temperature is reached, all organic carbon from all kerogen types will have been completely thermally degraded (Lafarge *et al.*, 1998). A flame ionization detector (FID – **Figure A2.4**) senses the organic compounds released from the kerogen as it degrades and infra-red detectors also record the amount of carbon monoxide (CO) and carbon dioxide (CO_2) released from the sample during pyrolysis and oxidation, which are used to determine kerogen types and the amount of mineral carbon (carbonate) present in the sample.

Figure A2.4. Schematic representation of a Rock Eval 6 instrument (after Lafarge *et al.*, 1998).

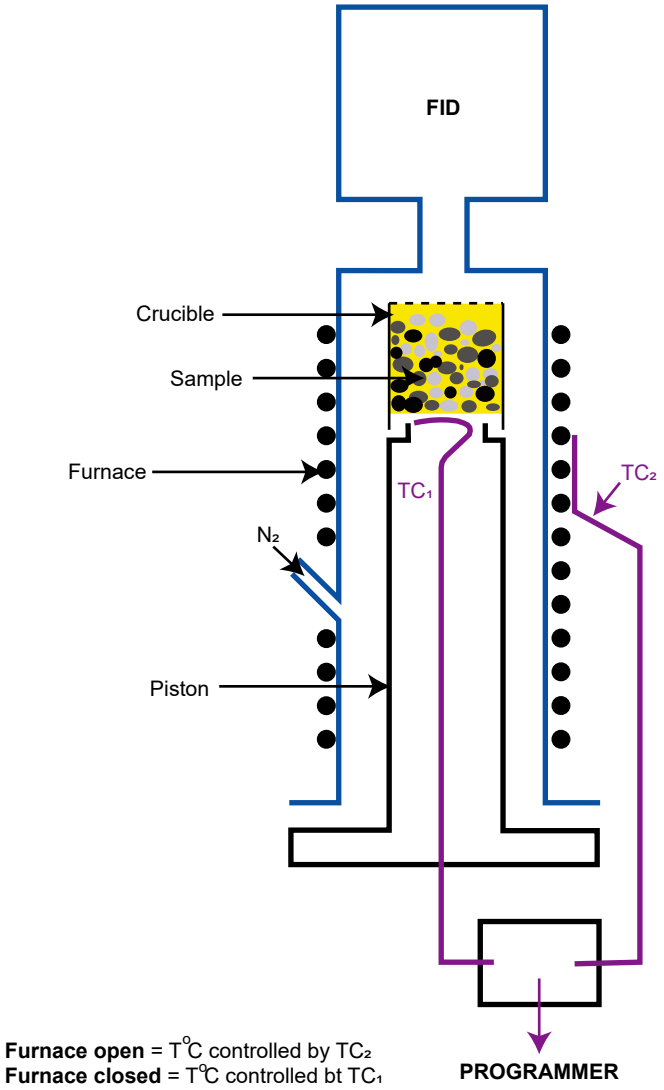

Several key measurements are taken during pyrolysis: the S1, S2, S3 and S4 peaks and the T_{max} peak (Peters, 1986; Lafarge *et al.*, 1998 – **Figure A2.5**), all of which are presented on a pyrogram derived from the analysis (see **Figure A2.6** for an example from well Mbuo-1). The S1 peak is recorded in the early stages of pyrolysis (i.e. during the 3 minute 300ºC isotherm- see **Figure A2.5**). The S1 peak records the amount of free hydrocarbons present in the sample in the form of bitumen. The bitumen vaporised at the S1 stage should be that which has been cracked from the sample being analysed and thus determines whether the source rock is either potential or effective. If the latter, the FID records the volume of hydrocarbons already produced (expressed as mg per g). However, any residual drilling contaminants, such as diesel or migrated

hydrocarbons will also be volatised at this stage and may artificially enhance the S1 peak (see Peters, 1986 and Carvajal-Ortiz & Gentzis, 2012 for more details).

The S2 peak is recorded during the progressive temperature increase stage of the pyrolysis and usually occurs between 300ºC and 650ºC but can be higher for some Type III kerogens (Lafarge *et al.*, 1998 - **Figures A2.5** and **A2.6**). Rather than recording the free hydrocarbons in the sample, the increase temperature continues to crack the sample itself in order to determine the maximum amount of hydrocarbons that are still to be produced (also expressed as mg per g). The temperature at which the maximum amount of hydrocarbons is being cracked from the kerogen (i.e. the temperature at the top of the S2 peak) is also recorded and referred as the T_{max} peak (**Figures A2.5** and **A2.6**).

The S3 peak records the amount of CO and CO_2 (in mg per g) produced from the sample being pyrolysed (Peters, 1986, Lafarge *et al.*, 1998 - **Figures A2.5** and **A2.6**). The S3 peak is required to calculate the 'oxygen index' (OI) of a sample and is continuously recorded over the 300ºC to 390ºC temperature range. At pyrolysis temperatures above 400ºC, CO_2 is interpreted to be produced from mineral carbon (carbonate minerals, such as magnesite and siderite) rather than organic matter (Lafarge *et al.*, 1998.). Whilst magnesite and siderite decompose at lower temperatures, other, usually more dominant carbonate minerals, such as dolomite and calcite decompose and release CO_2 at much higher temperatures (up to 850ºC for calcite – Lafarge *et al.*, 1998). Therefore, to determine the amount of mineral carbon in the sample, the S4 peak, the sample is oxidised to the maximum temperature and the CO_2 values recorded from oxidation are combined with the pyrolysed CO_2 values over 400ºC.

Figure A2.5. Diagram depicting the different fractions of the total organic matter of rocks analysed, the corresponding parameters and their recordings (after Lafarge *et al.*, 1998).

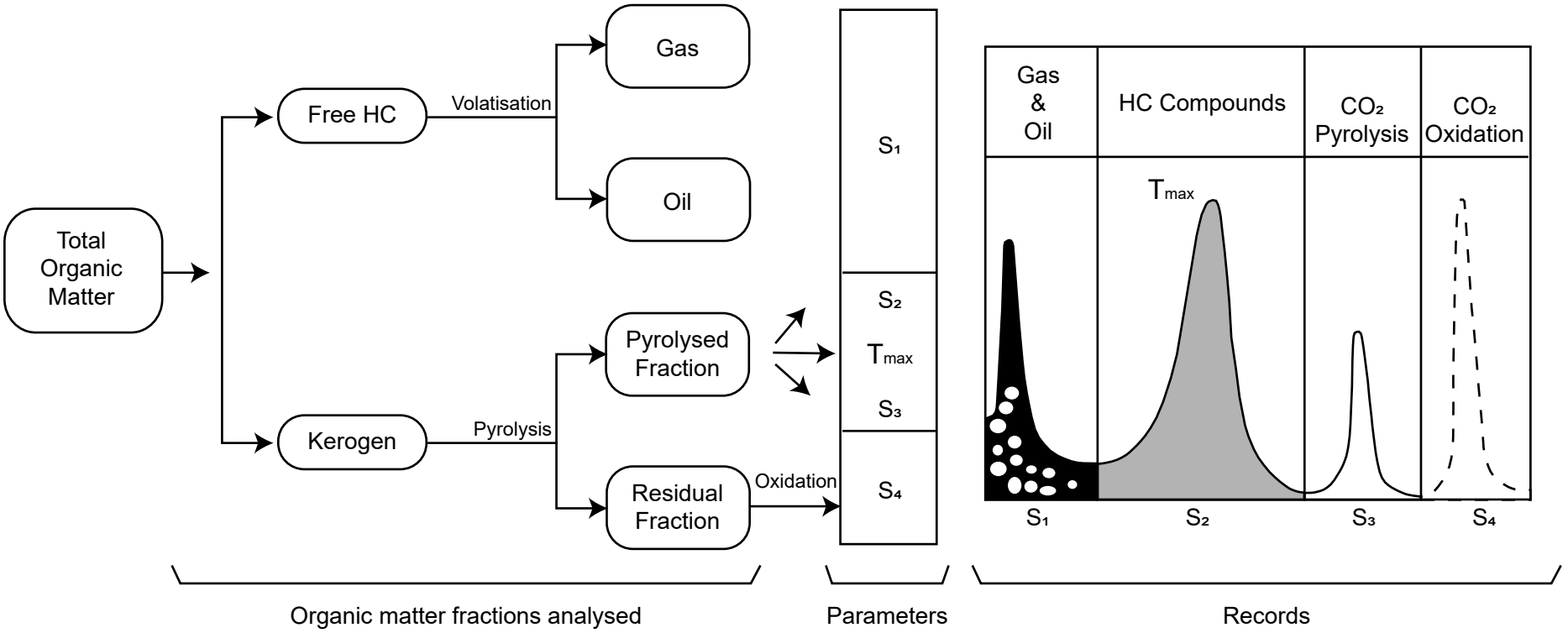

Figure A2.6. Pyrogram for sample 315m in well Mbuo-1

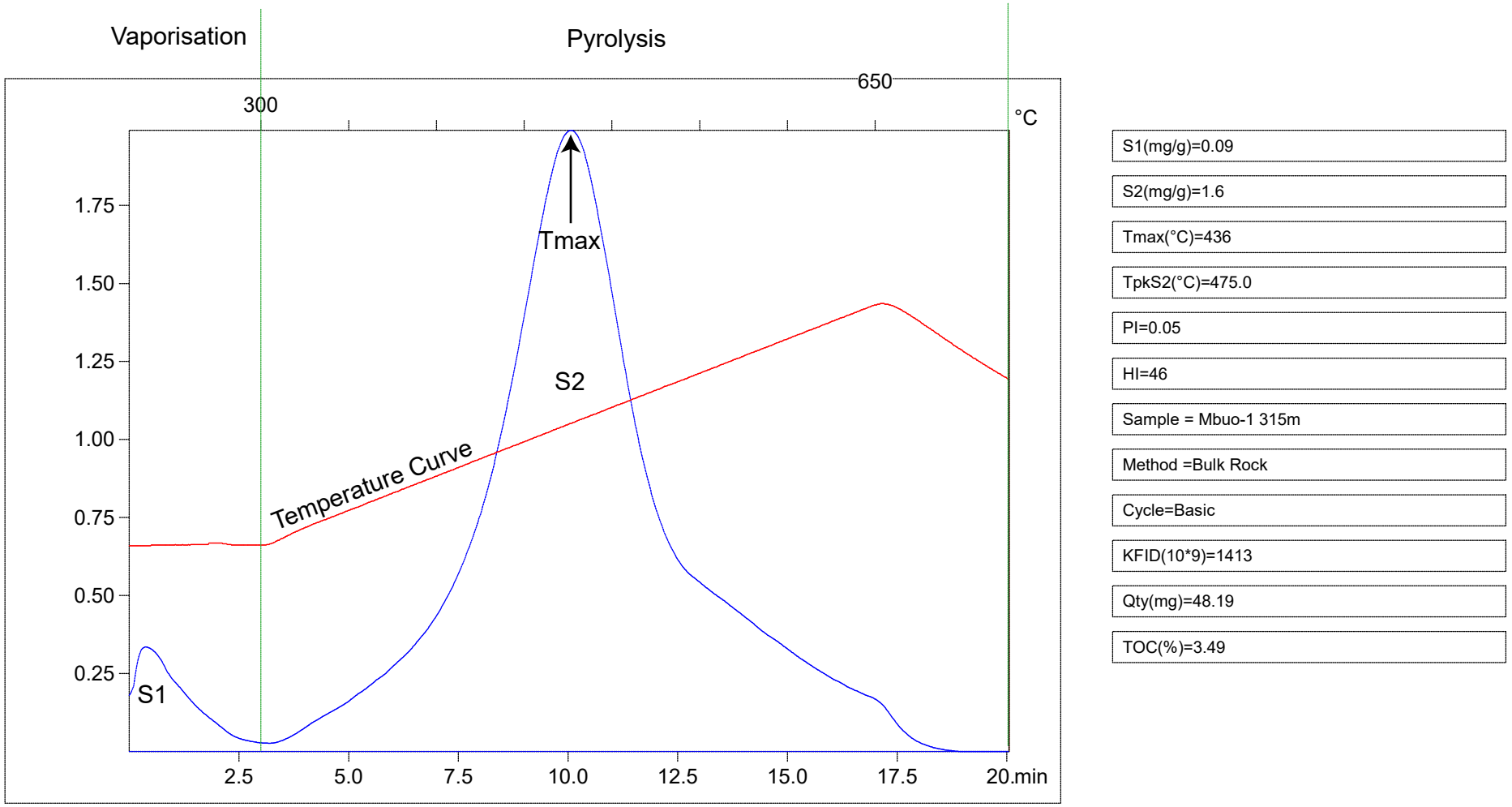

TOC information is also acquired through pyrolysis. However, unlike other analytical instruments such as the LECO (Lafarge *et al.*, 1998; Carvajal-Ortiz & Gentzis, 2015) that record TOC abundance directly, the Rock Eval 6 pyrolysis instrument calculates TOC by adding together the amount of pyrolysed carbon (PC) and residual carbon (RC). PC is calculated from the hydrogen compounds released in the S1 and S2 peaks, the CO released during the S3 peak and the CO_2 released up to 400ºC. RC is obtained during the oxidation phase by summing the amount of CO and CO_2 produced during the recording of the S4 peak.

Using the various data outputs described above acquired by pyrolysis, accurate determinations regarding the type and quality of potential source rocks in a study area can be made. Guidelines for such determinations are summarised by Carvajal-Ortiz & Gentzis (2015) and plotted on **Table A2.1**.

Table A2.1: Guideline values for interpreting the type and quality of source rocks from pyrolysis data (after Carvajal-Ortiz & Gentzis, 2015).

Quantity of OM	TOC (wt.%)	S2 (mg HC/g rock)	S1 (mg HC/g rock)	
Poor	<0.5	<1.0	0.0-0.5	
Fair	0.5-1.0	1.0-5.0	0.5-1.0	
Good	1.0-2.0	5.0-10.0	1.0-2.0	
Very Good	2.0-4.0	10.0-20.0	2.0-4.0	
Excellent	>4.0	>20.0	>4.0	
Kerogen Type (OM quality)	**Atomic H/C**	**Hydrogen Index (mg HC/g TOC)**	**S2/S3**	**Main Product at peak Maturity**
III	<0.8	50-200	<3	Gas
II/III	0.8-1	200-300	3-5	Gas & Oil
II	1-1.2	300-600	5-10	Oil & Gas
I	>1.2	>600	>10	Oil

There are three types of sample material under investigation: core, outcrop and cuttings. Prior to performing analysis of any kind, the quality of the different sample types need to be assessed. Any potential issues regarding sample contamination, or bias in any way needs to be identified and, as far as practicable, mitigated during the sample preparation stage.

Core from the shallow subsurface (i.e. 200m depth maximum – TDP) is the predominant sample type. Core samples are regarded as being the optimal sample type for geological analysis, as they are directly representative of the sedimentary succession from which they were collected: contamination in various forms (such as drilling mud / loss of circulation material contamination) is negligible and they are not normally affected by modern day processes of weathering and diagenesis (although weathering fronts of between 8m and 39m are recognised in many of the shallow TDP cores which may potentially affect geochemical results – see Nicholas *et al.*, 2006 and Berrocoso *et al.*, 2010, 2012 and 2015).

Mandawa Basin outcrop samples are the least numerous sample type examined in this study. Again, outcrop samples are generally free of artificial contaminants and practically, there is no limit to the amount of material that can be collected on site from which multiple detailed analyses can be performed, particularly analyses that require large sample volumes (such as heavy mineral analysis). The biggest quality issue regarding outcrop material, is that samples can be heavily affected by modern day processes of chemical weathering, especially in the sub-tropical conditions that prevail in Tanzania. Modern day weathering processes have the potential to drastically alter the mineralogy (and by association, chemistry), TOC values (as much as a 60% reduction: Waples, 2013) and kerogen quality of surficial sedimentary rocks compared to the same successions in the subsurface. Indeed, Hudson (2010) cites modern weathering processes as a potential causal factor for differences in pyrolysis results between the outcrop samples he analysed for his thesis and those acquired by Kagya (1996). However, based on the comparison of weathering indices calculated for surficial and subsurface rocks in the Mandawa Basin (**Chapter 6**) and the conclusion that the influence of recent and modern processes of chemical

weathering on the Mandawa Basin outcrop samples is minimal, it is more likely that the differences in pyrolysis results is related to different stratigraphic intervals being sampled.

Cuttings samples are the primary sample type in most of the deep test wells available to this study. Of all three sample types, cuttings samples are the most variable in terms of quality, which is related both to drilling practices (types of drill bit employed, rate of penetration, types of mud additives and other associated contaminants) and also the type of material being drilled (whether it is indurate or friable). Based on personal experience, cuttings samples can range in quality from excellent (i.e. bags containing large chips of a single rock type that is representative of the *in situ* sediments over the recorded depth range) to extremely poor (i.e. rock that has been reduced to powder by drilling, containing *in situ* material, material caved from younger successions and mixed with drilling additives such as barite mud, diesel and nut husks). Similar observations on cuttings are made by Waples (2013), who also points out that diesel mud additive contamination of a cuttings sample can potentially produce overestimated TOC values. Conversely, contamination by caving of non-organic matter-rich sedimentary material (e.g. sandstone, carbonate) may have the opposite effect and dilute the TOC signal of an *in situ* organic matter-rich sample. According to Waples (2013), most contaminants can be avoided through washing and the careful picking of the *in situ* lithology from the cuttings bag and avoiding analysing other contaminants.

As is discussed in **Appendix 6**, the process by which cutting samples have been selected for pyrolysis in this thesis is based on their redox-sensitive elemental composition rather than their sample quality. Once chosen, a single lithology, interpreted from supplementary log (GR, completion log) data as being the *in situ* lithology, is picked out under a binocular microscope, with every effort made to avoid any contaminants observed within the bags. Based on observations of the cutting samples, the quality is regarded as ranging from average to incredibly poor. Average quality cuttings are bags containing a mix of disaggregated sandstone and millimetre-sized claystone chips that are relatively easy to pick under a binocular microscope

(e.g. Mbuo-1, 2665m, Mihambia-1, 1717m, 2230m and Mita Gamma-1, 4270ft – **Figure A2.7**). Incredibly poor quality cuttings are bags containing a mix of disaggregated sandstone and ≤250μm sized claystone chips that are very difficult to pick under a binocular microscope (e.g. Mbuo-1, 3090m and Mita Gamma-1 5700ft, 7370ft – **Figure A2.7**). As a general observation, sample quality is poorest in the deeper portions of wells Mbuo-1 and Mita Gamma-1, which could be related to either a change in the drilling operation or related to similar physical properties of the rock being drilled in both wells. Of the alternatives, the latter is suspected as being more likely, as wells Mbuo-1 and Mita Gamma-1 were drilled by two different operators six years apart and it is unlikely that identical operational decisions were made by both Shell and Tanganyika Oil Company.

For some of the cuttings samples at the poorer end of the spectrum, a clean *in situ* sample could be isolated, but the sample volumes were low compared to most other samples (e.g. 28.21mg and 7.86mg in samples 3120m and 5720ft of wells Mbuo-1 and Mita Gamma-1 respectively. According to Peters (1986) and Carvajal-Ortiz & Gentzis (2012), for pyrolysis it is preferred that all sample volumes are roughly equal in order to negate any differences in results that significantly variable sample volumes can create (such as suppression of TOC values). Therefore, the pyrolysis data acquired from samples with low volumes will be treated with a degree of caution. At the extreme low end of the quality spectrum, such as in samples 5820ft and 7270ft in well Mita Gamma-1, a clean *in situ* sample could not be isolated at all. So, despite the positive indications from the inorganic geochemical data (see **Figure A2.7**) these samples were not submitted for pyrolysis.

Figure A2.7. Photographs of selected cuttings samples from wells Mbuo-1, Mihambia-1 and Mita Gamma-1.

Mbuo-1 - 2665m

Mbuo-1 - 3090m

Mihambia-1 - 2230m

Mihambia-1 - 1717m

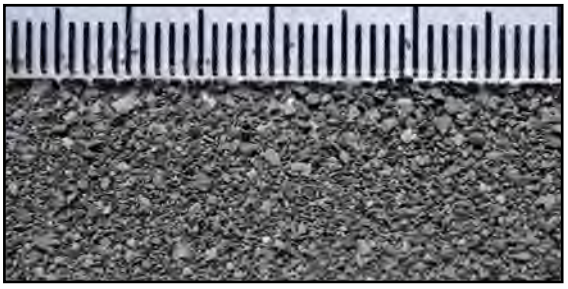

Mita Gamma-1 - 5720ft

Mita Gamma-1 - 4270ft

Mita Gamma-1 - 7370ft

Samples highlighted in red are regarded as the poorest quality and most challenging to pick, as the *in situ* rock chips are very small and subordinate to caved and disaggregated sandstone material

In this study, pyrolysis analysis has been undertaken by technicians at the University of Greenwich, UK, using a 'standard' model Rock-Eval 6 instrument. Calibration of the instrument is via the supplied Institut Français du Pétrole (IFP) reference material, which was also tested as an unknown at regular intervals through the analytical run. The University of Greenwich independently verify of performance of the Rock-Eval 6 instrument through the measurement of two Norwegian Petroleum Directorate (2000) geochemical standards SR-1 (Standard Svalbard Rock) and JR-1 (Standard Jet Rock), which are analysed at least once during every analytical batch (See **Table A2.2** for example).

Table A2.2: Performance test results of the Rock-Eval 6 instrument at the University of Greenwich using geochemical standards SR-1 and JR-1.

	Norwegian Petroleum Directorate Standards Approved Ranges					
	Sample	**S1**	**S2**	**S3**	**Tmax**	**TOC**
	Rock Eval 6 (preliminary possible ranges)					
	SR-1	0.9 - 1.2	5.0 - 6.1		433 - 440	2.16 - 2.64
	JR-1	6.7 - 7.5	67 - 79		429 - 435	11.2 - 13.4
	University of Greenwich Sample Measurements					
Batch 1	SR-1	1.17	6.02	0.32	437	2.48
	JR-1	7.26	71.54	0.55	431	12.25
Batch 1	SR-1	1.11	6.03	0.41	438	2.43
	JR-1	7.02	72.75	0.29	431	11.91

A2.3. RAMAN SPECTROSCOPY

Raman spectroscopy uses monochromatic electromagnetic (EM) energy to measure the strength of the chemical bonds of molecules within solids, liquids or gasses. The chemical bonds that hold the atoms of a molecule together can be displaced when exposed to an external energy source (Nasdala *et al.*, 2004; Andrews, 2017; John & George, 2017). The strength of the chemical bonds within molecules is dependent on their atomic composition and structural configuration: both of which are unique to the material being examined and thus produce a similarly unique Raman spectral fingerprint (Nasdala *et al.*). When introduced to an external energy source, the chemical bonds displace by experiencing (in order of energy required, from low to high) rotational, vibrational and electronic excitation (**Figure A2.7**). Multiple levels of rotational excitation (rotational bands) occur within each vibrational level and multiple vibrational bands occur within each electronic level. In every case, specific units of energy are required to stimulate all levels of rotational, vibrational and electronic excitement and it is the energy required to create rotational and vibrational excitation in a molecule that provides insights into the strength of its chemical bonds.

When an incident beam (i.e. a laser) producing monochromatic EM radiation at energy levels (wavelengths) within the visible light region of the EM spectrum (sufficient to induce vibrational excitation) passes through a sample, the light exits (scatters) in one of two ways: either elastically or inelastically (Nasdala *et al.*, 2004; Andrews, 2017; Chou & Wang, 2017; John & George, 2017). Elastic scattering, also known as Rayleigh scattering, occurs when no reaction occurs between the incident beam and the sample and the light exits at the same wavelength as it went in (**Figure A2.8**). Inelastic scattering occurs when a minute portion of the light energy interacts with the molecules of the sample by either giving energy to it (inducing rotational and/or vibrational excitation) or taking energy from it (inducing rotational and/or vibrational de-excitation). Thus the light scatters at a wavelength that is different to that of the incident beam.

Inelastic scattering is also known as 'Raman Scattering' or the 'Raman Effect' (**Figure A2.8**).

Figure A2.7. Energy diagram depicting energy exchanges with molecules that produce Rayleigh and Raman scattering.

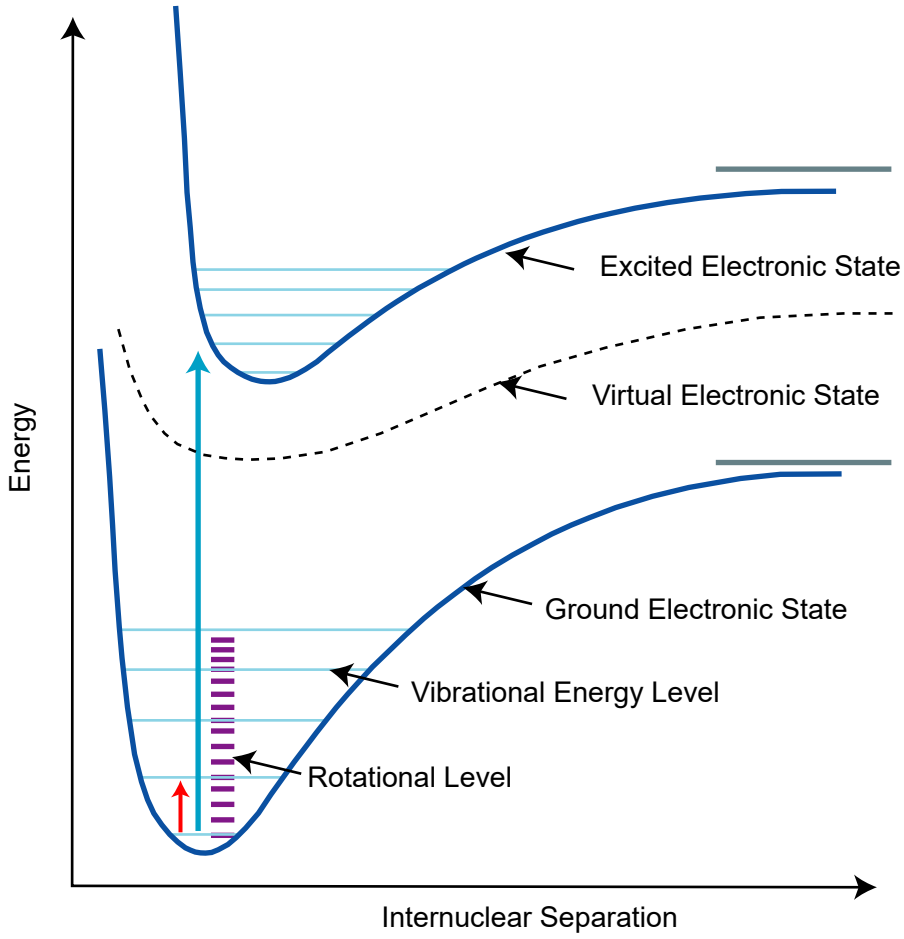

Modified from chem.libretexts.org

Of the two ways light can scatter, Rayleigh scattering is overwhelmingly dominant. Raman scattering accounts for approximately 10^{-6} to 10^{-7} of the light that interacts inelastically with the sample (Chou & Wang, 2017; Andrews, 2017). Therefore the intensity of the incident beam at any given wavelength has to be as high as it can be without inducing electronic excitation. When electronic excitation occurs, an electron absorbs a photon and momentarily jumps from the orbit of a lower electron shell to the orbit of a higher shell. Upon de-excitation to its ground state, the electron emits a photon at a lower energy to the incident beam; i.e. it fluoresces. Electronic fluorescence is a reaction fundamental for other analytical methodologies (X-ray fluorescence - Potts & Webb, 1992), but undesirable in Raman spectroscopy, as fluorescence is more powerful

and more dominant than Raman scattering. Thus, fluorescence obscures the unique Raman spectral fingerprint of a material (Nasdala *et al.*, 2004).

Figure A2.8. Energy diagram depicting energy exchange

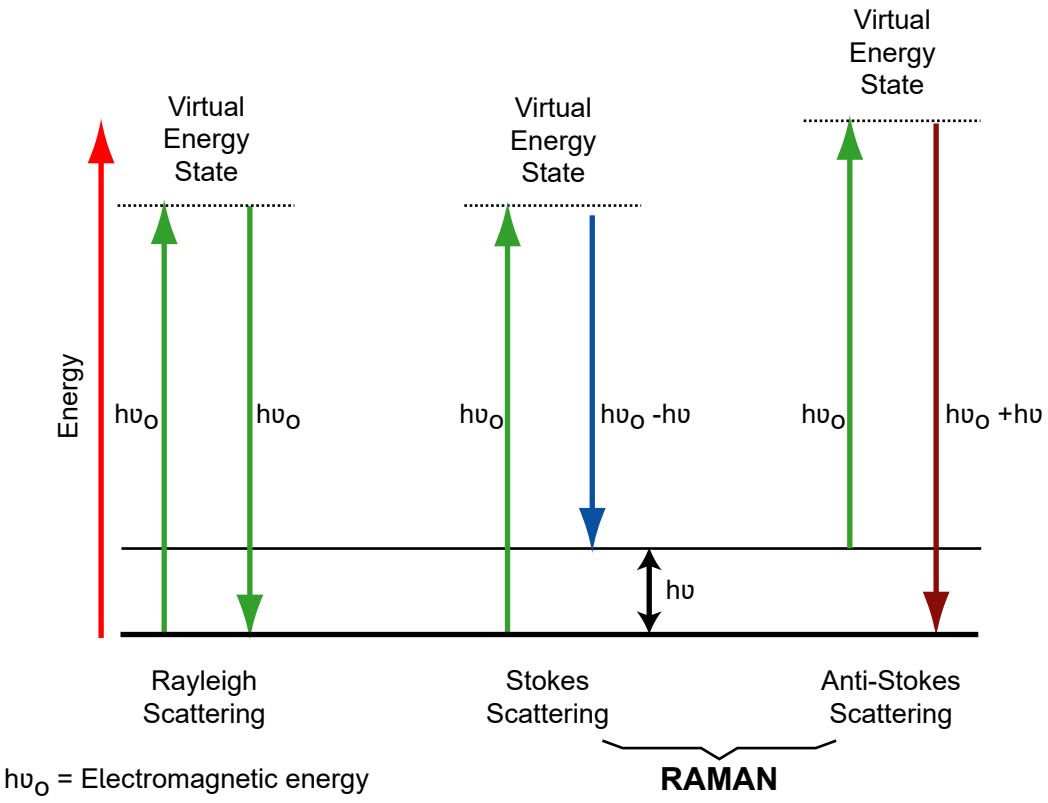

$h\upsilon_o$ = Electromagnetic energy

$h\upsilon$ = Energy difference between vibrational states of the molecule

Modified from John & George (2017)

In order to achieve a situation that permits a clear Raman spectral fingerprint of the analyte without stimulating electronic excitation, the incident beam has to be set to provide enough energy to excite the molecules to a 'virtual electronic state' (Nasdala *et al.,* 2004; John & George, 2017). A virtual electronic state is an unstable and unobservable quantum state that can theoretically occur anywhere between real electronic states, such as the ground state and first excited electronic state (**Figures A2.7** and **A2.8**). The energy applied to reach the virtual electronic state is the optimal amount to produce the clearest Raman signal for measurement without inducing fluorescence.

As the molecular bond strength of substances varies greatly, so too is the energy required to reach a virtual electronic state. When analysing a material containing multiple different compounds (e.g. a heavy mineral separate), an incident beam set at one wavelength and one energy level may produce the desired strong Raman scatter in some but either undesirable weak Raman scatter or fluorescence in others. Experimentation with lasers of different wavelengths (higher wavelength blue lasers vs. lower wavelength red lasers and everything in between) and intensities may therefore be required to achieve optimum results (Andò & Garzanti, 2013 - see later, this section).

The EM waves produced during Raman scattering are recorded as shifts relative to the Rayleigh peak, which has the same energy as the incident beam. The Raman shifts are best discerned when the incident beam is monochromatic with as narrow a bandwidth on the EM spectrum as possible (Nasdala *et al.*, 2004). If the Raman wavelength is lower in energy than the Rayleigh peak (i.e. the molecule has taken energy from the incident beam) the downshift in energy is known as a Stokes shift. Conversely, if the Raman wavelength is higher in energy than the Rayleigh peak (i.e. the molecule has given energy to the incident beam) the upshift in energy is known as an anti-Stokes shift. Every spectral peak created by Raman scattering has both a stokes and anti-stokes part that are shifted equidistantly either side of the incident beam.

Figure A2.9 depicts a schematic of a typical Raman instrument. The Raman spectrometer is attached to an optical microscope. The incident beam is emitted from a laser set at a predetermined wavelength and focused onto the sample through the microscope objective. The scattered light is then captured through the same objective and passed through a notch filter in order to attenuate the Rayleigh signal but allow the discrete Raman-shifted waves to pass back into the spectrometer. Once in the spectrometer, the Raman waves are deflected by a prism onto a diffractive grating, which separates the composite waves into their single component wavelengths. The grating then disperses the individual waves across a Charge Couple Device (CCD) detector to measure their wavenumber position and spectral intensity (reported as

wavenumber in cm^{-1} - Chou & Wang, 2017).

Figure A2.9. Schematic representation of a Raman spectrometer (from Chou & Wang, 2017).

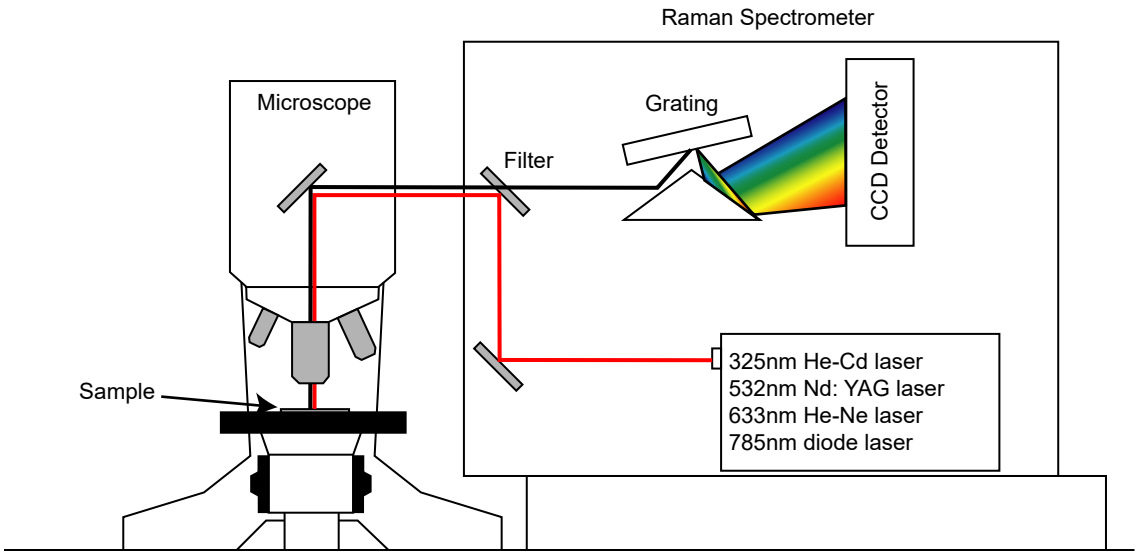

When the Raman spectral data is plotted graphically (**Figure A2.10**), the Rayleigh line is conventionally set as zero wavenumbers. Stokes peaks have positive wavenumbers and anti-stokes peaks have negative wavenumbers (Nasdala *et al.*, 2004). Peak intensity is measured in arbitrary units (a. u.) and as is shown on **Figure A2.10**, the stokes peaks are stronger than the anti-stokes peaks. The reason for this phenomenon is because at ambient temperatures, there are more molecules in the ground state than in an excited electronic state (Andrews, 2017). As such, more molecules will react with the incident beam by absorbing rather than emitting energy. Thus, the anti-stokes peaks are weaker than their stokes counterparts and less useful for spectral fingerprinting.

Figure A2.10. The stokes and anti-stokes parts of a Raman spectrum (modified from Nasdala *et al.*, 2004).

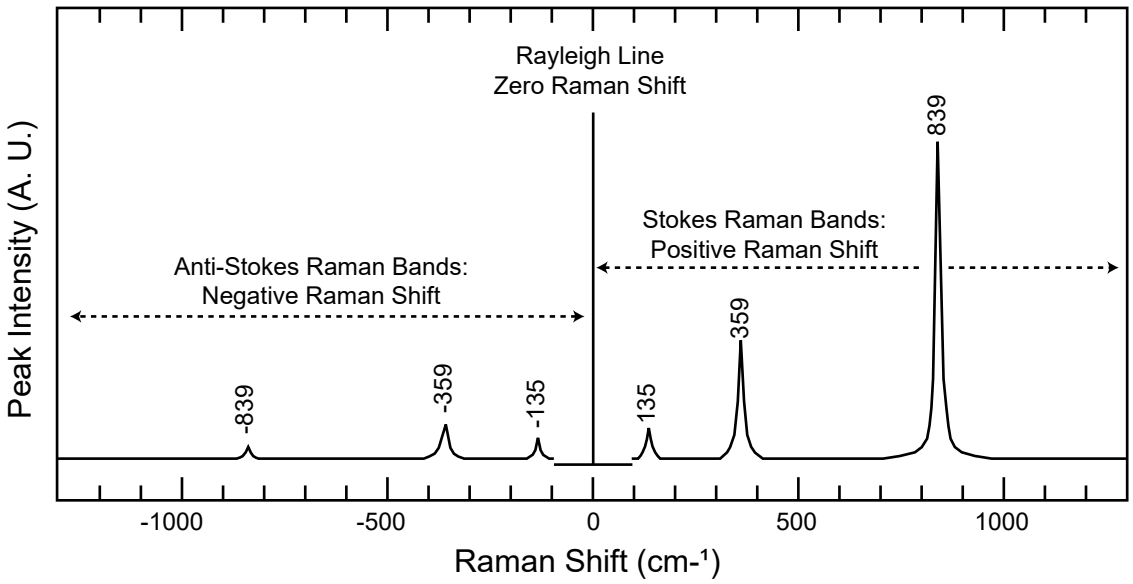

Andò & Garzanti (2013) provide an excellent summary of the various ways Raman spectroscopy can be effectively employed in the discipline of heavy mineral analysis. As well as assisting optical analysts to confidently identify highly weathered and opaque grains such as pyrite, haematite, magnetite and ilmenite, mineral polymorphs such as rutile, anatase and brookite or sillimanite, kyanite and andalusite, can be confidently differentiated. Chemical variations within isomorphous mineral species like garnet can be easily detected and the degree of metamictization in radioactive species such as zircon can be readily determined through subtle shifts in Raman peaks at specific wavenumbers. The acquisition time of the Raman spectra from individual grains is quick, ranging from less than one second for minerals with a good Raman response, to a minute for minerals with poorer signals (Andò & Garzanti). Moreover, the spot size of the incident beam is sufficiently narrow that heavy minerals can be examined at grain sizes of a few microns, thus opening up the 'new frontier' of provenance analysis in progressively finer-grained sedimentary rocks.

For heavy mineral grains to be positively identified from their diagnostic Raman spectral fingerprint, a comprehensive reference database needs to be available for comparison purposes. Andò & Garzanti (2013), present the diagnostic Raman spectra for a wide range of opaque and non-opaque heavy minerals and cite a number of texts and online databases that are available to acquire reference Raman spectra on a wide range of minerals. Andò & Garzanti report that within the University of Milano-Bicocca, the publically available Raman spectral databases have also been augmented by spectra acquired in-house from minerals of precisely known specific chemical composition. Even more comprehensive spectral databases are also likely exist within other universities and commercial laboratories. Such databases are likely to be more restricted in terms of access. Clearly, and regardless of the quality of Raman spectra acquired from the spectrometer, one of the limiting factors of obtaining meaningful results is the quality of the reference database employed for spectral matching.

In this study, samples were prepared for Raman analysis by technicians at Chemostrat Ltd, UK. For heavy mineral analysis of siltstones and claystones, Chemostrat Ltd employ a wide grain-size window of 10-250µm to capture and pre-concentrate the heavy minerals from the rocks. The principal advantage of employing a wide window is that heavy minerals of a wide variety of potential grain-sizes are captured within the rock (the entire 'crop' – Mange & Maurer, 1992), particularly those present at the finer end of the spectrum.

To separate clay-sized heavy minerals from the 10-250µm grain-size fraction, samples were disaggregated, dry sieved with 250µm size sieves and then wet sieved using 10µm size sieves. Acidic dissolution (10% acetic acid solution) was performed to dissolve carbonate grains. Heavy minerals were then separated in lithium heteropolytungstate solution (LST Fastfloat, 2.89 g/cm3) using the funnel separation technique as described by Mange and Maurer, 1992.

Raman analysis of the heavy mineral separates was conducted by technicians at the University of Greenwich, UK. The material was weighed and loose grains were securely placed onto a glass slide for analysis. By not fixing the heavy mineral grains in resin, a problem highlighted by Totten & Hanan (2007) of the smallest grains being completely submerged and thus undetectable by the incident beam is avoided. Each heavy mineral slide was inserted into a Horiba LabRam Raman Microscope and subjected to analysis using a 532nm green laser. The green laser is routinely employed by technicians at Greenwich as it provides the best balance of fast analysis time and production of the clearest Raman spectra for the widest range of heavy minerals.

Rather than manually moving the microscope stage to target individual heavy mineral grains for Raman analysis, the instrument software utilises imaging software to map all the grains on the slide. Once co-ordinates of all grains are obtained, the software then automatically moves the stage to analyse the centre of each individual grain. All mineral grains present on the slide were analysed and upwards of 600 counts were routinely acquired, which is in contrast to the standard 200 grain point count often employed under optical analysis (Mange & Maurer, 1992; Morton & Hallsworth, 1994). Once acquired, the spectral data was transmitted to technicians at Chemostrat Ltd for processing.

Over eleven thousand separate Raman spectra have been acquired for this thesis. The volume of spectra is too large and too time consuming to be processed manually. Chemostrat Ltd have developed software that compares the unknown Raman spectra acquired from a sample to a compiled database of heavy mineral reference spectra in order to positively identify its likely mineralogy. The reference database employed in this study comprises heavy mineral spectra acquired in-house by Chemostrat Ltd, but also utilises the Raman spectra published in the RRUFF database (http://rruff.info/) as an additional cross-check. The spectra matching process tests the statistical viability of the match by using both the correlation coefficient from linear regression and the confidence score from neural network analysis: if both methods return the same mineral match and have a high R^2 (around 0.7) and confidence respectively, then the mineral is considered

to be correctly identified (see **Figure A2.11** for an example).

Any spectra that cannot be confidently matched to a mineral in the database is highlighted by the software for manual evaluation. Often, the spurious spectra is related to material that has fluoresced and therefore is of no use for geological interpretations. Examples of the spectra matching process for heavy minerals identified in this study are presented on **Figures A2.11** to **A2.15**. The software package outputs the total counts of non-opaque and non-micaceous heavy mineral grains in excel format. The counts are then converted into percentage abundances of the individual heavy mineral assemblages of a sample. The counts of all minerals determined by Raman spectroscopy on selected TDP cores are presented on **Table A2.3**.

Figure A2.11. Typical Raman spectra for zircon and tourmaline acquired in this study.

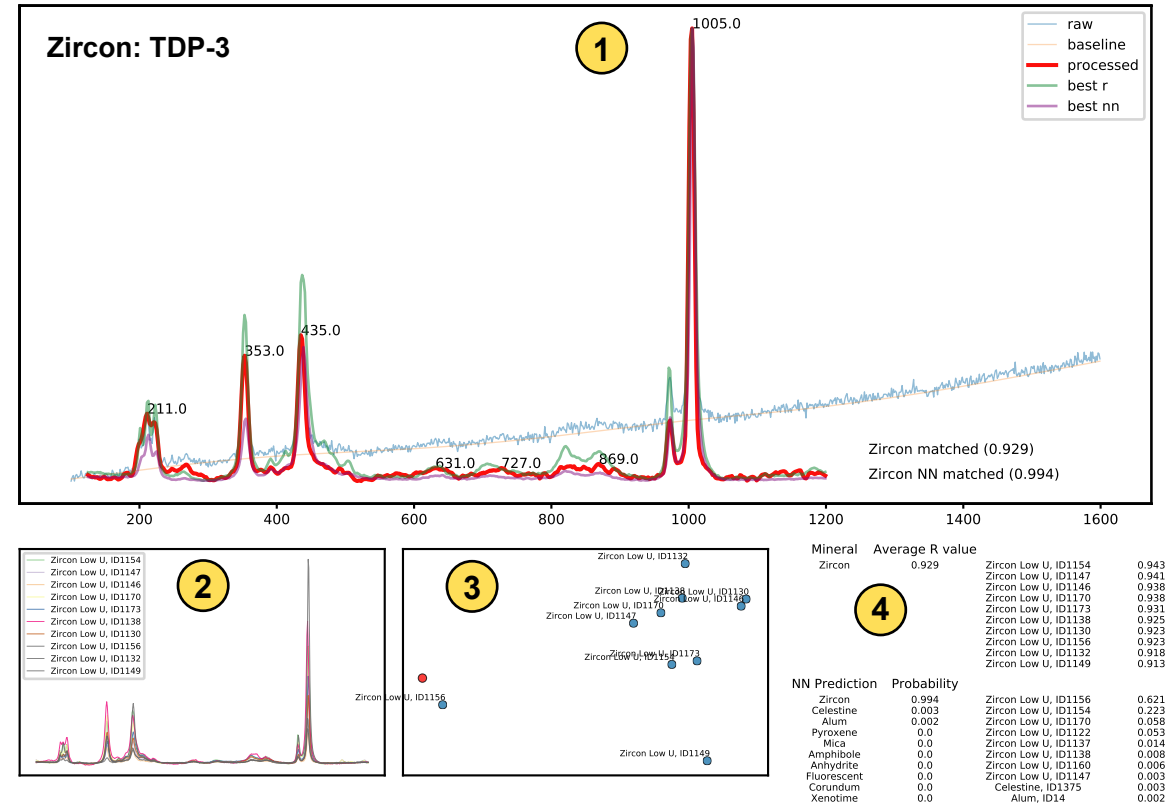

1 Spectra matching interface

2 Top 10 best r² value matches for the mineral

3 Principal Components Analysis (PCA) of the top 10 spectral matches in the database, plus the mineral spectra under examination

4 Top ten confidence and probability that the spectra under examination has been correctly linked to a specific mineral

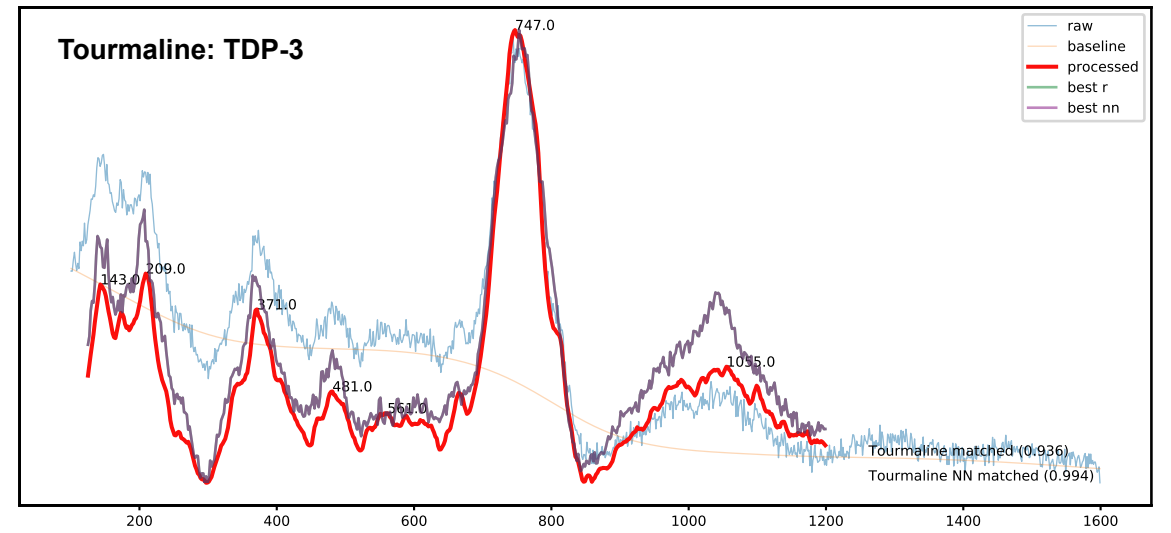

Figure A2.12. Typical Raman spectra for rutile, anatase and brookite acquired in this study.

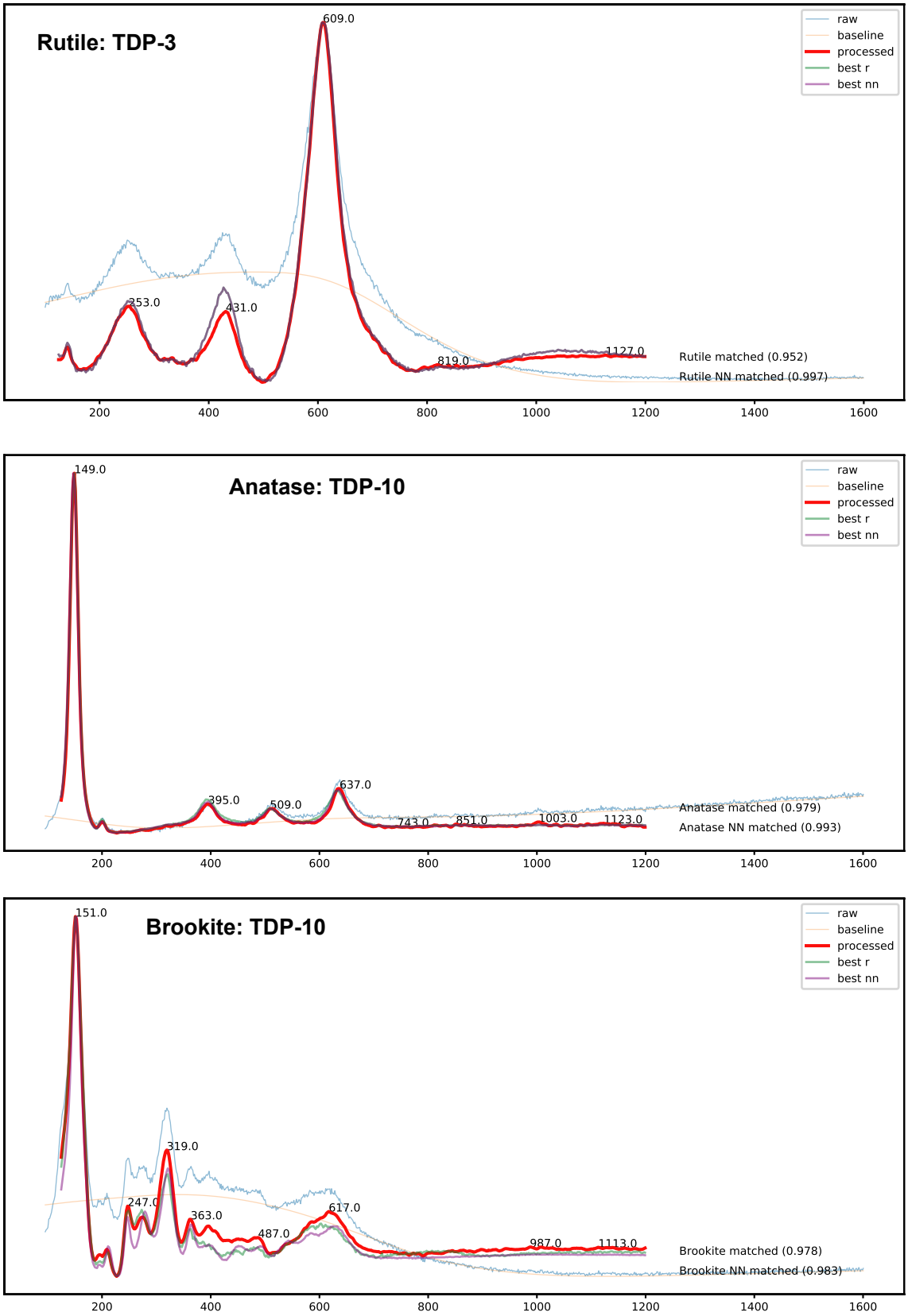

Figure A2.13. Typical Raman spectra for apatite, monazite and xenotime acquired in this study.

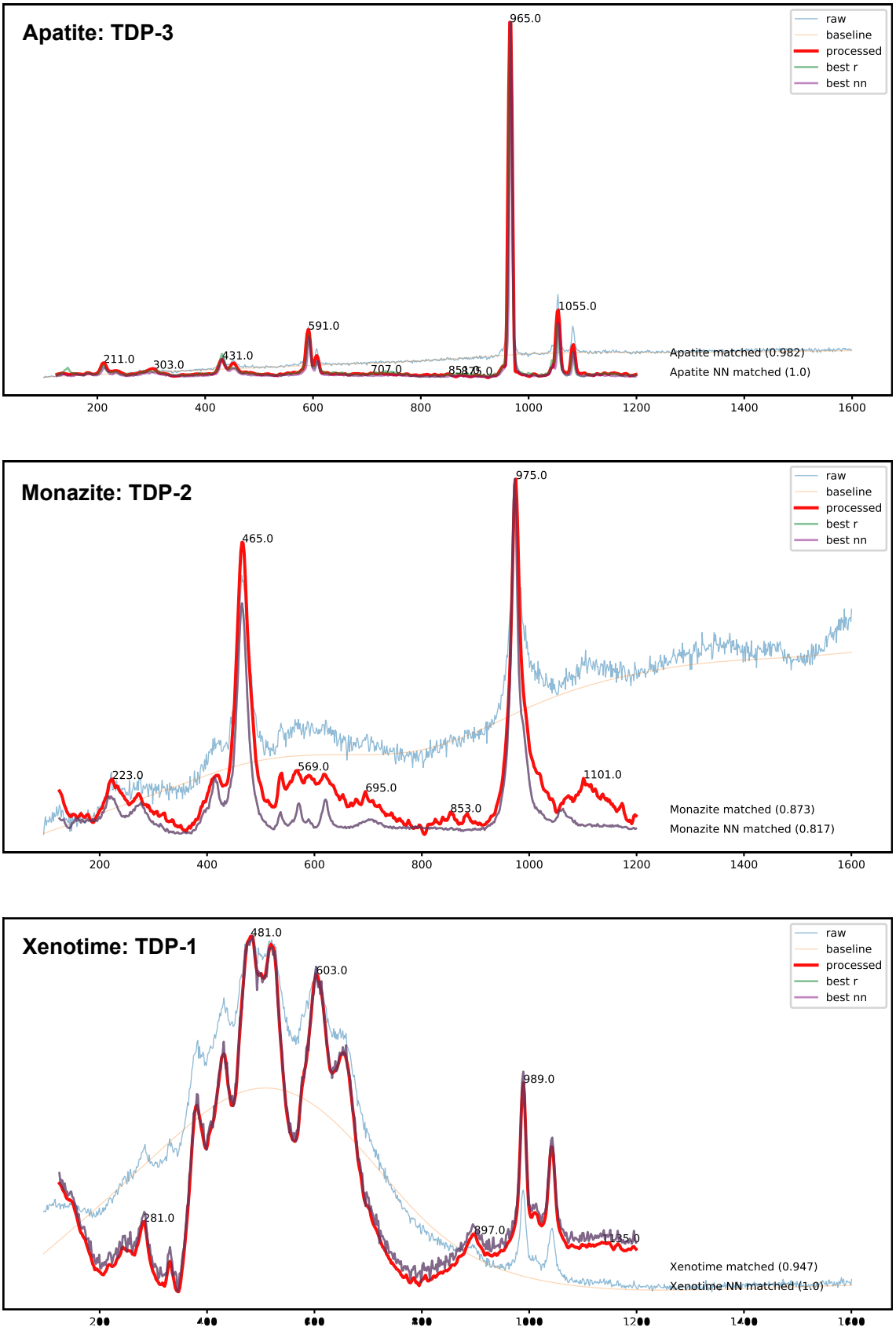

Figure A2.14. Typical Raman spectra for epidote, kyanite and garnet acquired in this study.

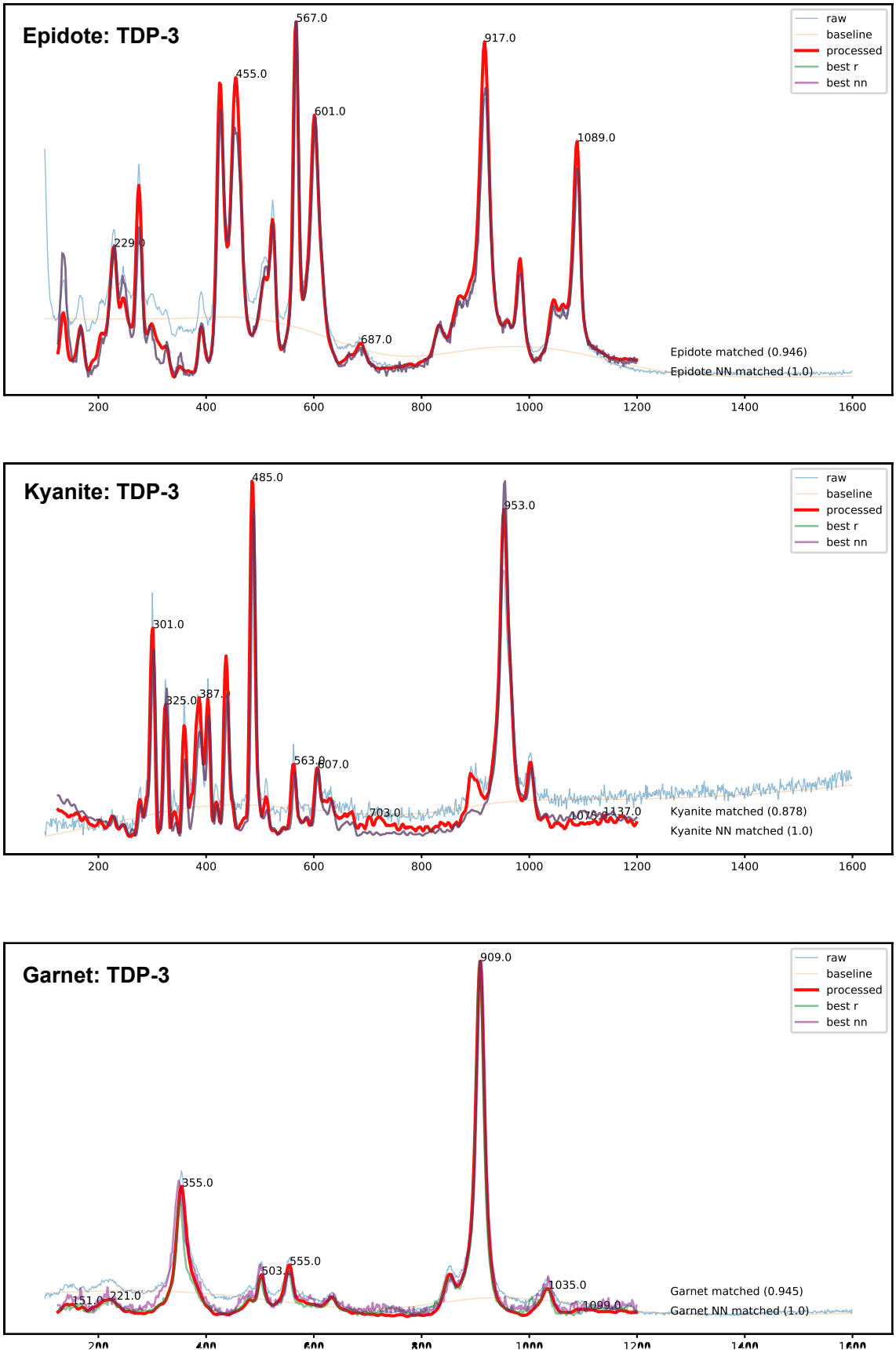

Figure A2.15. Typical Raman spectra for staurolite, titanite and pyroxene acquired in this study.

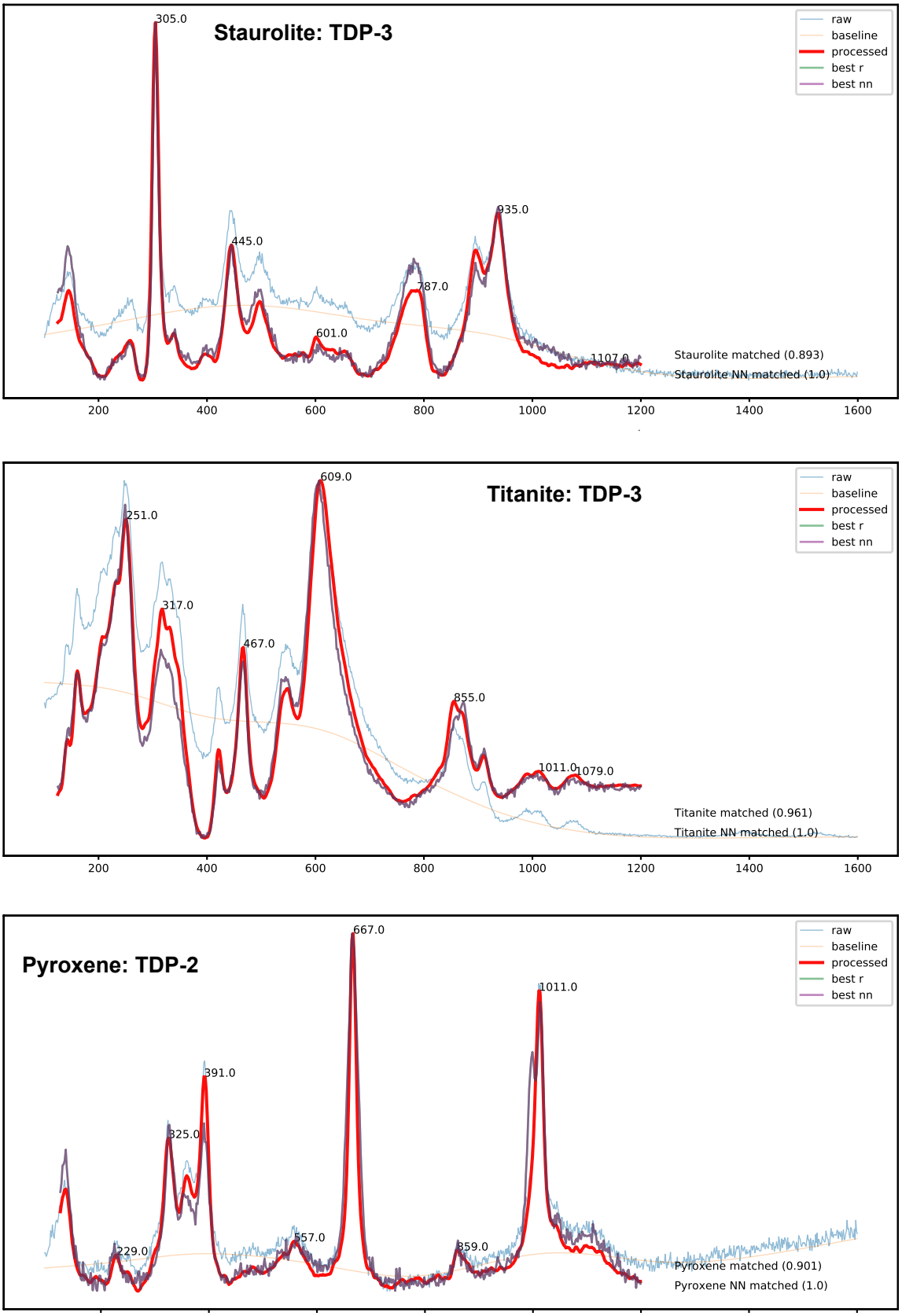

Table A2.3: Counts of all minerals acquired by Raman Spectroscopy on selected TDP cores.

Sample	Allanite	Anatase	Apatite	Baryte	Brookite	Chloritoid	Chrome-Spinel	Epidote	Garnet	Jarosite	Kyanite	Monazite	Pyroxene	Rutile	Staurolite	Titanite	Tourmaline	Xenotime	Zircon
TDP-1 (6/1-8 + 6/3-1 + 7/2-1)	0	19	16	1	2	0	0	110	50	0	4	0	0	28	2	58	9	2	20
TDP-2 (12/1-59 + 13/3-13 + 14/1-13)	1	15	20	0	0	0	0	71	61	0	8	2	1	30	0	86	4	0	28
TDP-3 (12/1-42 + 15/2-57 + 17/1-65)	0	30	16	3	3	1	1	105	92	0	13	0	2	50	1	104	5	0	37
TDP-14 (4/2-40 + 5/1-30 + 5/2-30)	0	12	6	0	2	0	0	2	43	0	0	1	1	39	0	26	2	0	17
TDP-10 (27/1-57 + 28/1-53)	0	8	5	1	1	0	0	24	55	0	1	0	0	24	1	39	5	0	18
TDP-37 (56/1-25 + 58/2-1 + 69/1-1)	0	8	13	2	1	0	0	1	52	0	0	0	0	18	2	5	14	0	17
TDP-23 (32/1-23 + 32/2-37 + 35/3-26)	0	9	16	0	0	0	0	2	118	0	2	0	0	37	1	8	6	1	43
TDP-31 (21/3-23 + 23/1-20 + 25.1-23)	0	30	66	1	0	0	1	5	248	0	0	4	0	99	0	128	8	0	66
TDP-40 (28/1-43 + 32/1-33 + 33/1-20)	0	45	108	2	6	0	1	2	155	0	1	7	0	94	2	120	17	1	47

Table A2.3: Continued.

Sample	Haematite	Pyrite	Carbonate	Chlorite	Feldspar	Microcline	Quartz	Unresolved Spectra	Glass (Slide)
TDP-1 (6/1-8 + 6/3-1 + 7/2-1)		1	1		1		12	203	62
TDP-2 (12/1-59 + 13/3-13 + 14/1-13)			1		2		5	114	70
TDP-3 (12/1-42 + 15/2-57 + 17/1-65)	43	3	2		4	1	13	508	140
TDP-14 (4/2-40 + 5/1-30 + 5/2-30)					5		11	258	160
TDP-10 (27/1-57 + 28/1-53)	1				3		32	266	81
TDP-37 (56/1-25 + 58/2-1 + 69/1-1)							6	293	102
TDP-23 (32/1-23 + 32/2-37 + 35/3-26)		1	1		2		7	221	93
TDP-31 (21/3-23 + 23/1-20 + 25.1-23)	26	2	1		1		1	306	25
TDP-40 (28/1-43 + 32/1-33 + 33/1-20)	45	2	1	3	8		4	415	29

APPENDIX 3: CHARACTERISATION & / OR CORRELATION OF TDP CORES OVER KEY CHEMOSTRATIGRAPHIC BOUNDARIES

Figure A3.1. The Sequence EC – MLC chemostratigraphic boundary picked in TDP-40A.

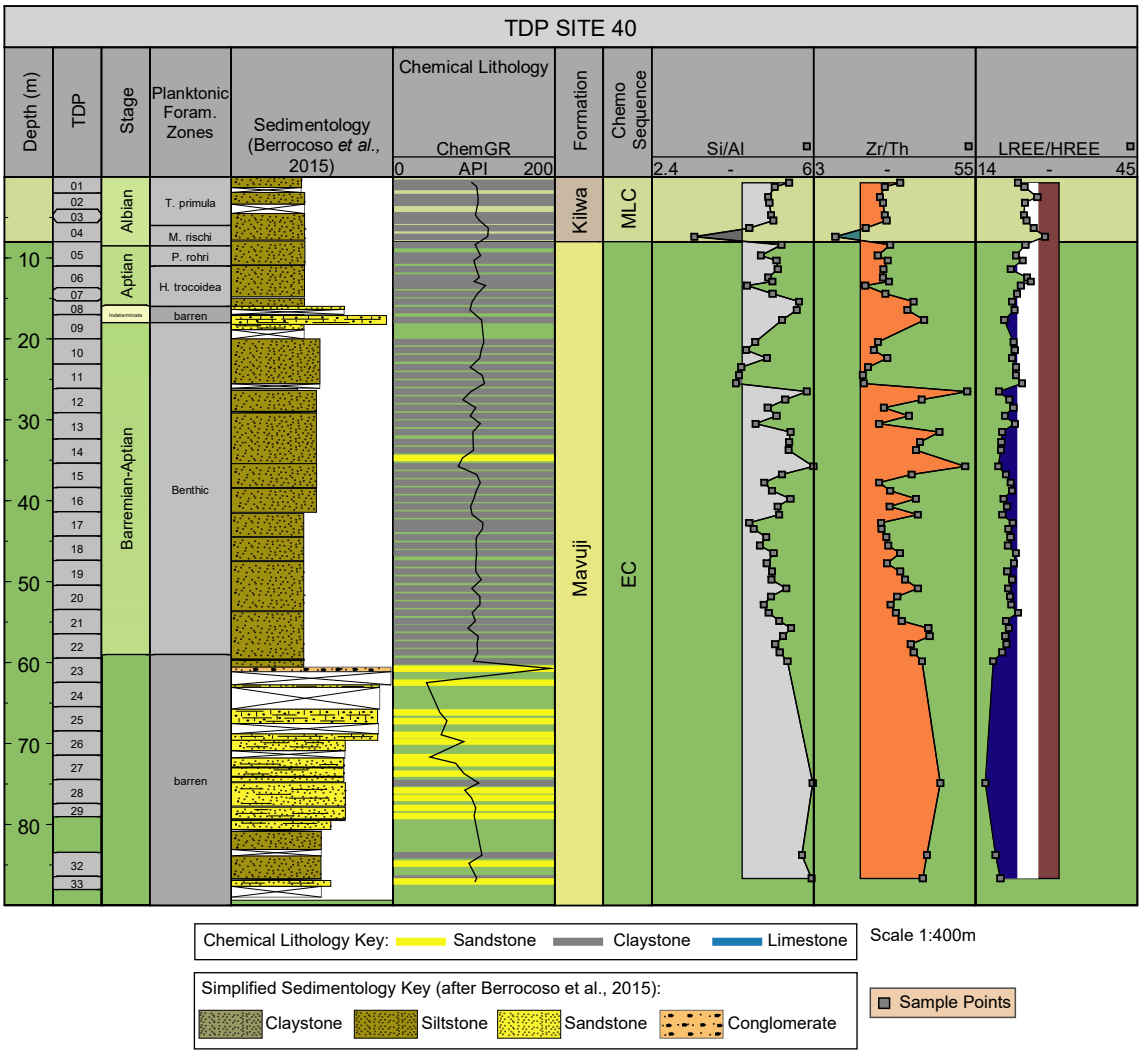

Figure A3.2. The Sequence MLC – Pg chemostratigraphic boundary picked within TDP-37.

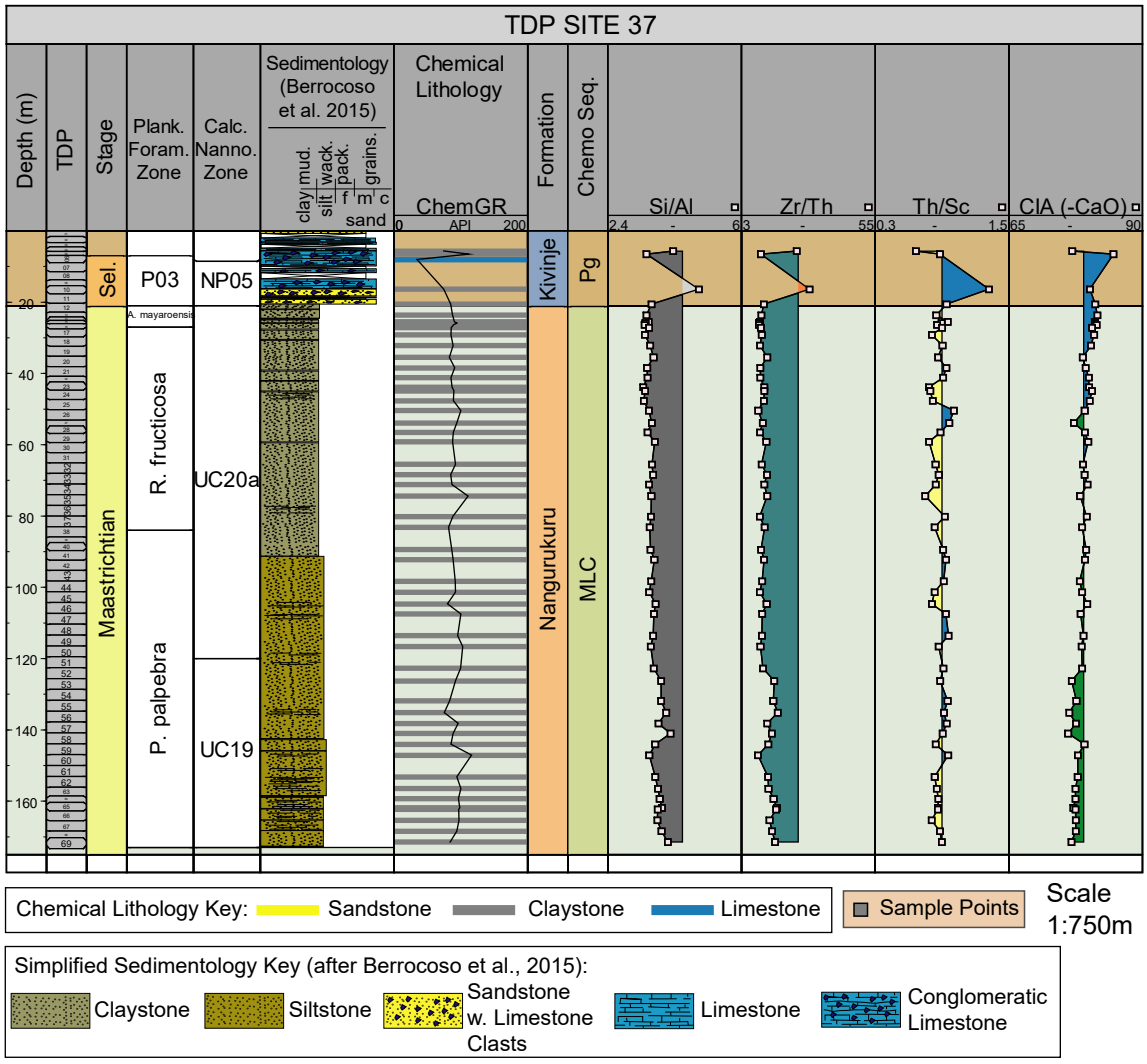

Figure A3.3. The Sequence Pg – LPg-Ng chemostratigraphic boundary picked between TDP-12 and TDP-1.

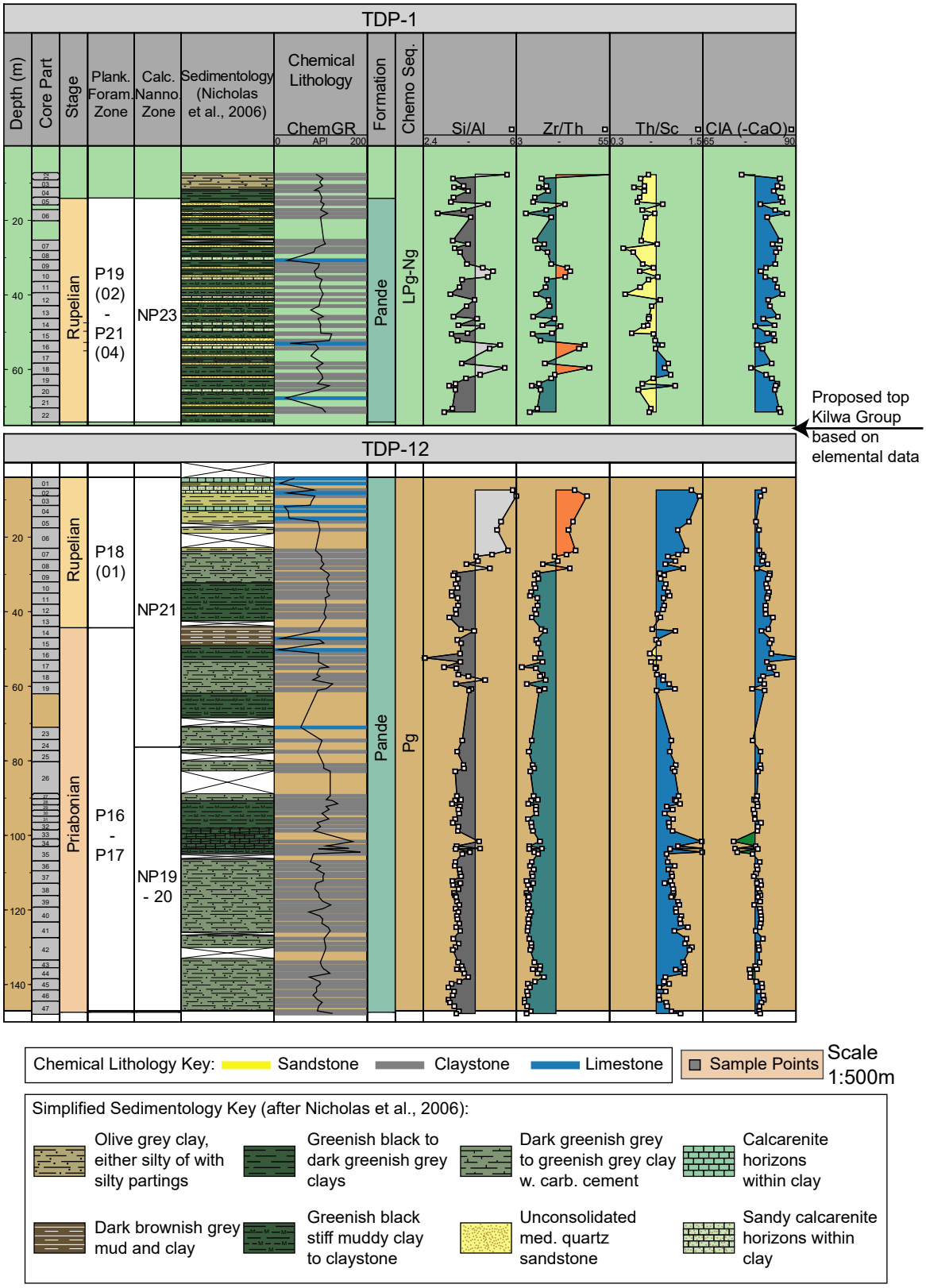

Figure A3.4. The Package MLC1 – MLC2 chemostratigraphic boundary picked within TDP-23.

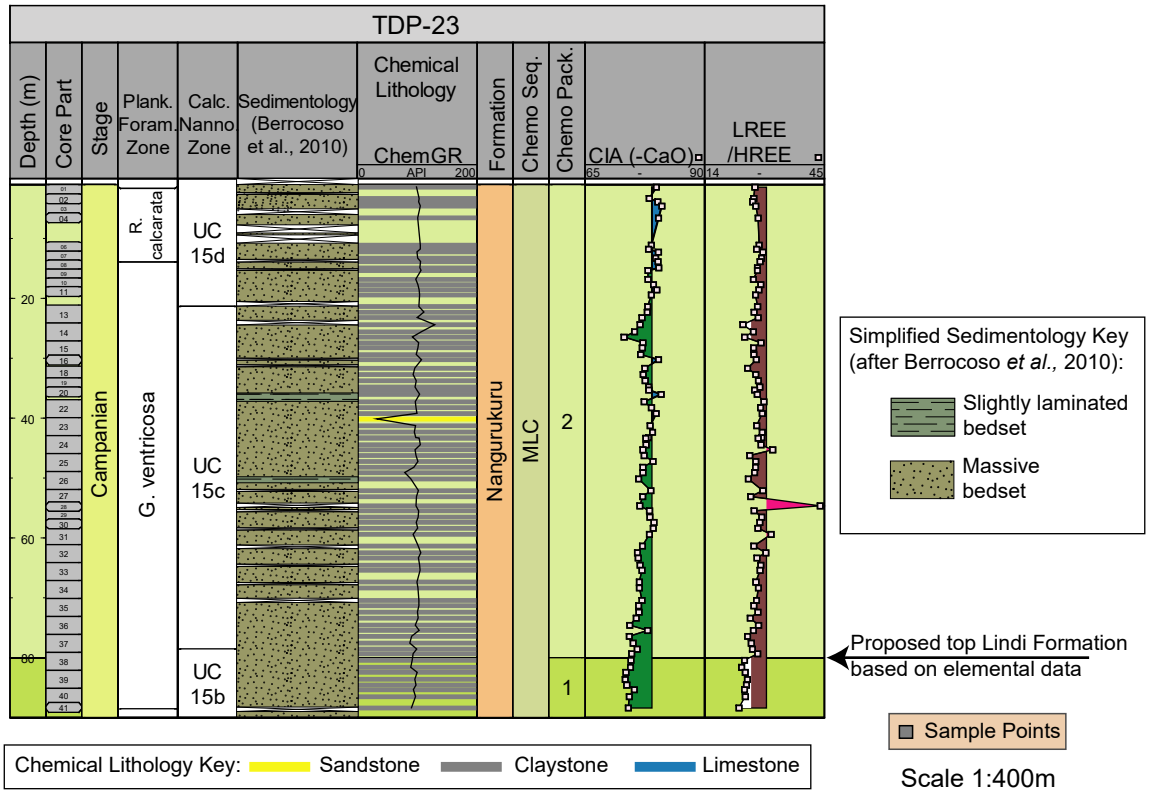

Figure A3.5. The Package Pg1 – Pg2 chemostratigraphic boundary picked within TDP-14

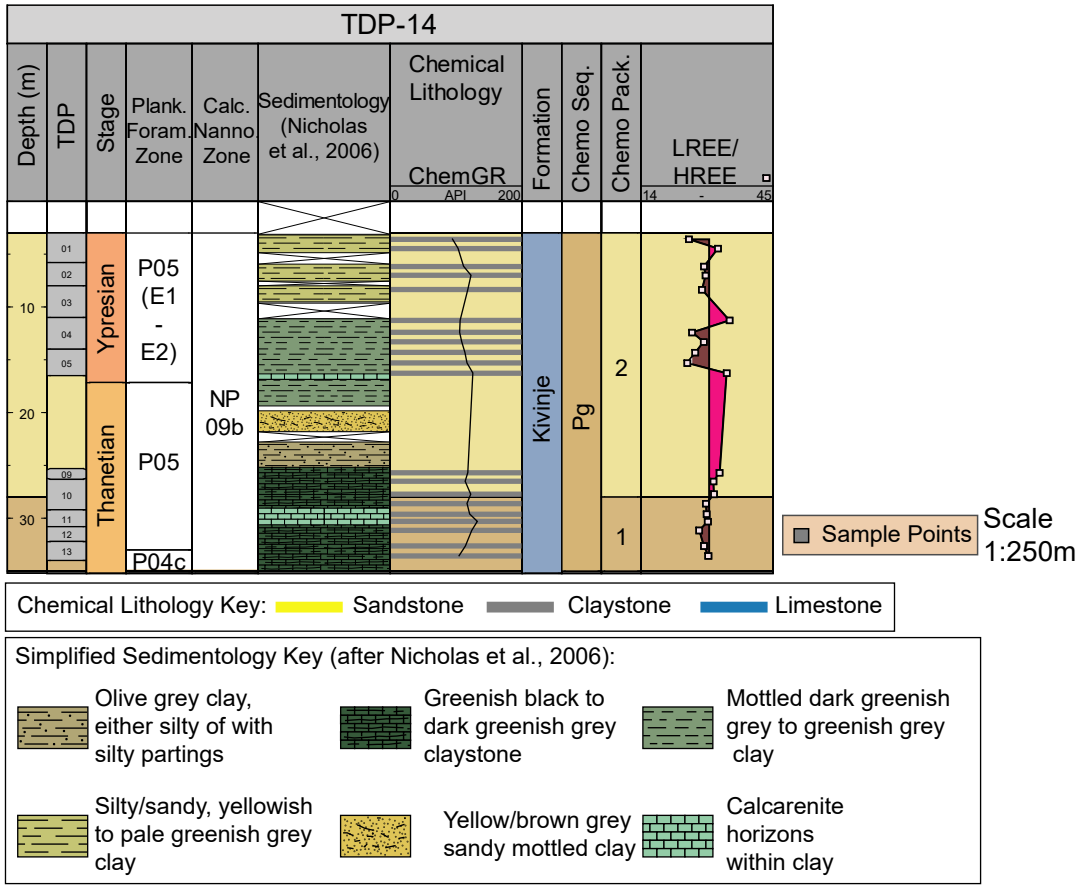

Figure A3.6. The Package Pg2 – Pg3 chemostratigraphic boundary picked between TDP-2 and TDP-3.

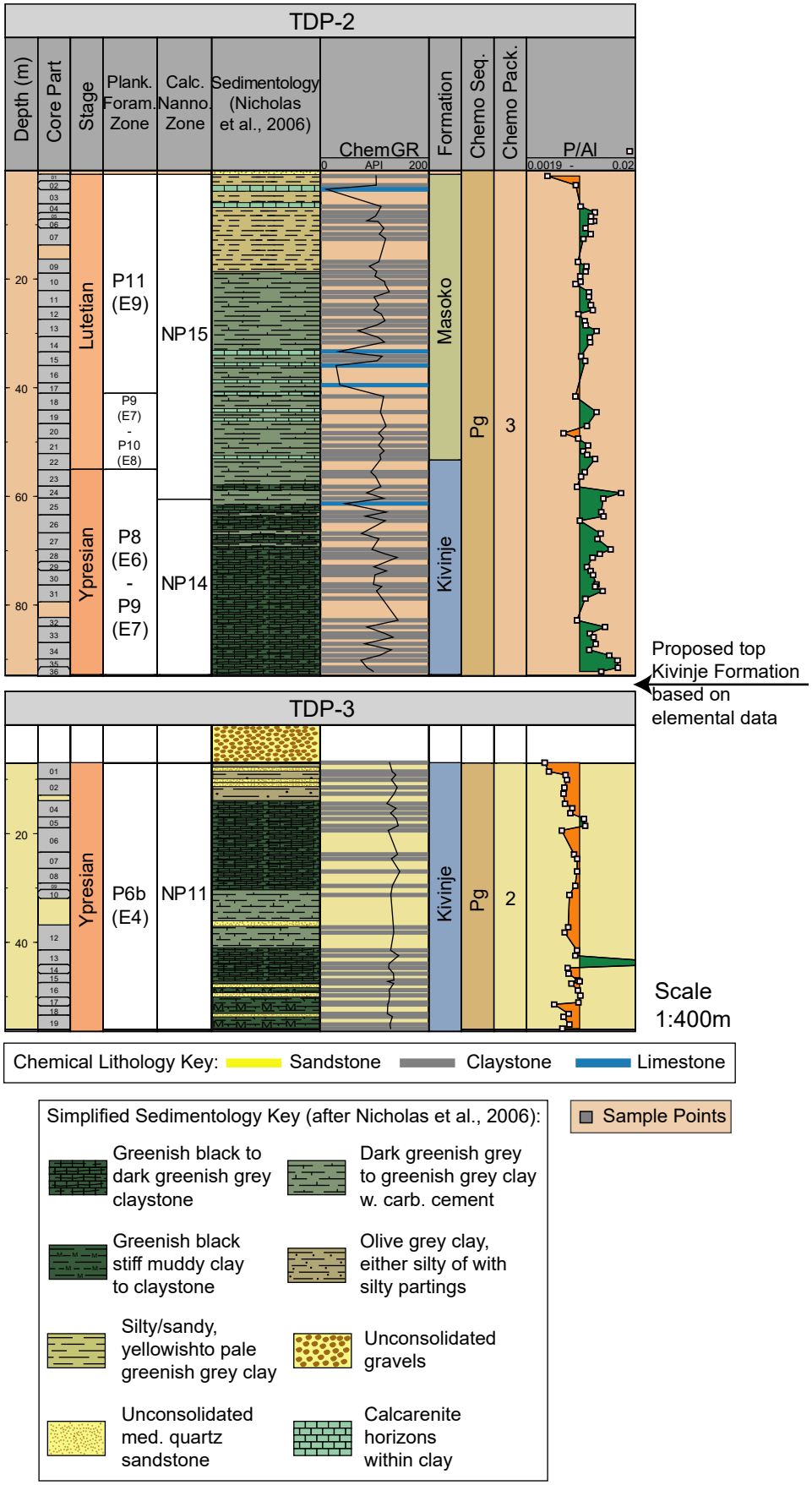

Figure A3.7. The Package Pg3 – Pg4 chemostratigraphic boundary picked within TDP-12.

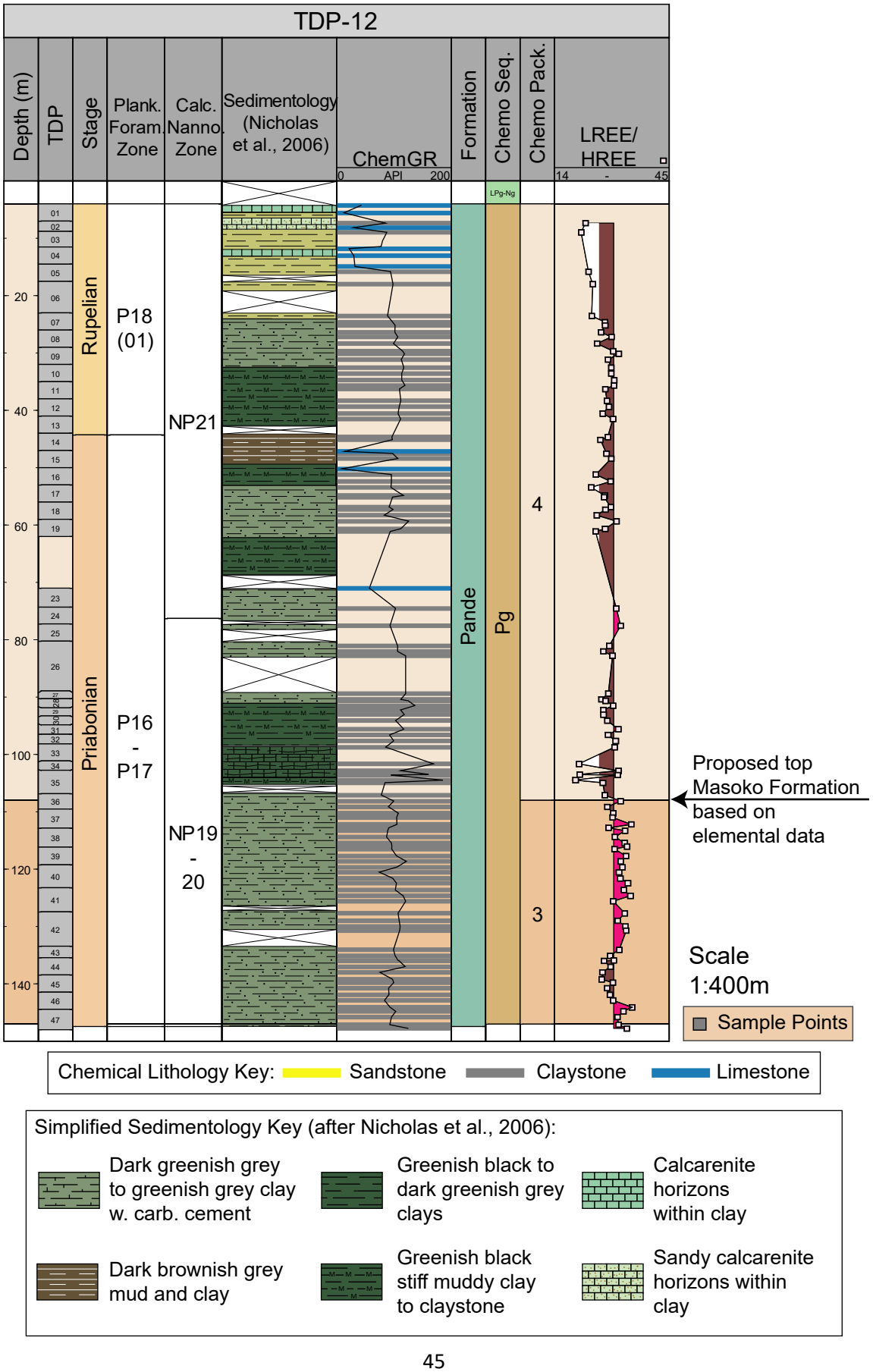

APPENDIX 4: CHEMOSTRATIGRAPHIC SUMMARY PANELS OF THE DEEP TEST WELLS

Figure A4.1. Chemostratigraphic characterisation summary of well Mbuo-1.

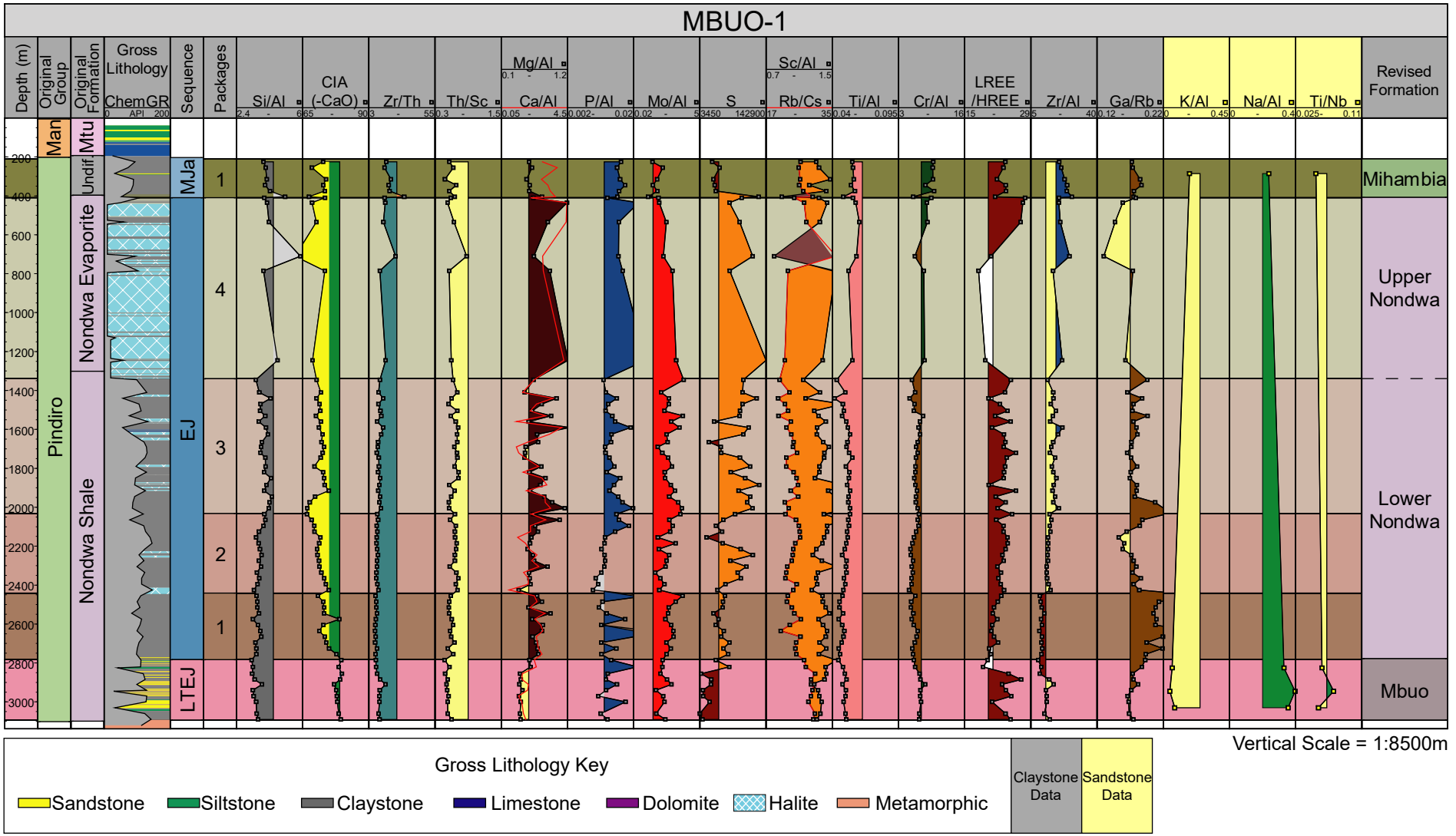

Figure A4.2. Chemostratigraphic characterisation summary of well Mihambia-1.

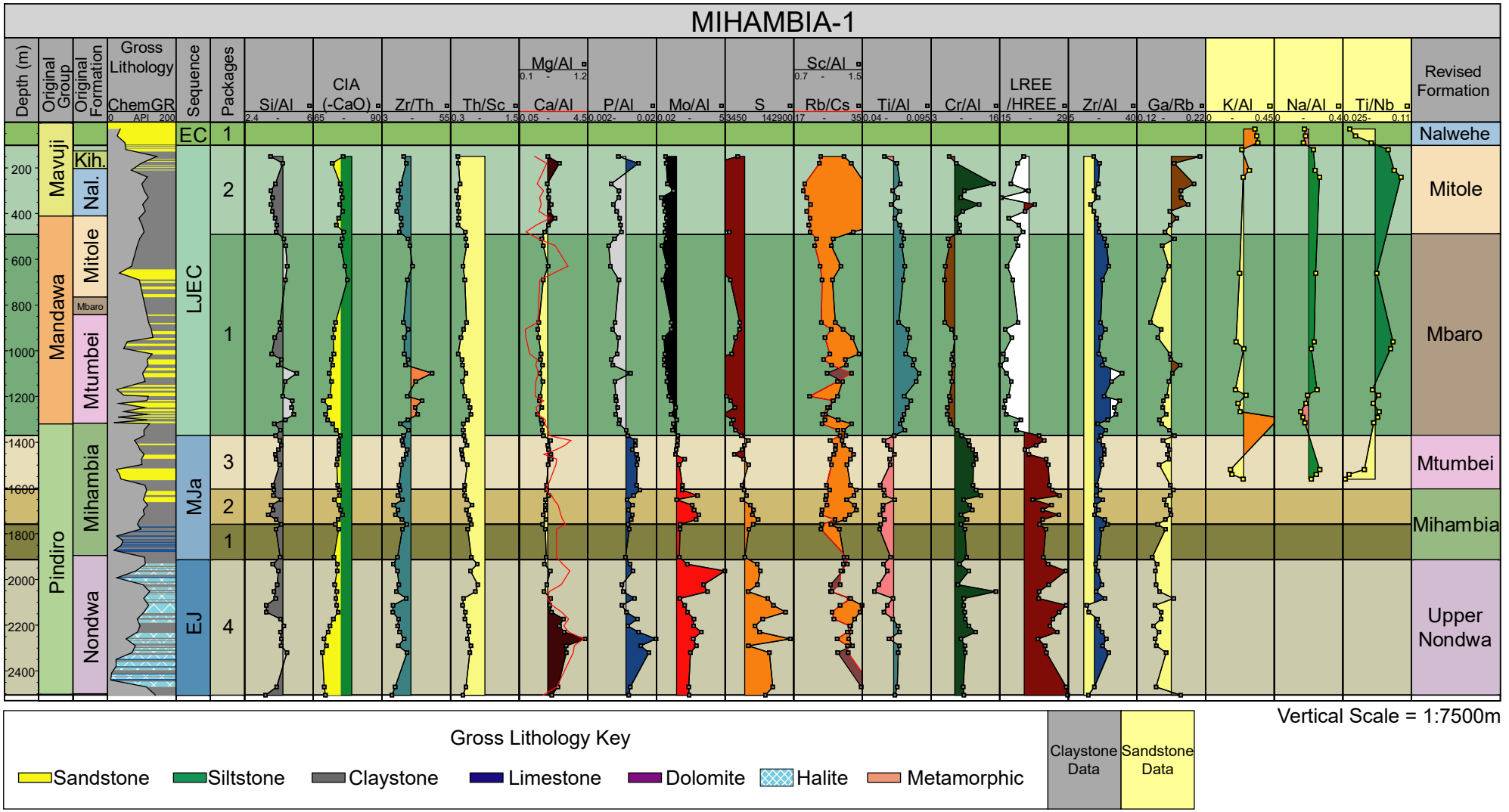

Figure A4.3. Chemostratigraphic characterisation summary of well Kizimbani-1.

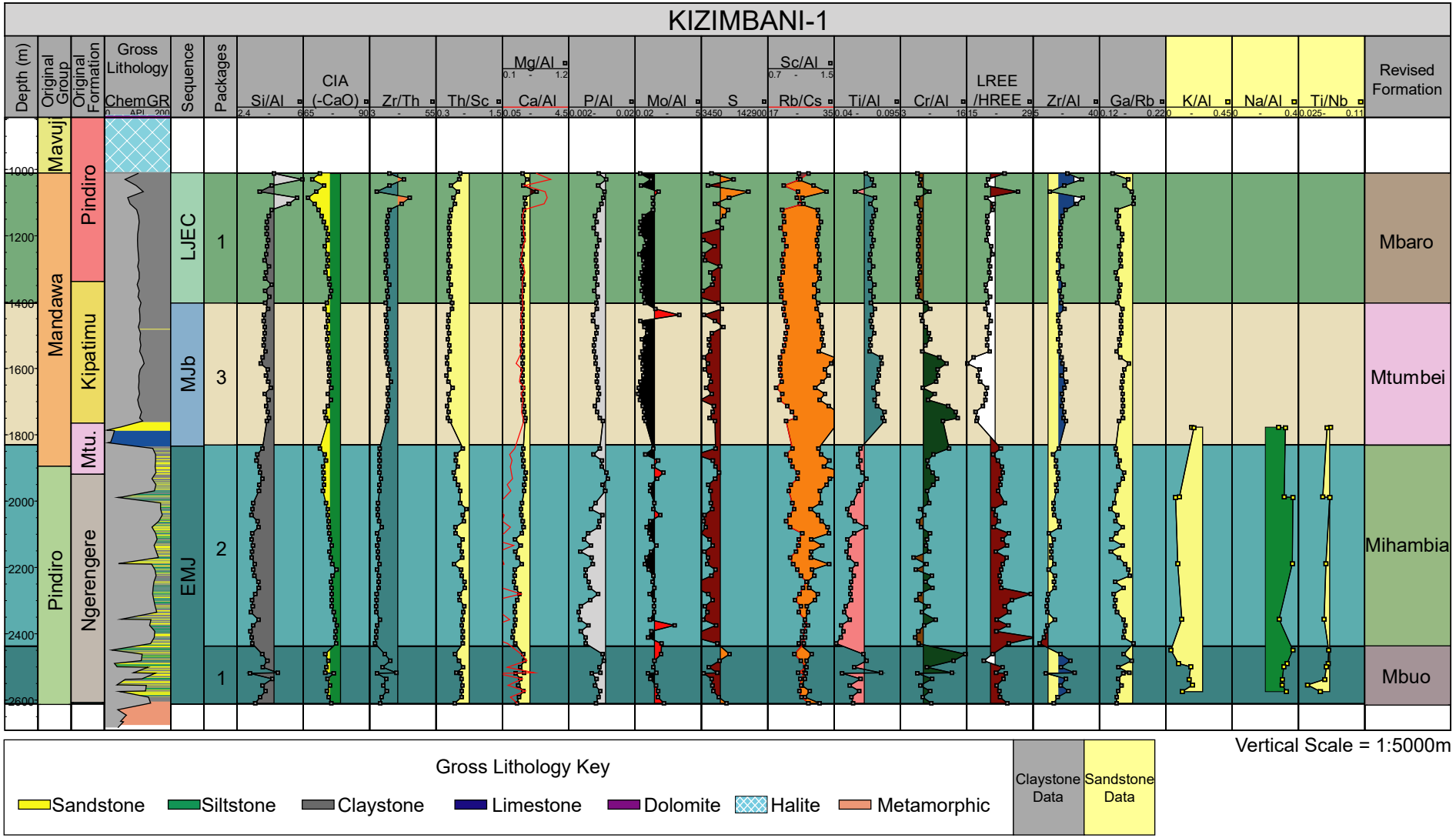

Figure A4.4. Chemostratigraphic characterisation summary of well Mita Gamma-1.

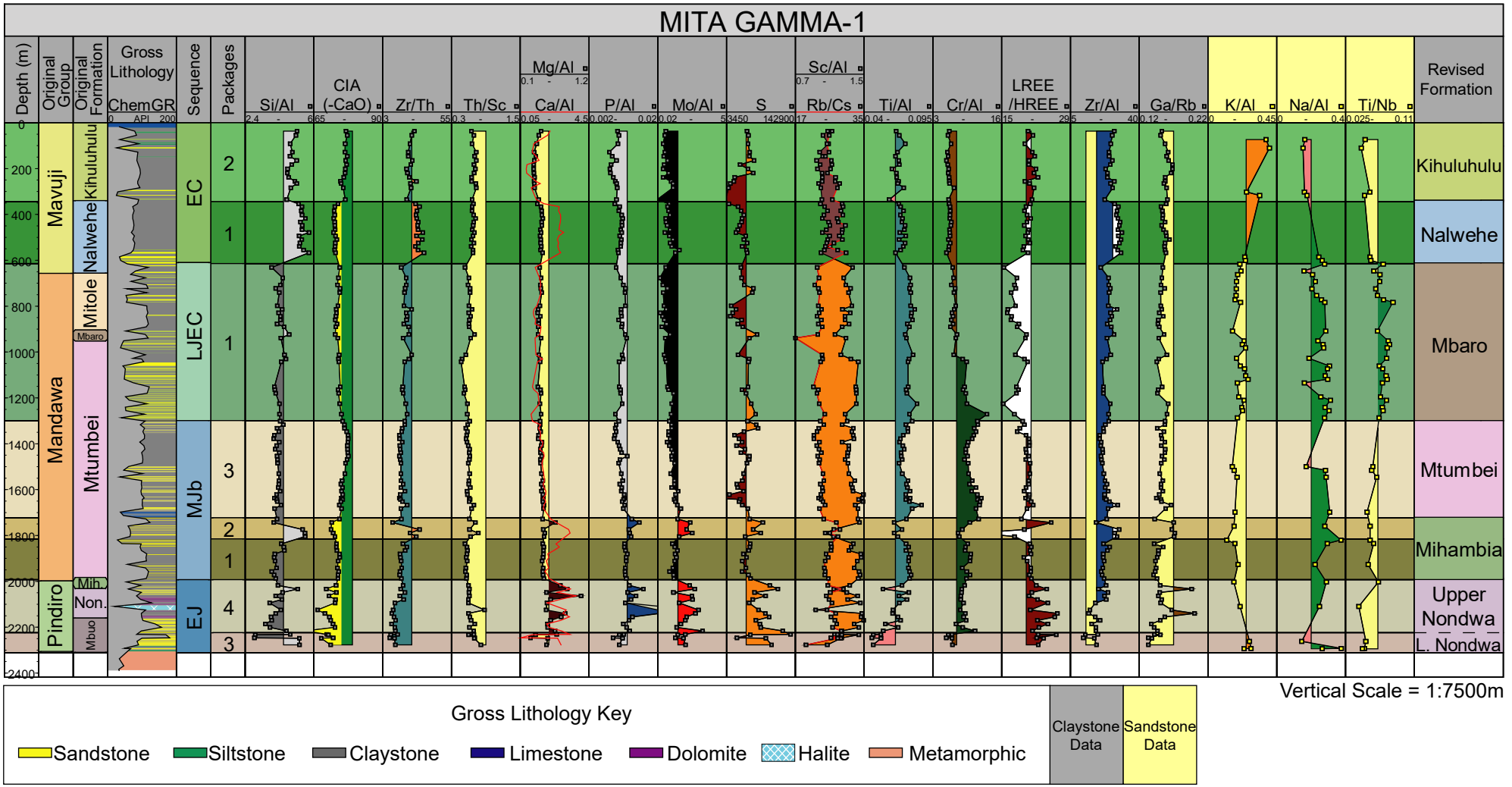

APPENDIX 5: PER-TRANSECT BINARY DIAGRAMS DISTINGUISHING THE CHEMOSTRATIGRAPHIC SEQUENCES AND PACKAGES OF THE MANDAWA BASIN OUTCROP SAMPLES

Figure A5.1. Claystone and sandstone-based binary diagrams distinguishing the chemostratigraphic sequences encountered at outcrop along North Mandawa Transect-1: samples colour coded by the lithostratigraphic assignment of Hudson (2010).

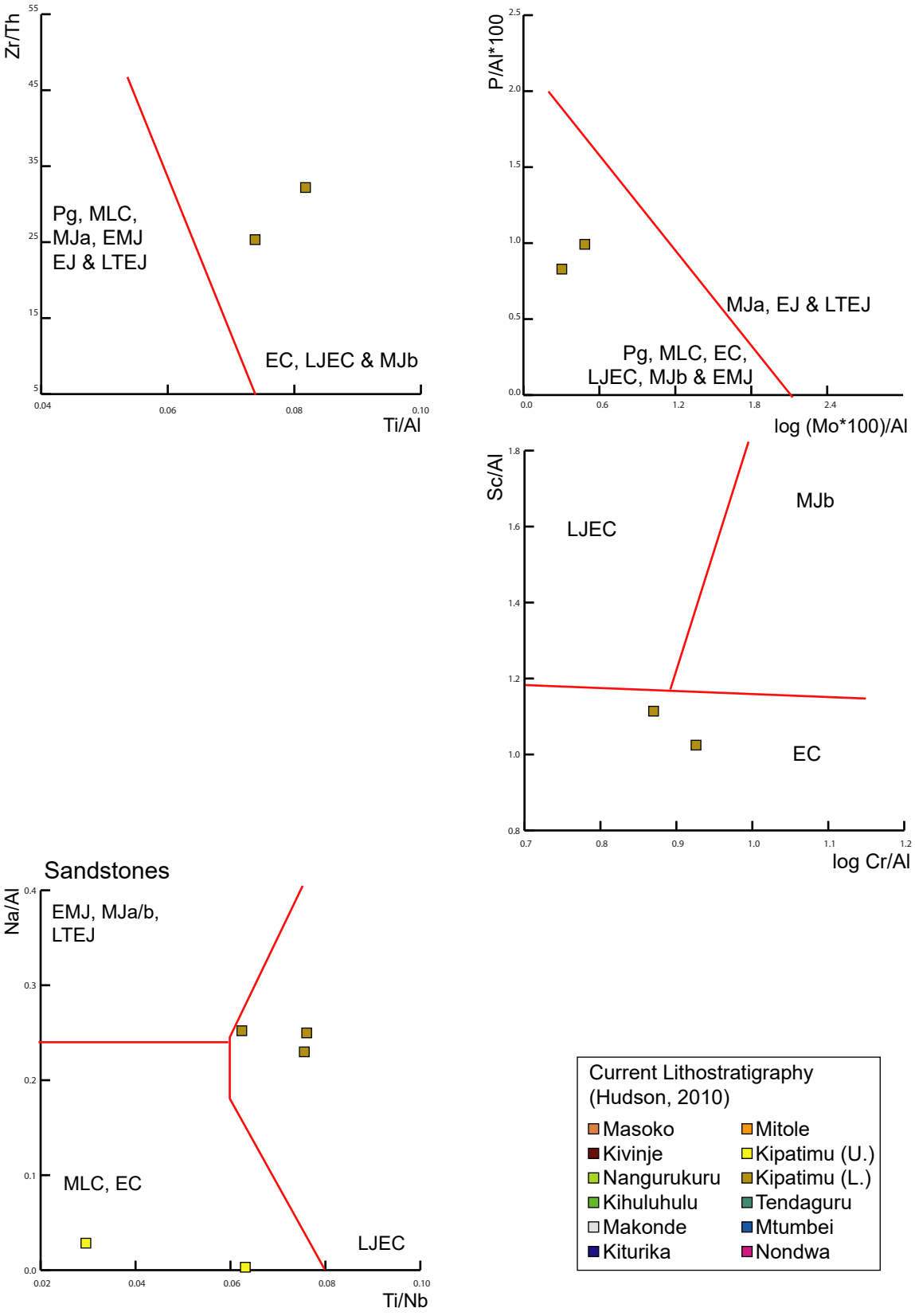

Figure A5.2. Claystone and sandstone-based binary diagrams distinguishing the chemostratigraphic sequences encountered at outcrop along North Mandawa Transect-1: samples colour coded by the chemostratigraphic assignment made in this thesis.

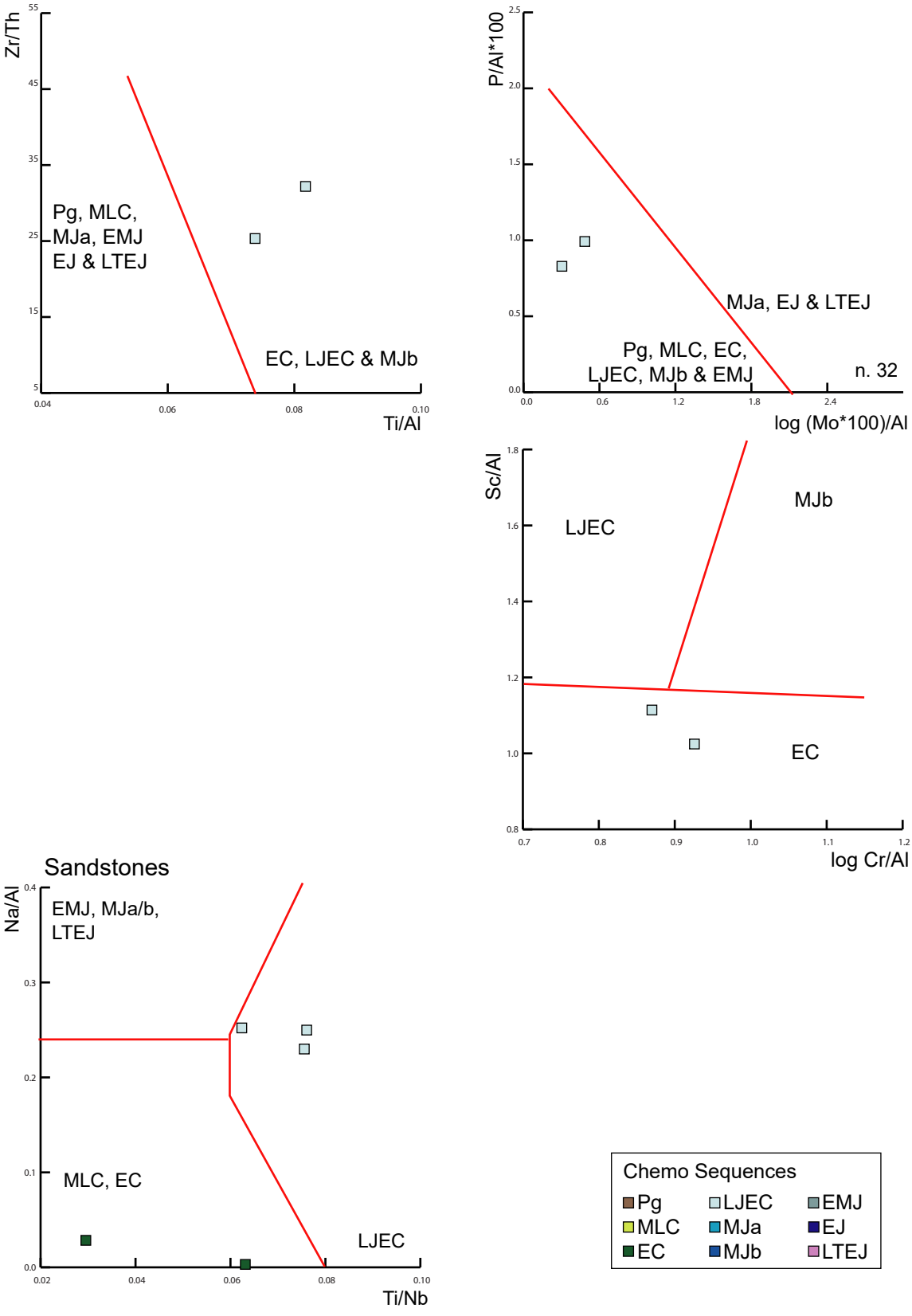

Figure A5.3. Claystone-based binary diagrams distinguishing the chemostratigraphic sequences encountered at outcrop along North Mandawa Transect-2: samples colour coded by the lithostratigraphic assignment of Hudson (2010).

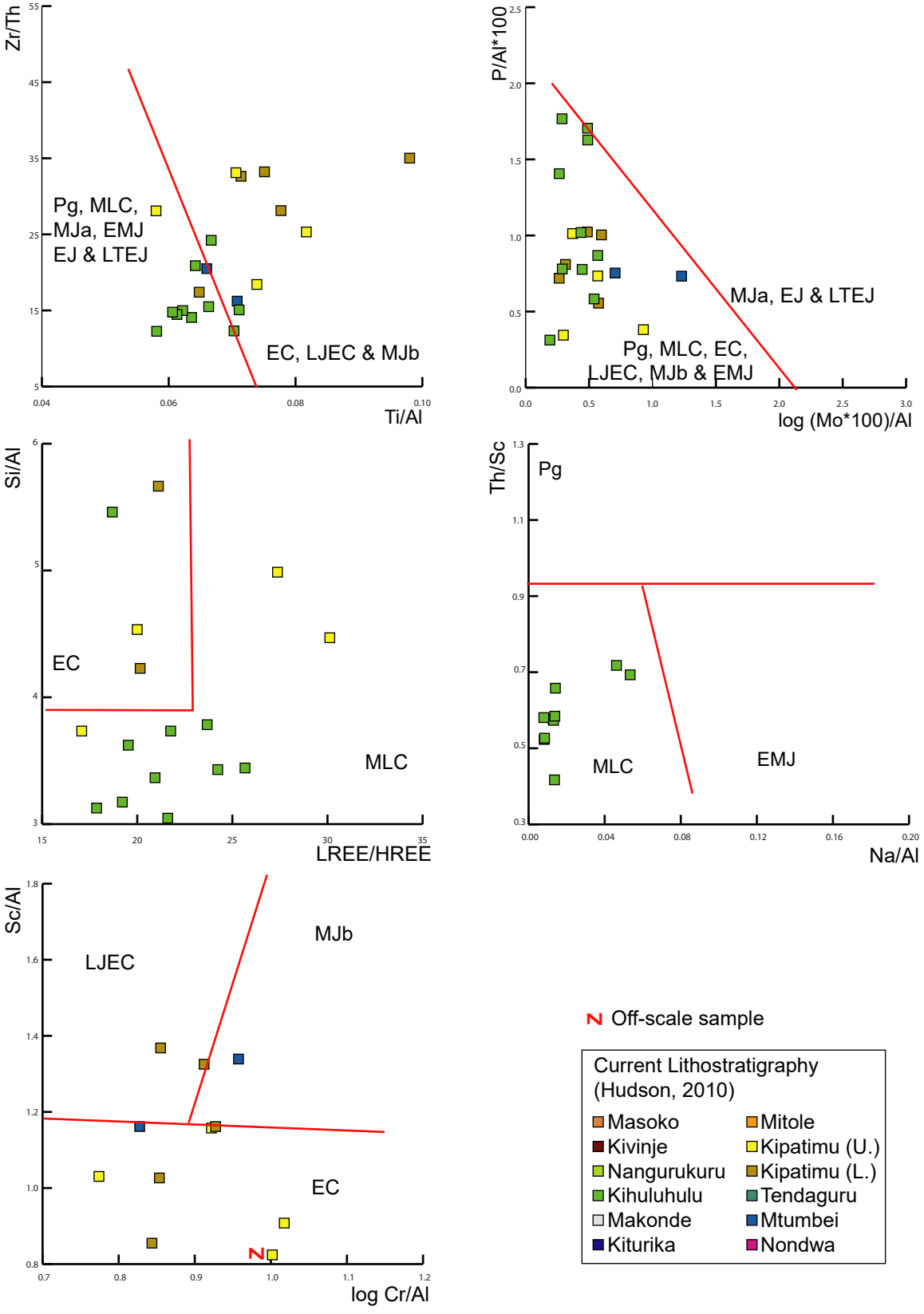

Figure A5.4. Claystone-based binary diagrams distinguishing the chemostratigraphic sequences encountered at outcrop along North Mandawa Transect-2: samples colour coded by the chemostratigraphic assignment made in this thesis.

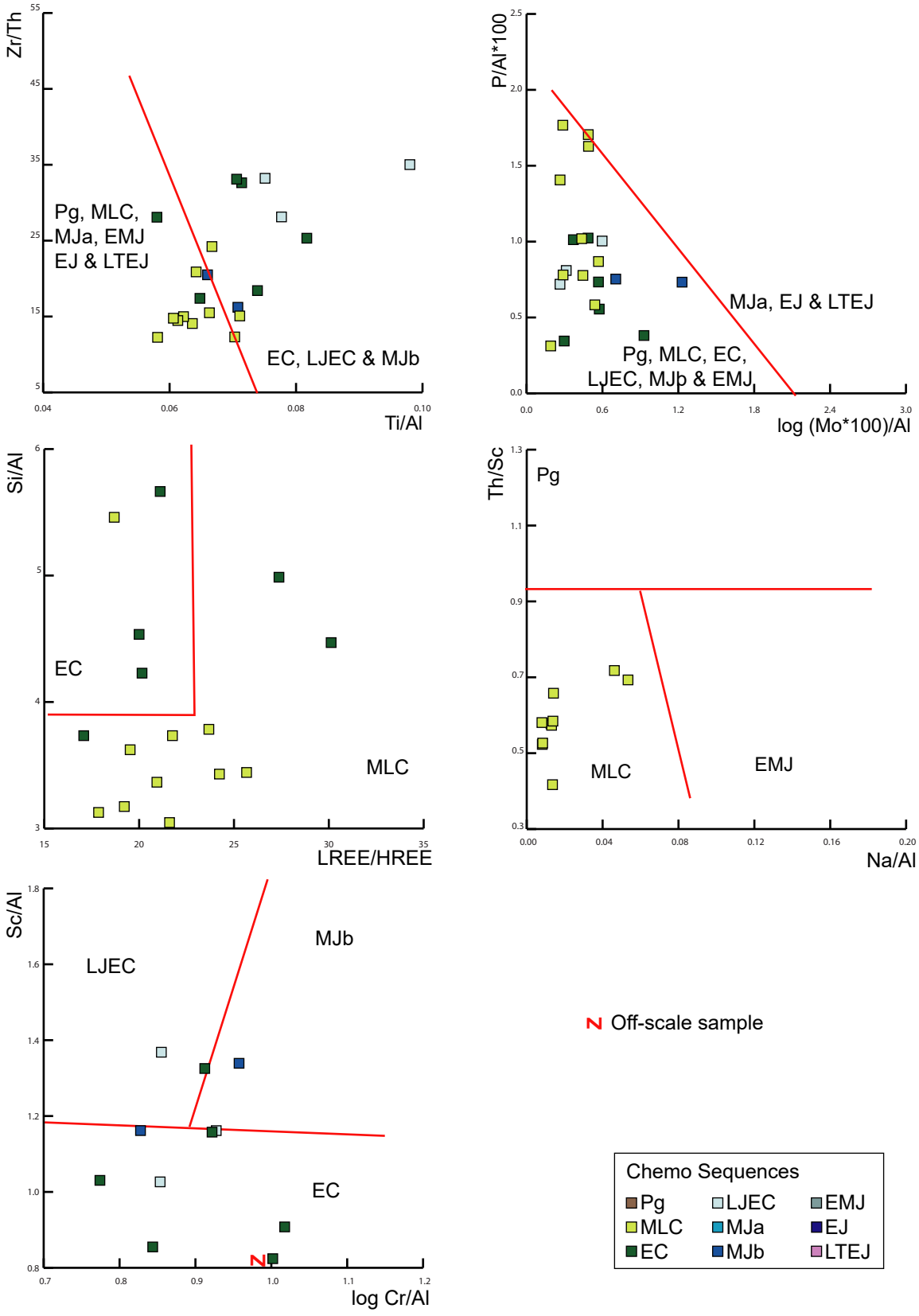

Figure A5.5. Sandstone-based binary diagram distinguishing the chemostratigraphic sequences encountered at outcrop along North Mandawa Transect-2: samples colour coded by the lithostratigraphic assignment of Hudson (2010) and chemostratigraphic assignment made in this thesis.

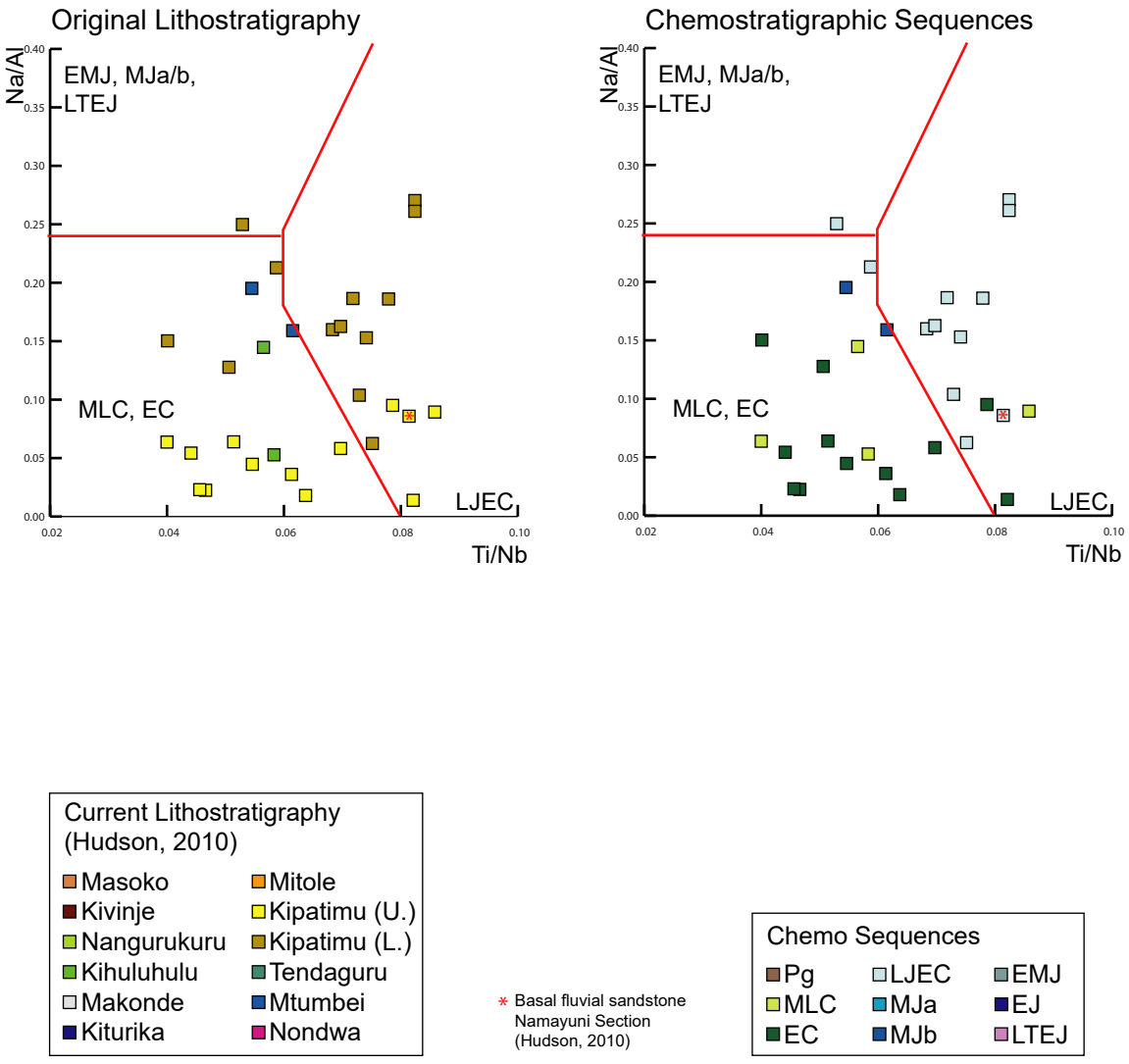

Figure A5.6. Claystone-based binary diagrams distinguishing the chemostratigraphic sequences encountered at outcrop along North Mandawa Transect-3: samples colour coded by the lithostratigraphic assignment of Hudson (2010).

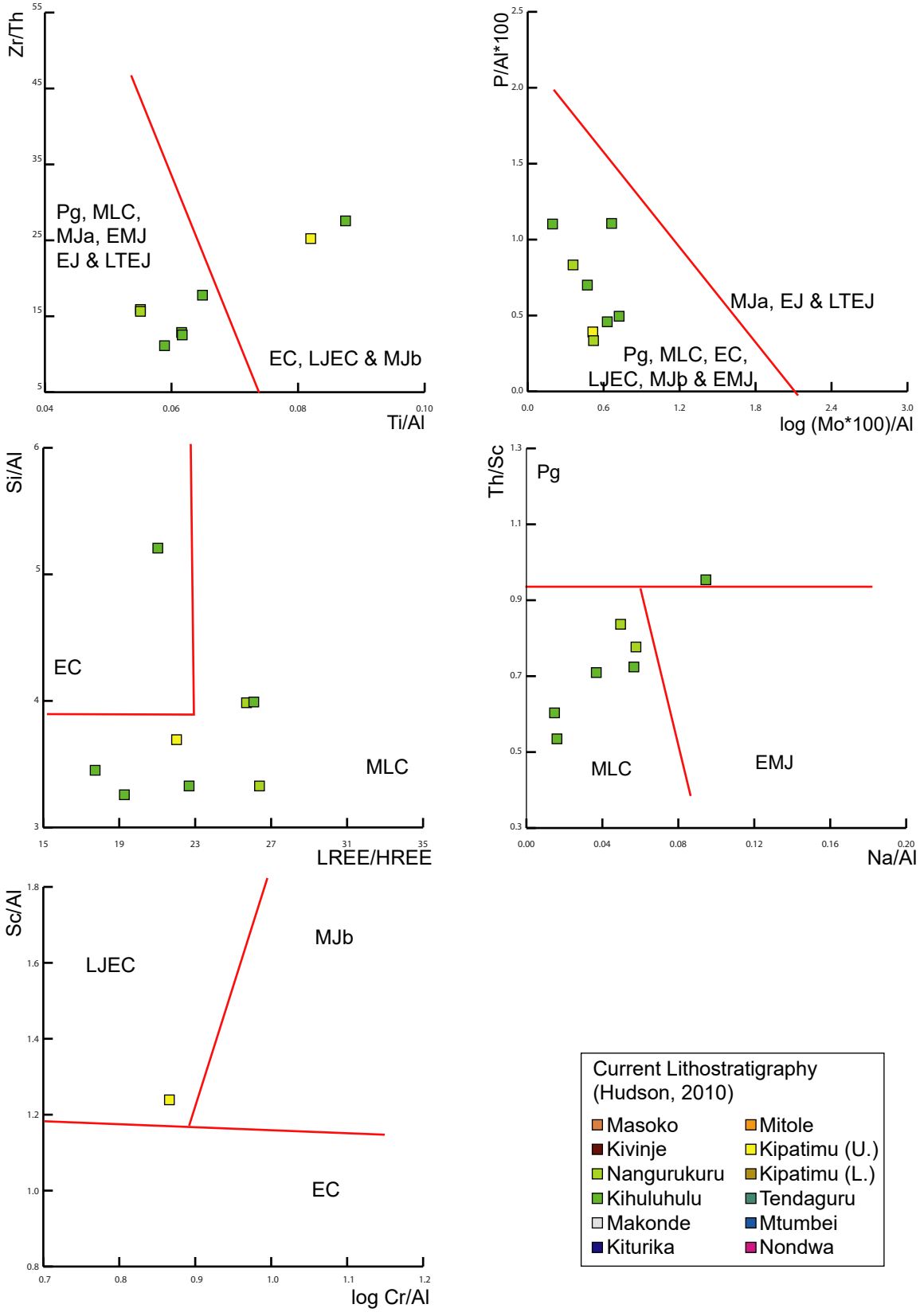

Figure A5.7. Claystone-based binary diagrams distinguishing the chemostratigraphic sequences encountered at outcrop along North Mandawa Transect-3: samples colour coded by the chemostratigraphic assignment made in this thesis.

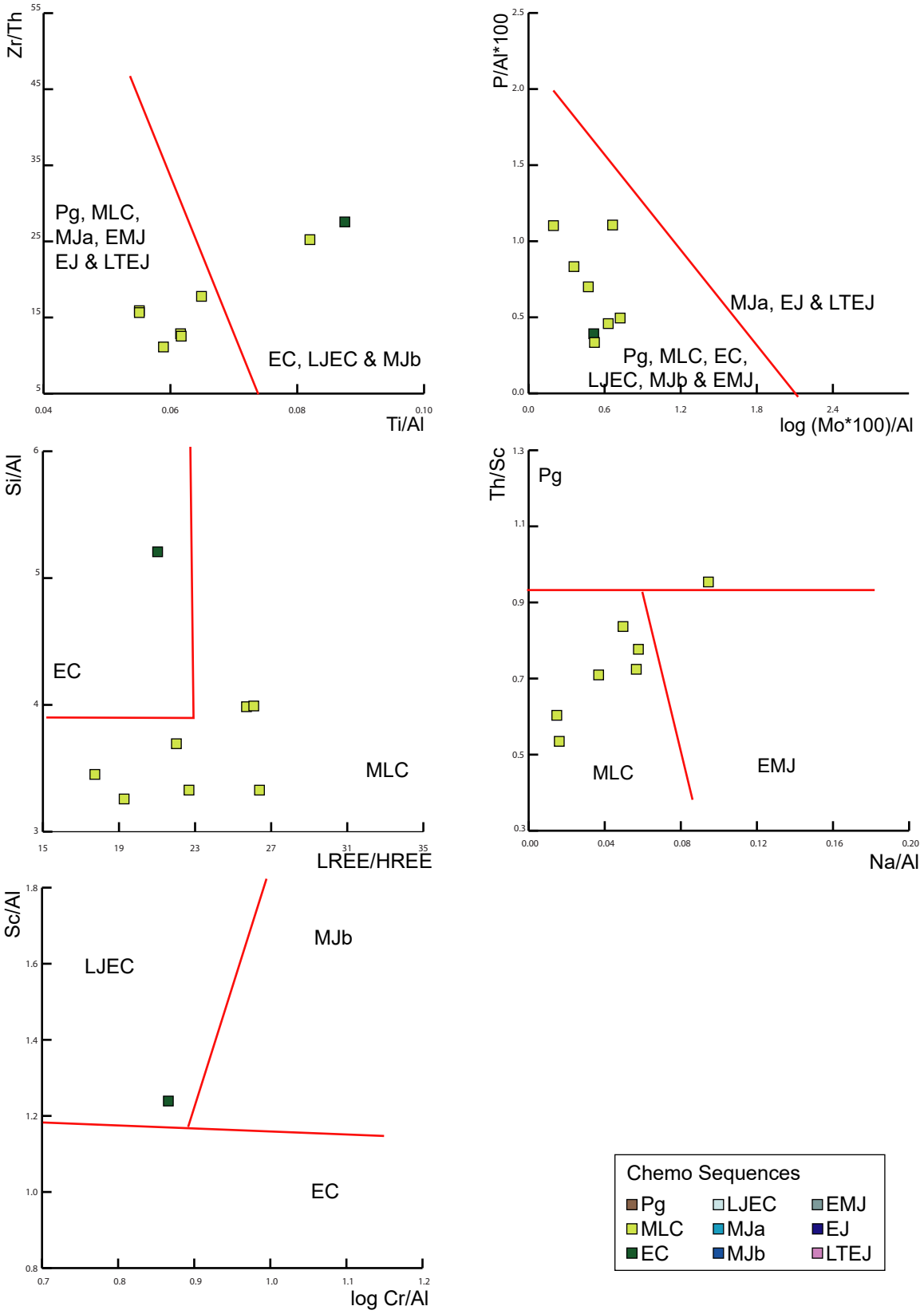

Figure A5.8. Sandstone-based binary diagram distinguishing the chemostratigraphic sequences encountered at outcrop along North Mandawa Transect-3: samples colour coded by the lithostratigraphic assignment of Hudson (2010) and chemostratigraphic assignment made in this thesis.

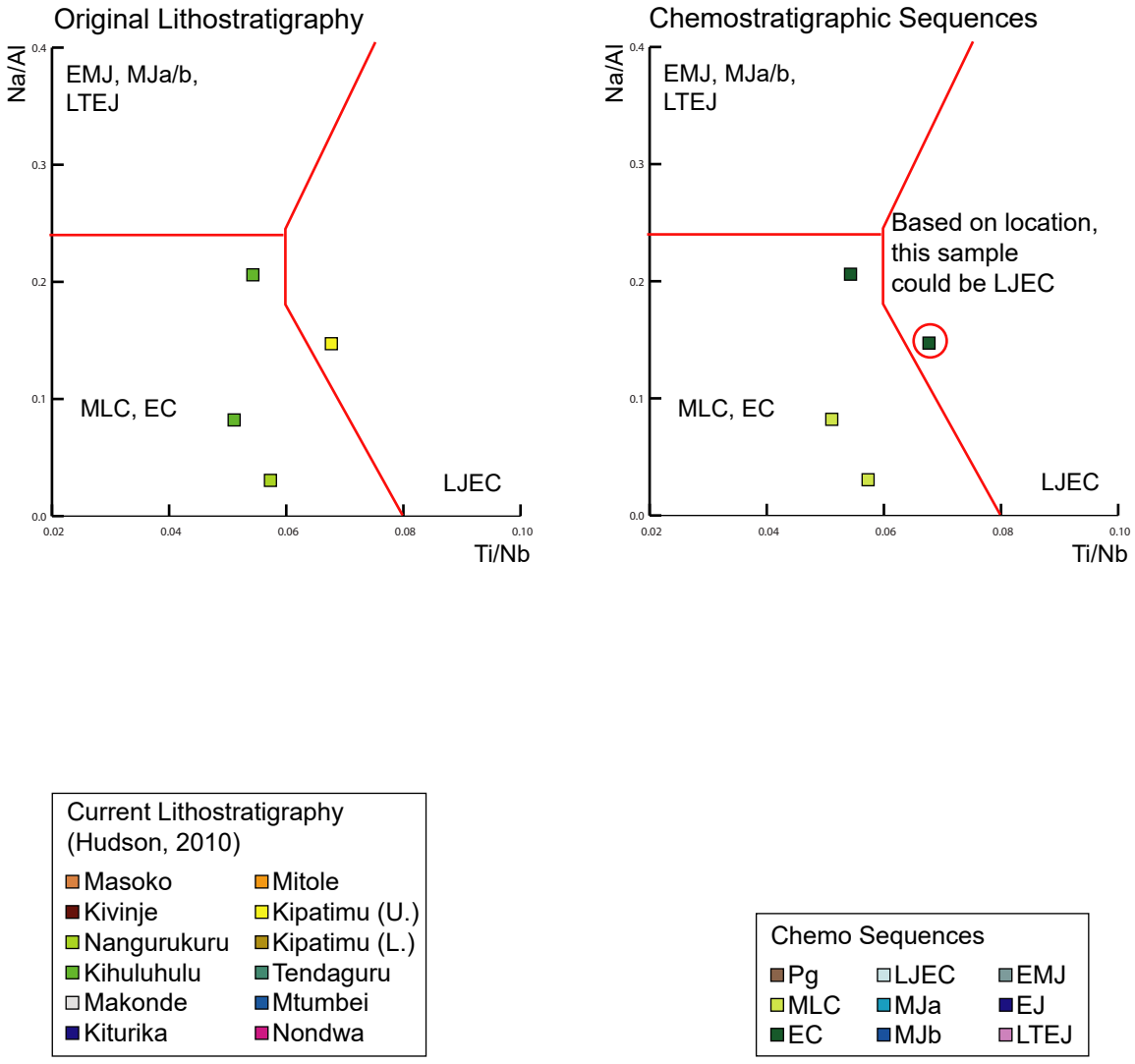

Figure A5.9. Claystone-based binary diagrams distinguishing the chemostratigraphic sequences encountered at outcrop along South Mandawa Transect-1: samples colour coded by the lithostratigraphic assignment of Hudson (2010).

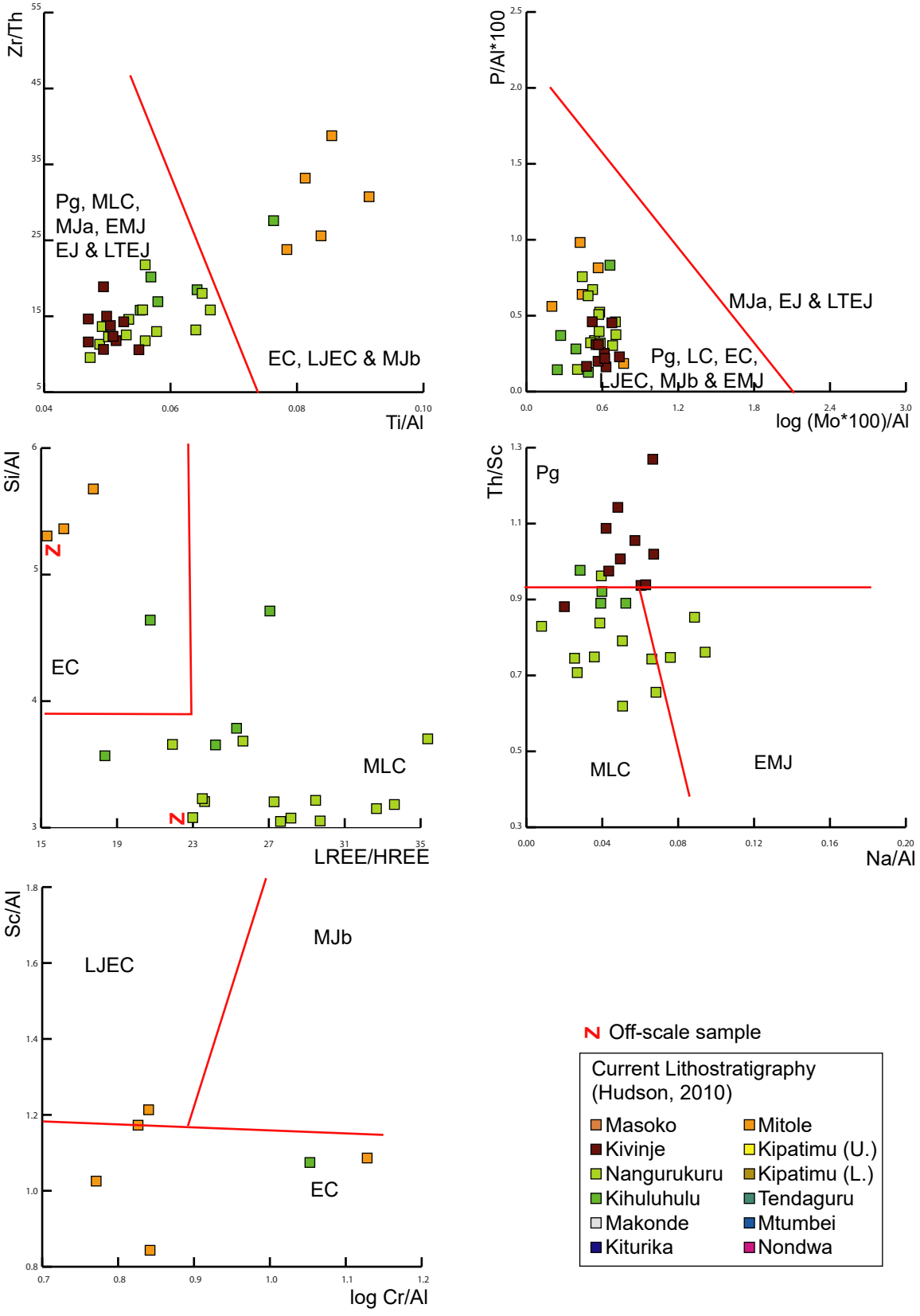

Figure A5.10. Claystone-based binary diagrams distinguishing the chemostratigraphic sequences encountered at outcrop along South Mandawa Transect-1: samples colour coded by the chemostratigraphic assignment made in this thesis.

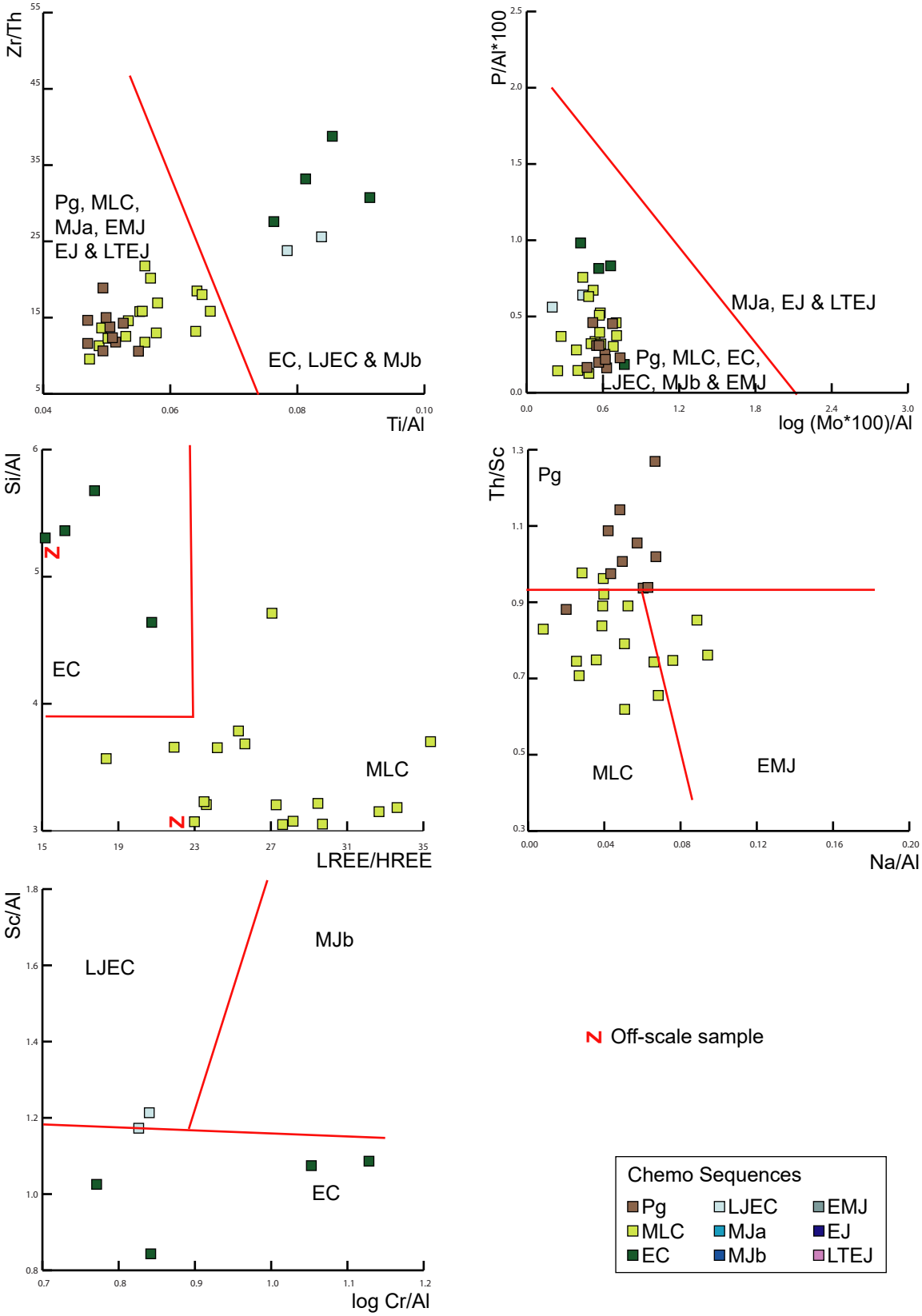

Figure A5.11. Sandstone-based binary diagram distinguishing the chemostratigraphic sequences encountered at outcrop along South Mandawa Transect-1: samples colour coded by the lithostratigraphic assignment of Hudson (2010) and chemostratigraphic assignment made in this thesis.

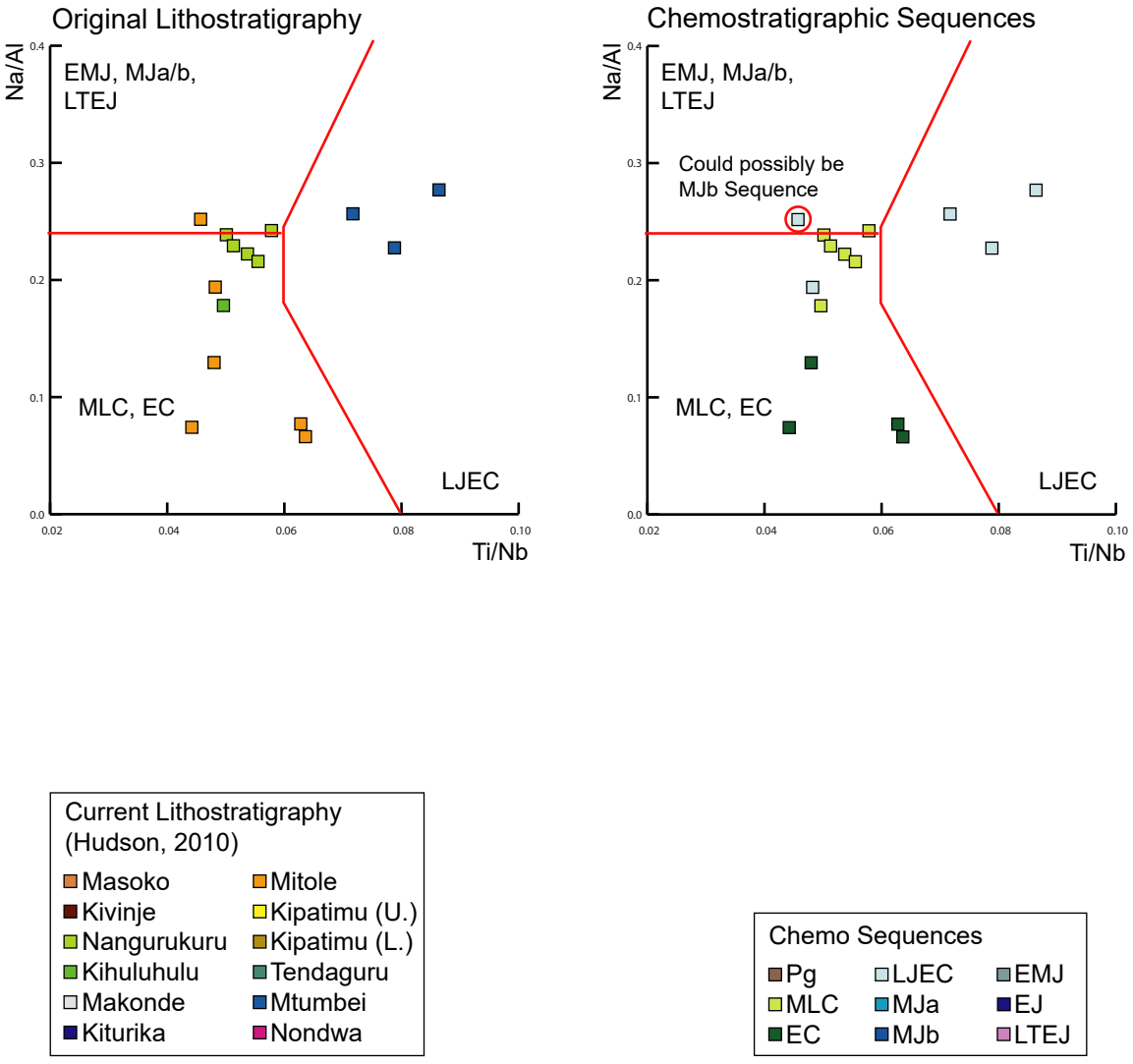

Figure A5.12. Claystone-based binary diagrams distinguishing the chemostratigraphic sequences encountered at outcrop along South Mandawa Transect-2: samples colour coded by the lithostratigraphic assignment of Hudson (2010).

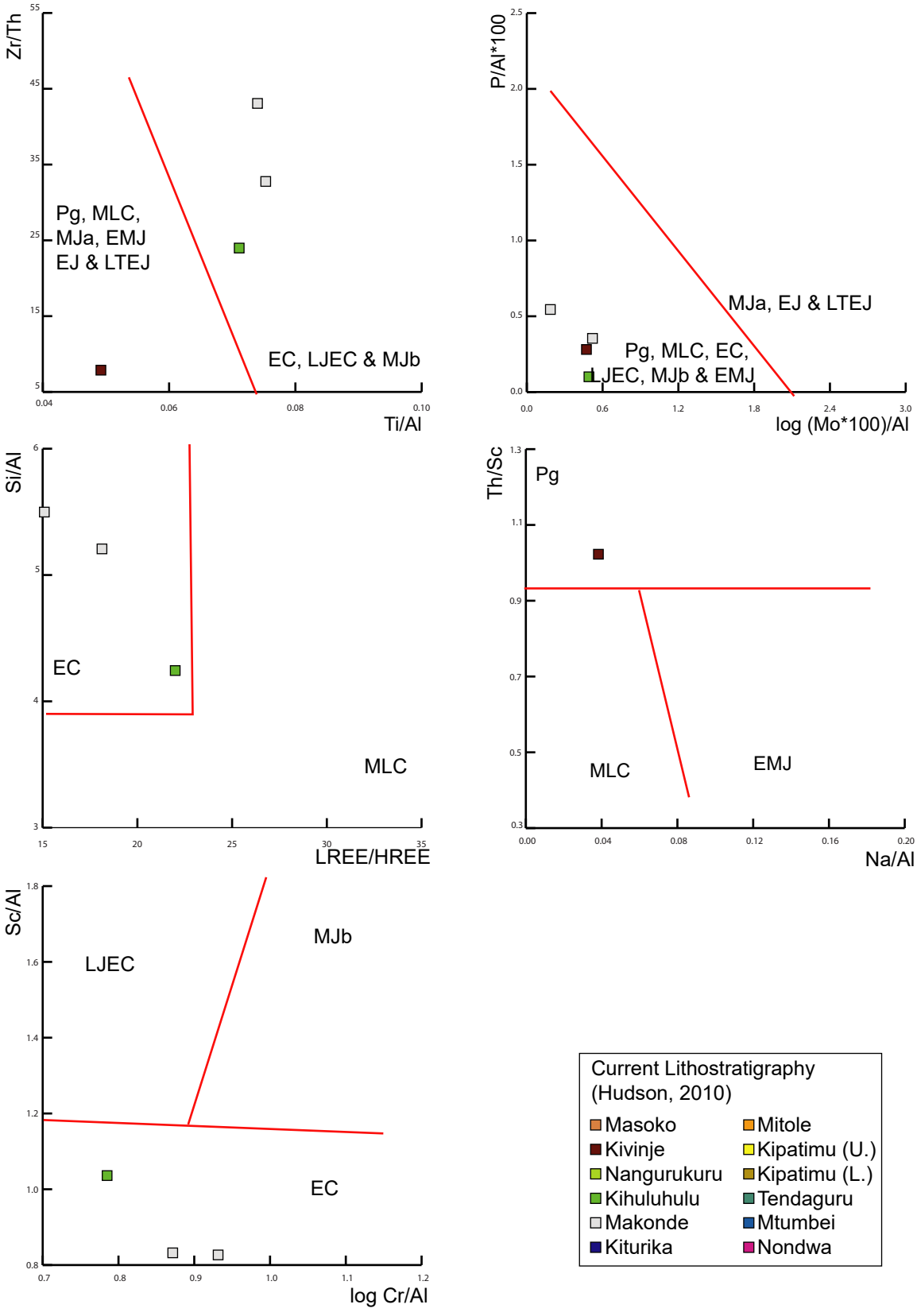

Figure A5.13. Claystone-based binary diagrams distinguishing the chemostratigraphic sequences encountered at outcrop along South Mandawa Transect-2: samples colour coded by the chemostratigraphic assignment made in this thesis.

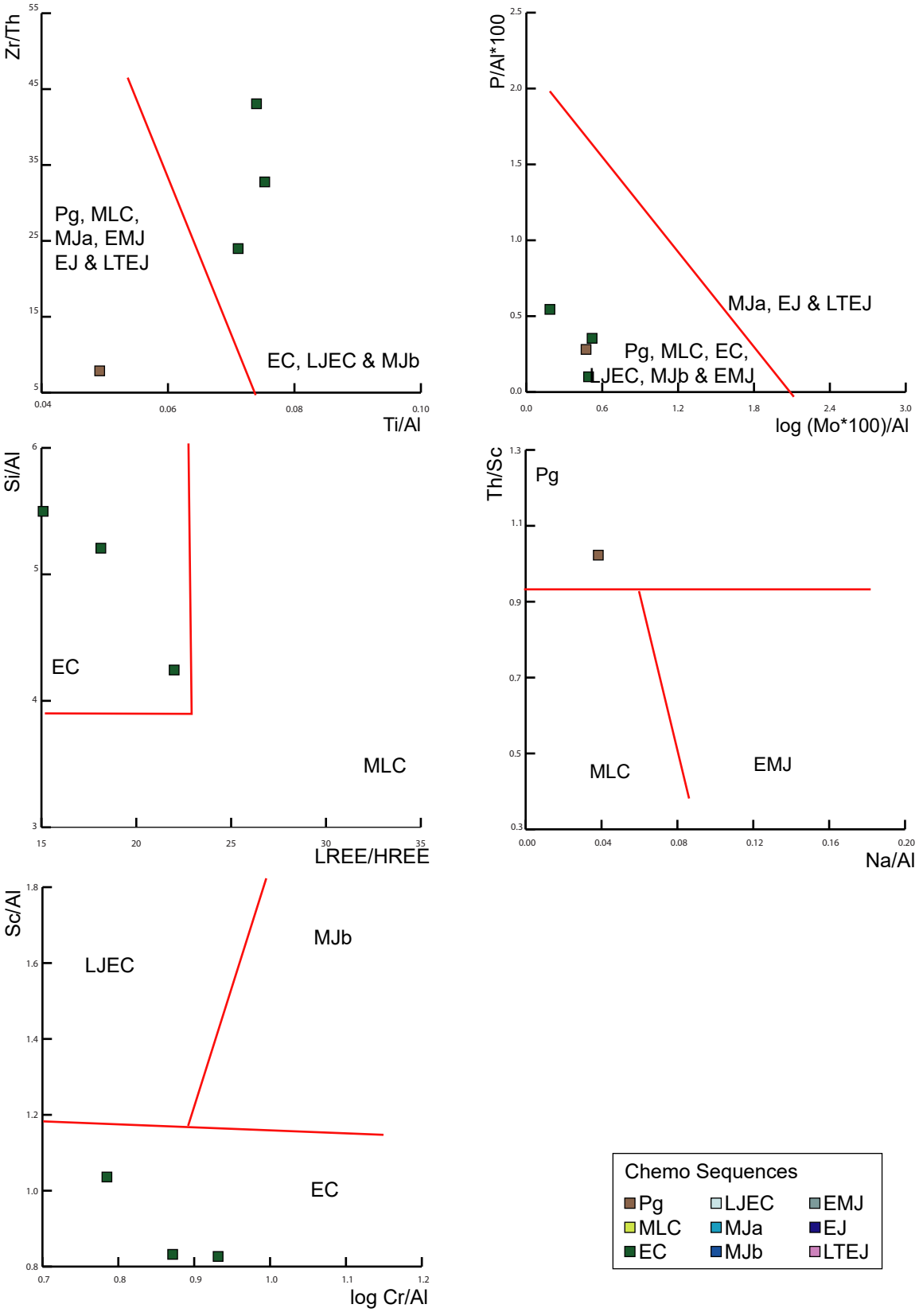

Figure A5.14. Sandstone-based binary diagram distinguishing the chemostratigraphic sequences encountered at outcrop along South Mandawa Transect-2: samples colour coded by the lithostratigraphic assignment of Hudson (2010) and chemostratigraphic assignment made in this thesis.

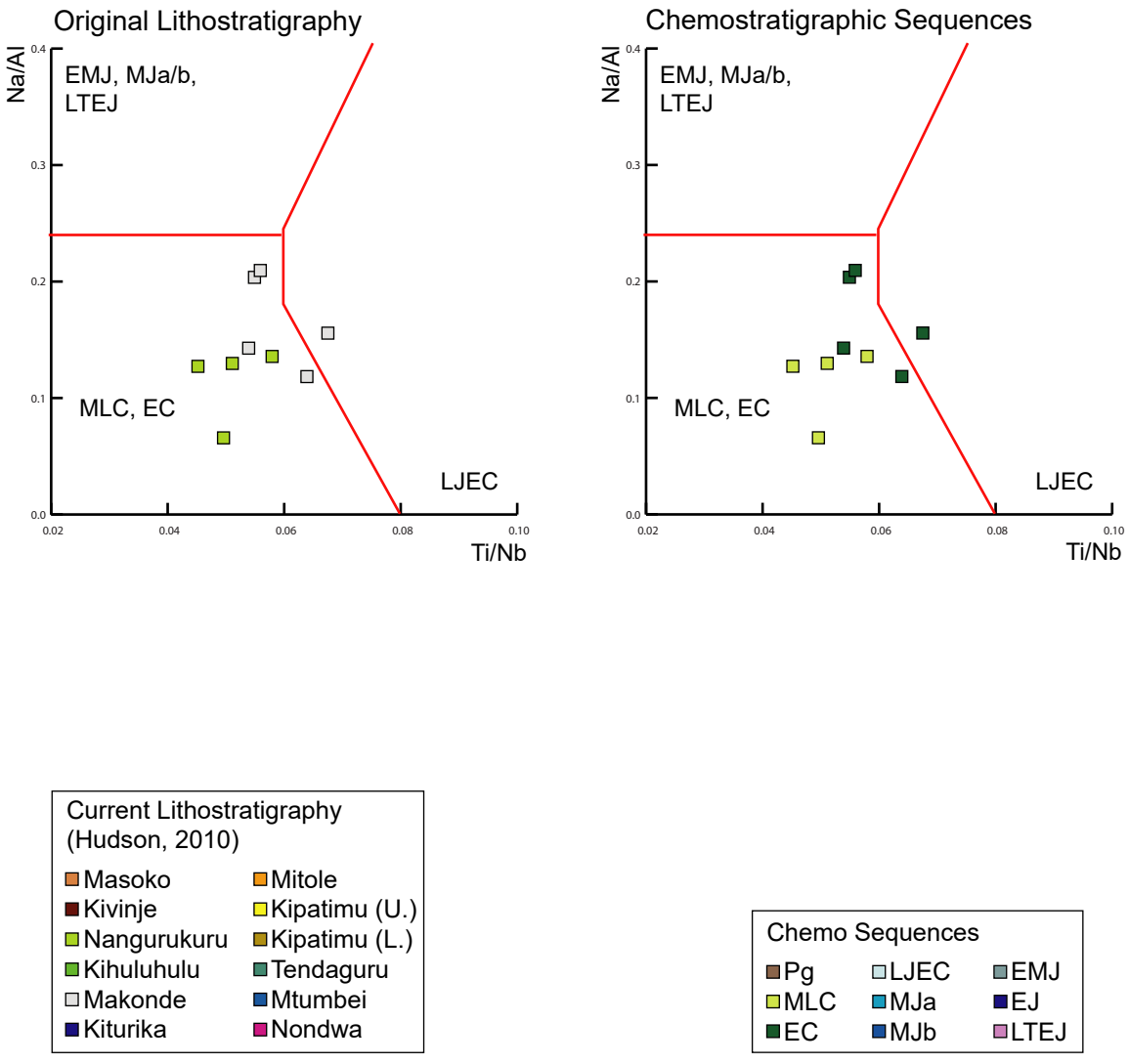

Figure A5.15. Claystone-based binary diagrams distinguishing the chemostratigraphic sequences encountered at outcrop along South Mandawa Transect-3: samples colour coded by the lithostratigraphic assignment of Hudson (2010).

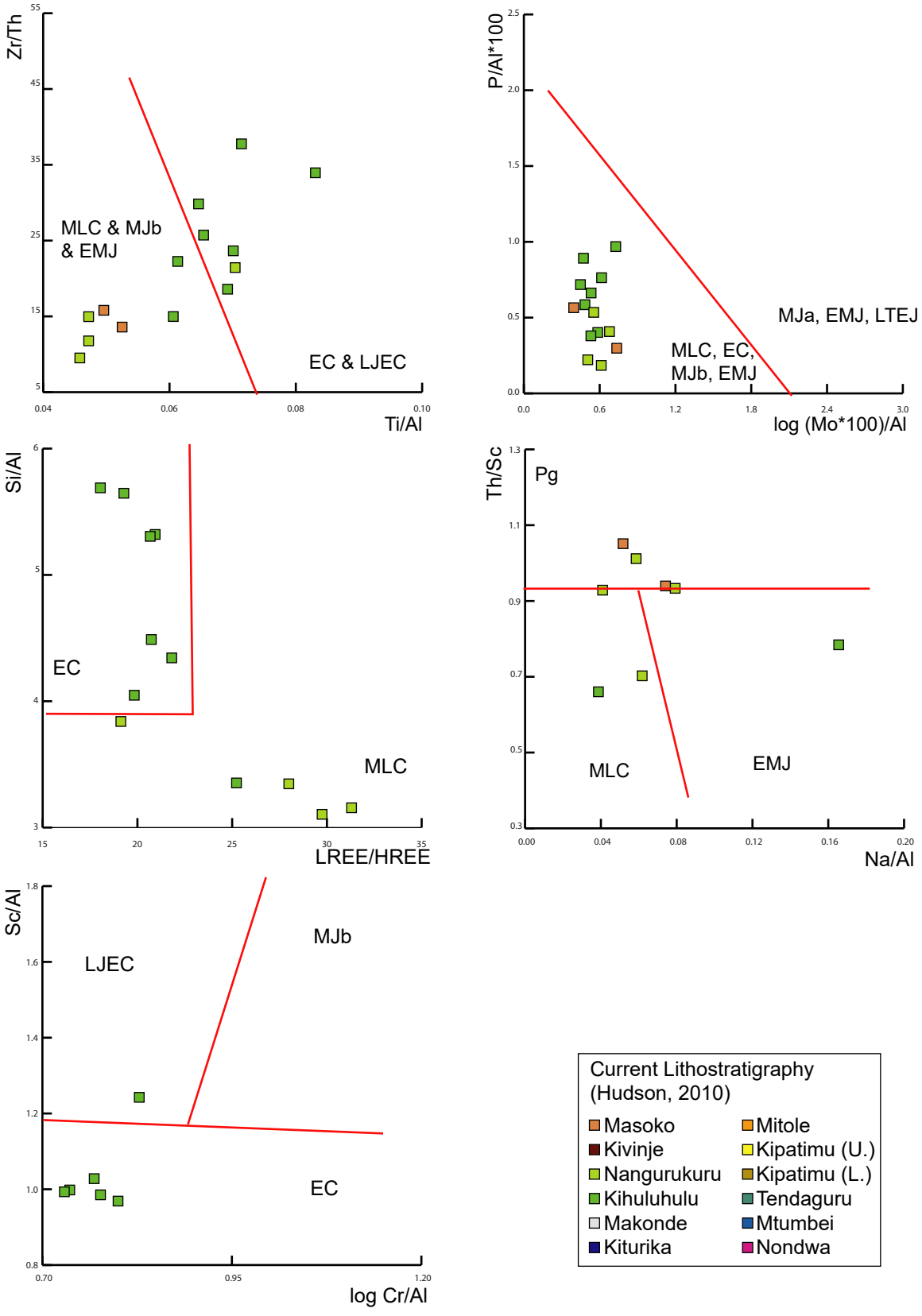

Figure A5.16. Claystone-based binary diagrams distinguishing the chemostratigraphic sequences encountered at outcrop along South Mandawa Transect-3: samples colour coded by the chemostratigraphic assignment made in this thesis.

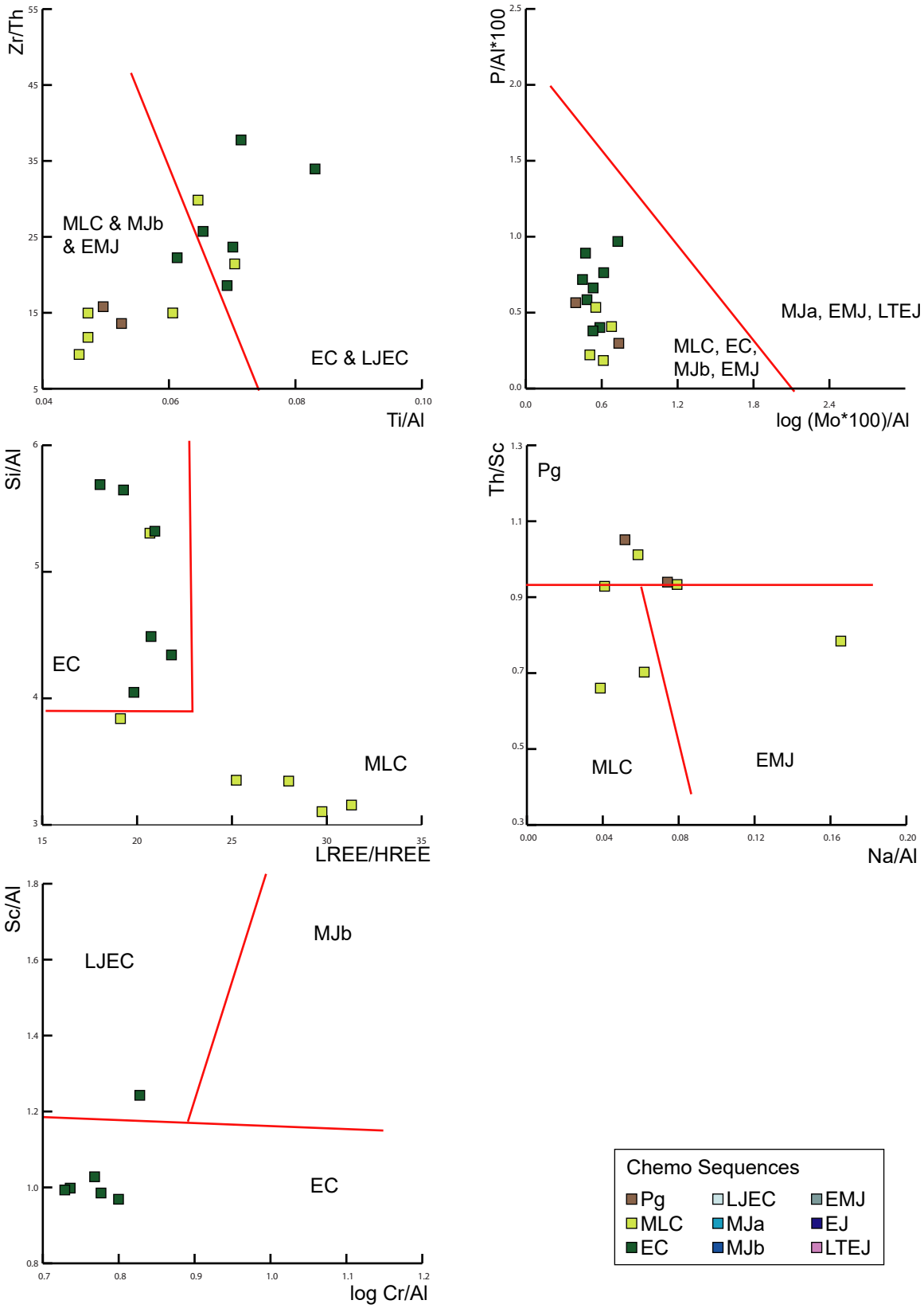

5Figure A5.17. Sandstone-based binary diagram distinguishing the chemostratigraphic sequences encountered at outcrop along South Mandawa Transect-3: samples colour coded by the lithostratigraphic assignment of Hudson (2010) and chemostratigraphic assignment made in this thesis.

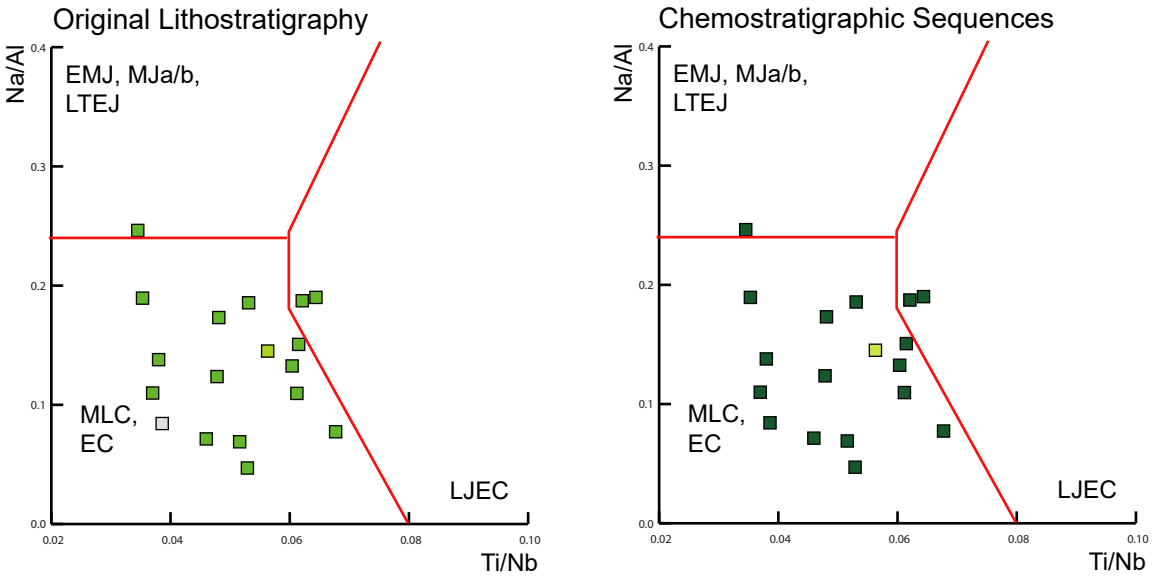

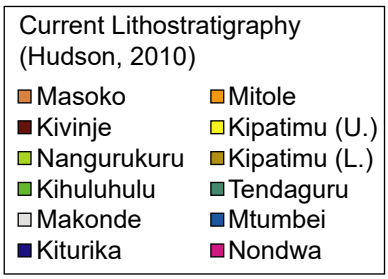

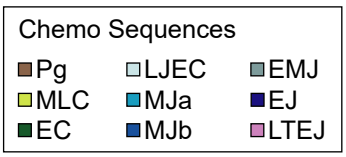

Figure A5.18. Claystone-based binary diagrams distinguishing the chemostratigraphic sequences encountered at outcrop along South Mandawa Transect-4: samples colour coded by the lithostratigraphic assignment of Hudson (2010).

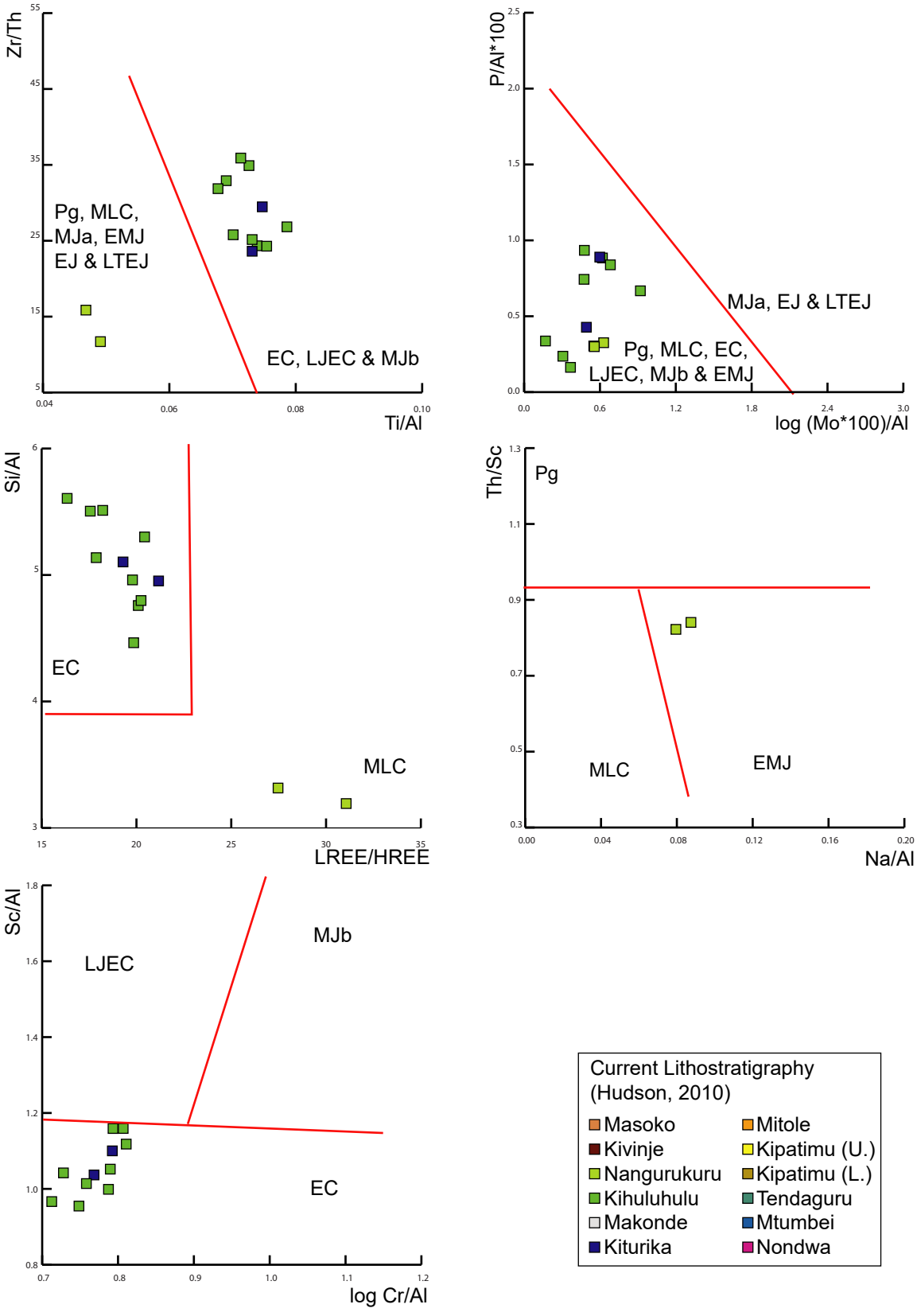

Figure A5.19. Claystone-based binary diagrams distinguishing the chemostratigraphic sequences encountered at outcrop along South Mandawa Transect-4: samples colour coded by the chemostratigraphic assignment made in this thesis.

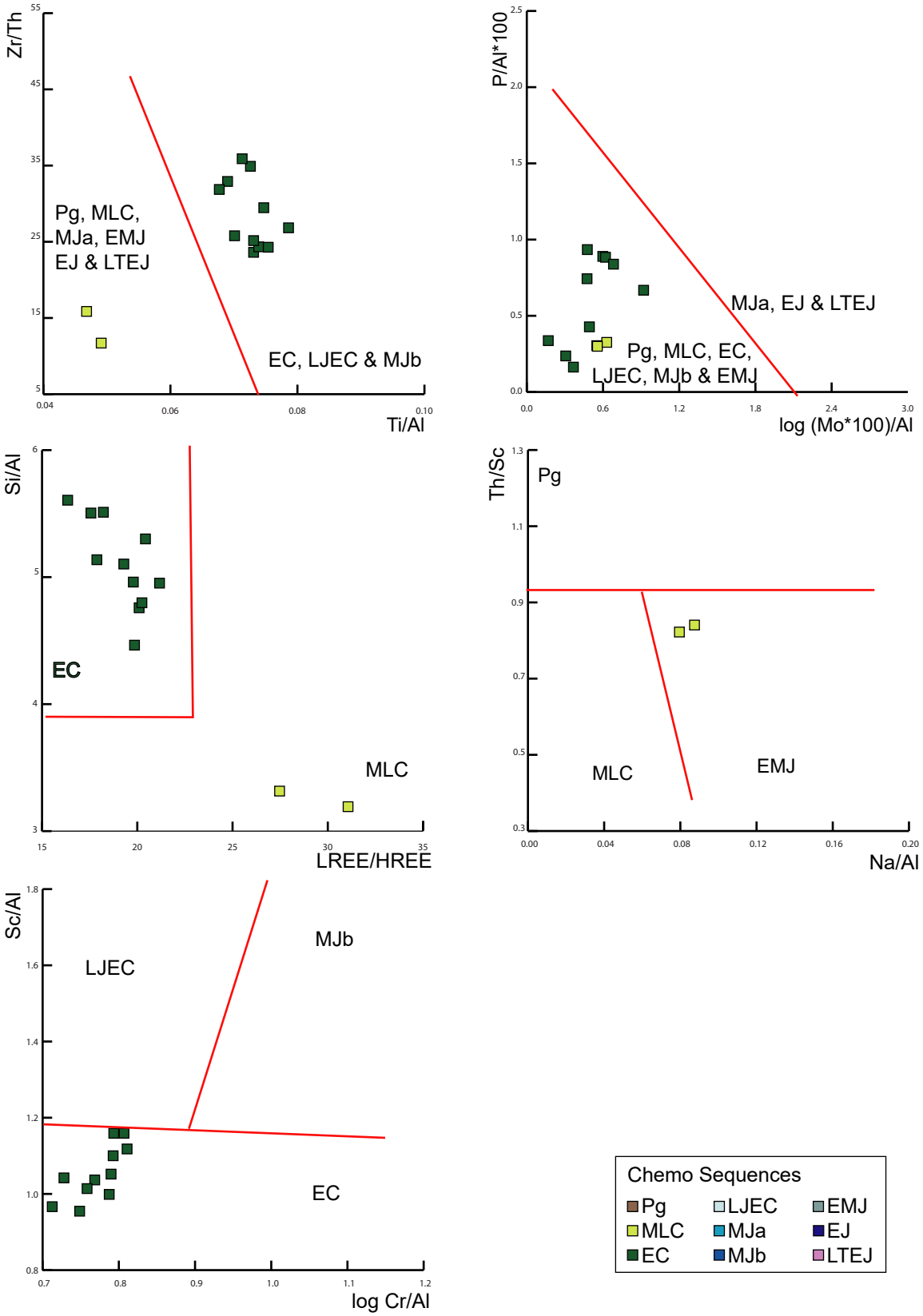

Figure A5.20. Sandstone-based binary diagram distinguishing the chemostratigraphic sequences encountered at outcrop along South Mandawa Transect-4: samples colour coded by the lithostratigraphic assignment of Hudson (2010) and chemostratigraphic assignment made in this thesis.

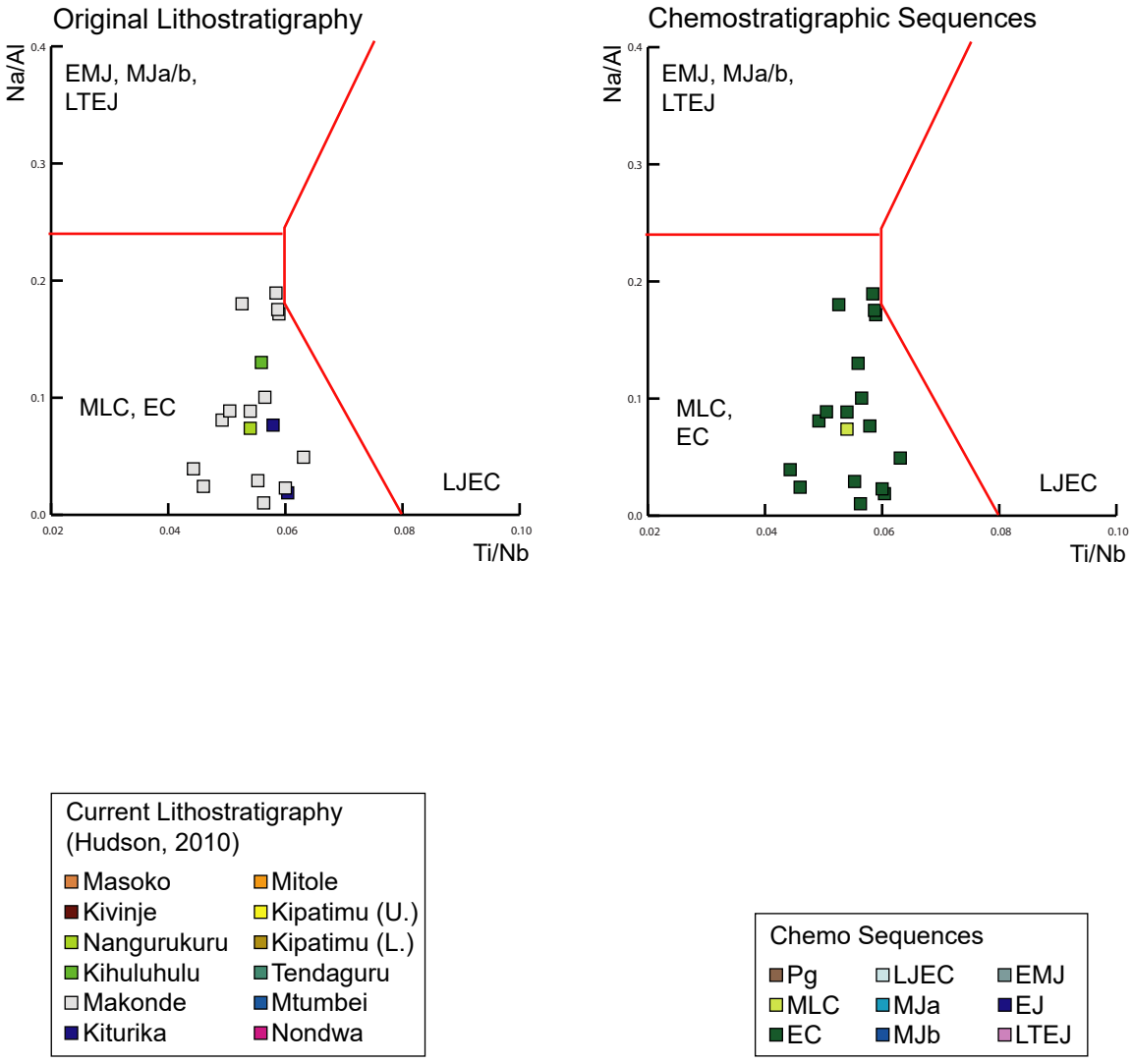

Figure A5.21. Claystone-based binary diagrams distinguishing the chemostratigraphic sequences encountered at outcrop along South Mandawa Transect-5: samples colour coded by the lithostratigraphic assignment of Hudson (2010).

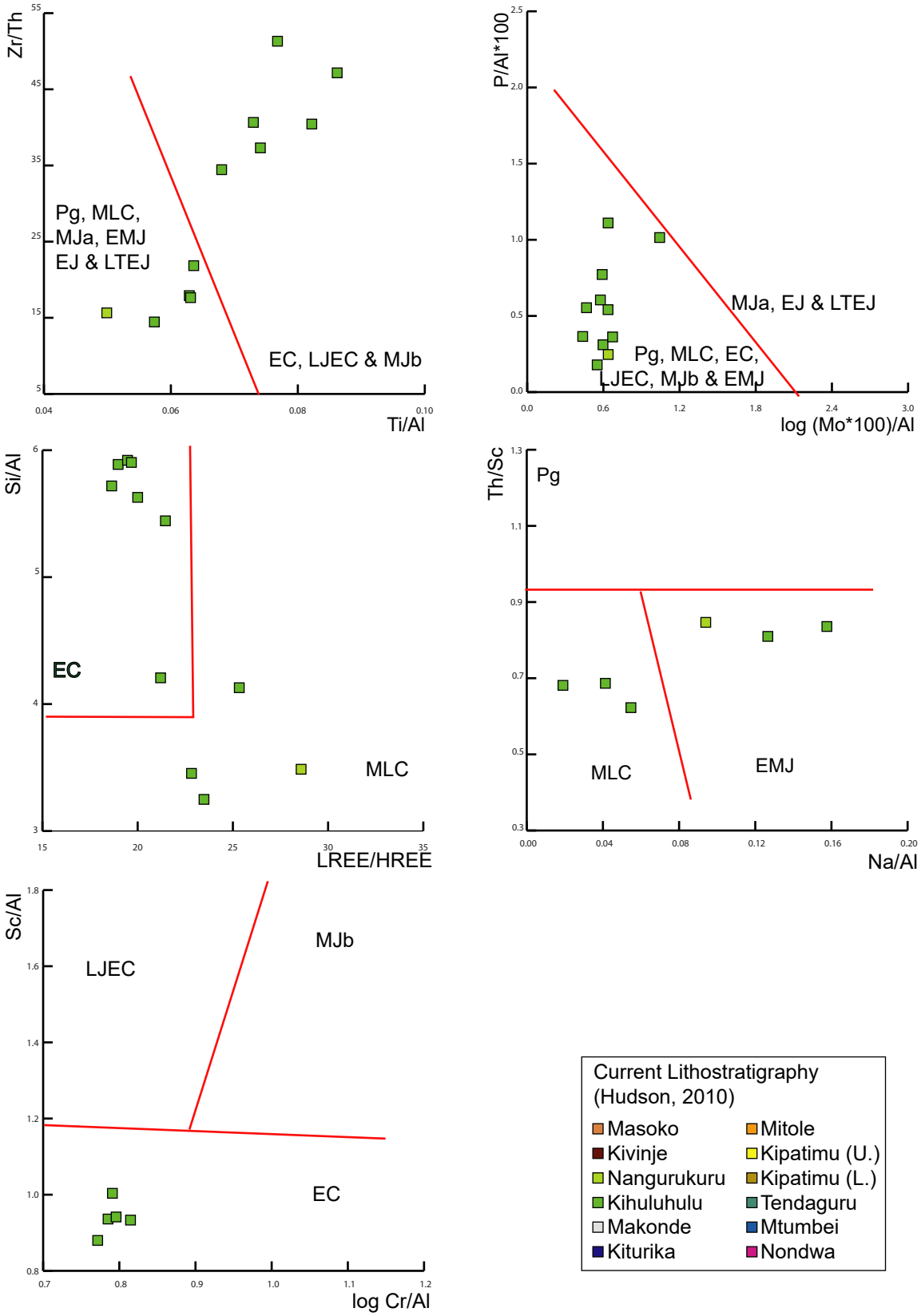

Figure A5.22. Claystone-based binary diagrams distinguishing the chemostratigraphic sequences encountered at outcrop along South Mandawa Transect-5: samples colour coded by the chemostratigraphic assignment made in this thesis.

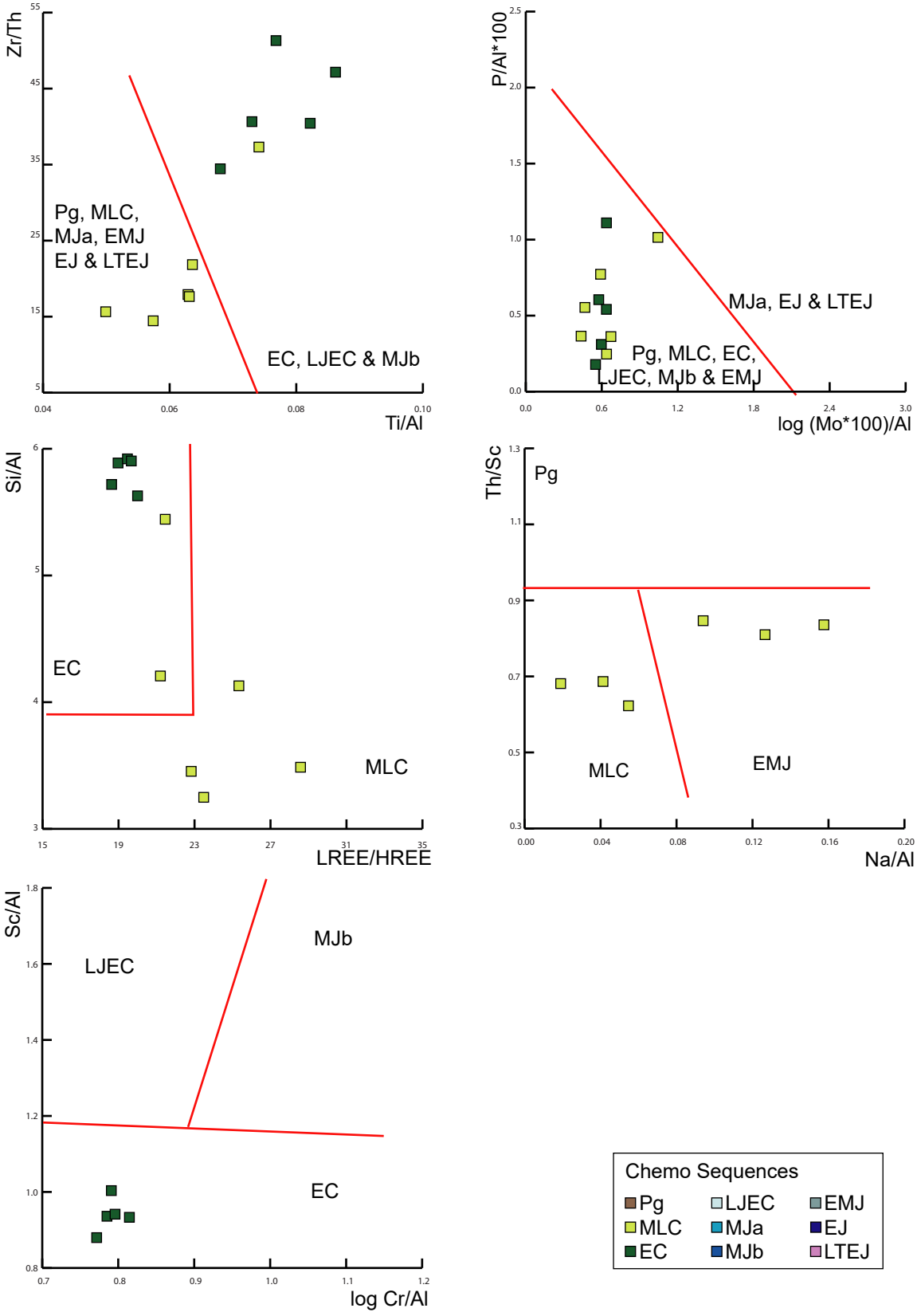

Figure A5.23. Sandstone-based binary diagram distinguishing the chemostratigraphic sequences encountered at outcrop along South Mandawa Transect-5: samples colour coded by the lithostratigraphic assignment of Hudson (2010) and chemostratigraphic assignment made in this thesis.

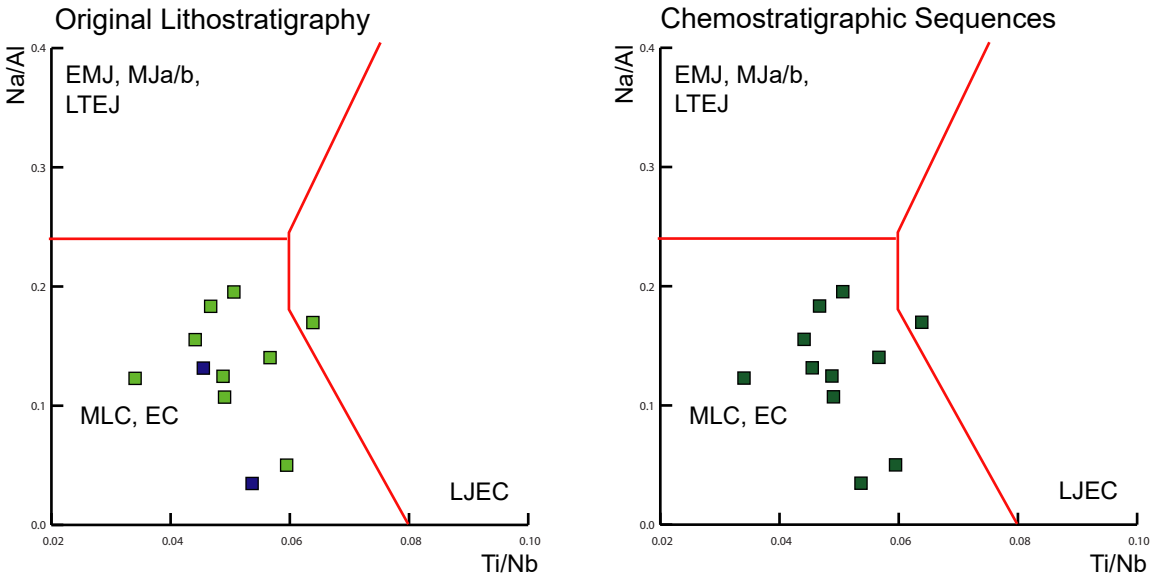

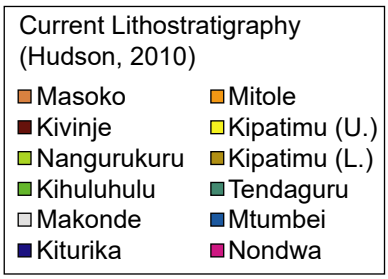

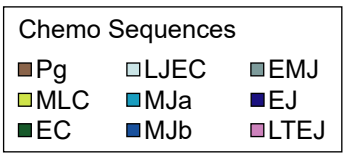

Figure A5.24. Claystone-based binary diagrams distinguishing the chemostratigraphic sequences encountered at outcrop along South Mandawa Transect-6: samples colour coded by the lithostratigraphic assignment of Hudson (2010).

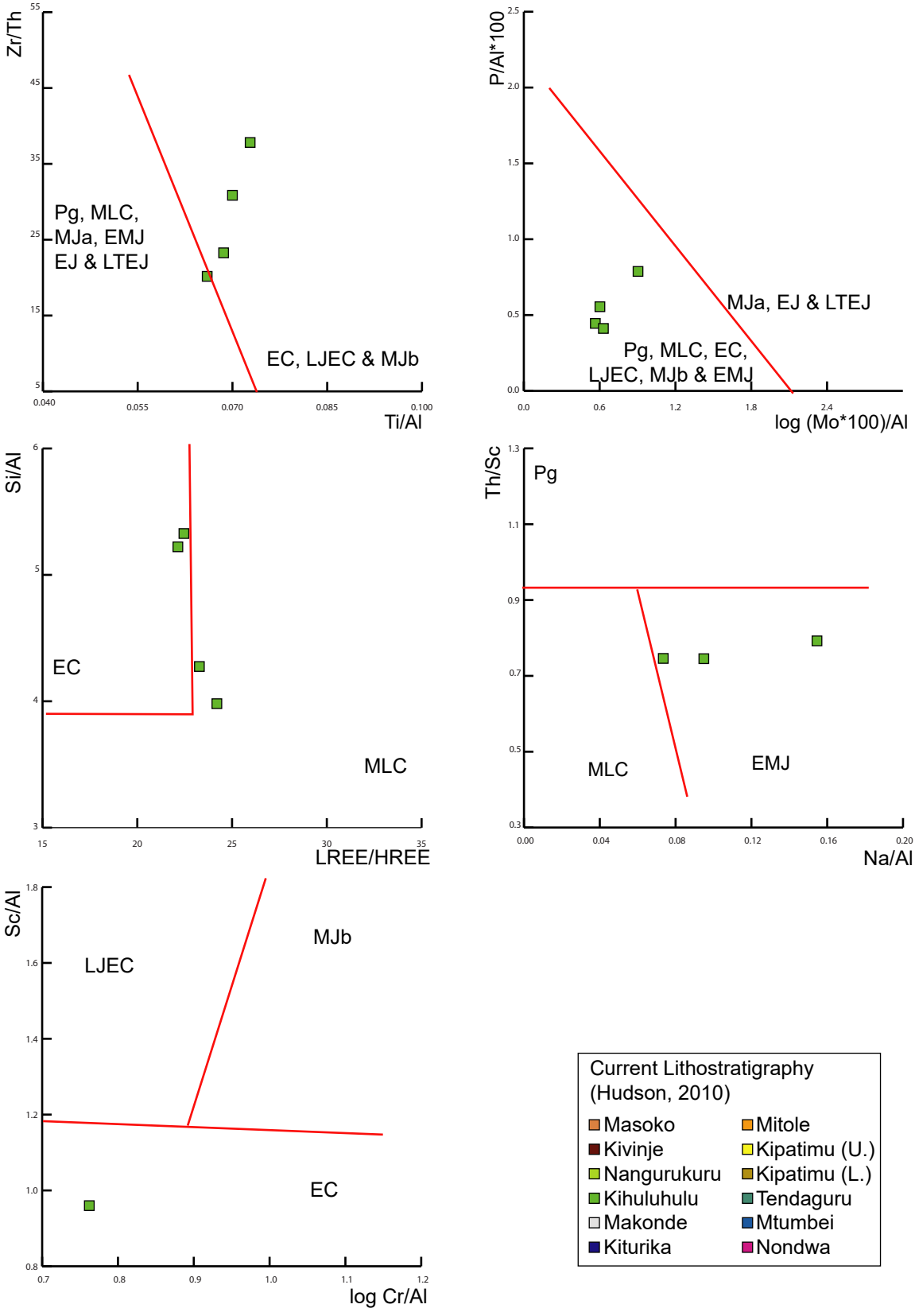

Figure A5.25. Claystone-based binary diagrams distinguishing the chemostratigraphic sequences encountered at outcrop along South Mandawa Transect-6: samples colour coded by the chemostratigraphic assignment made in this thesis.

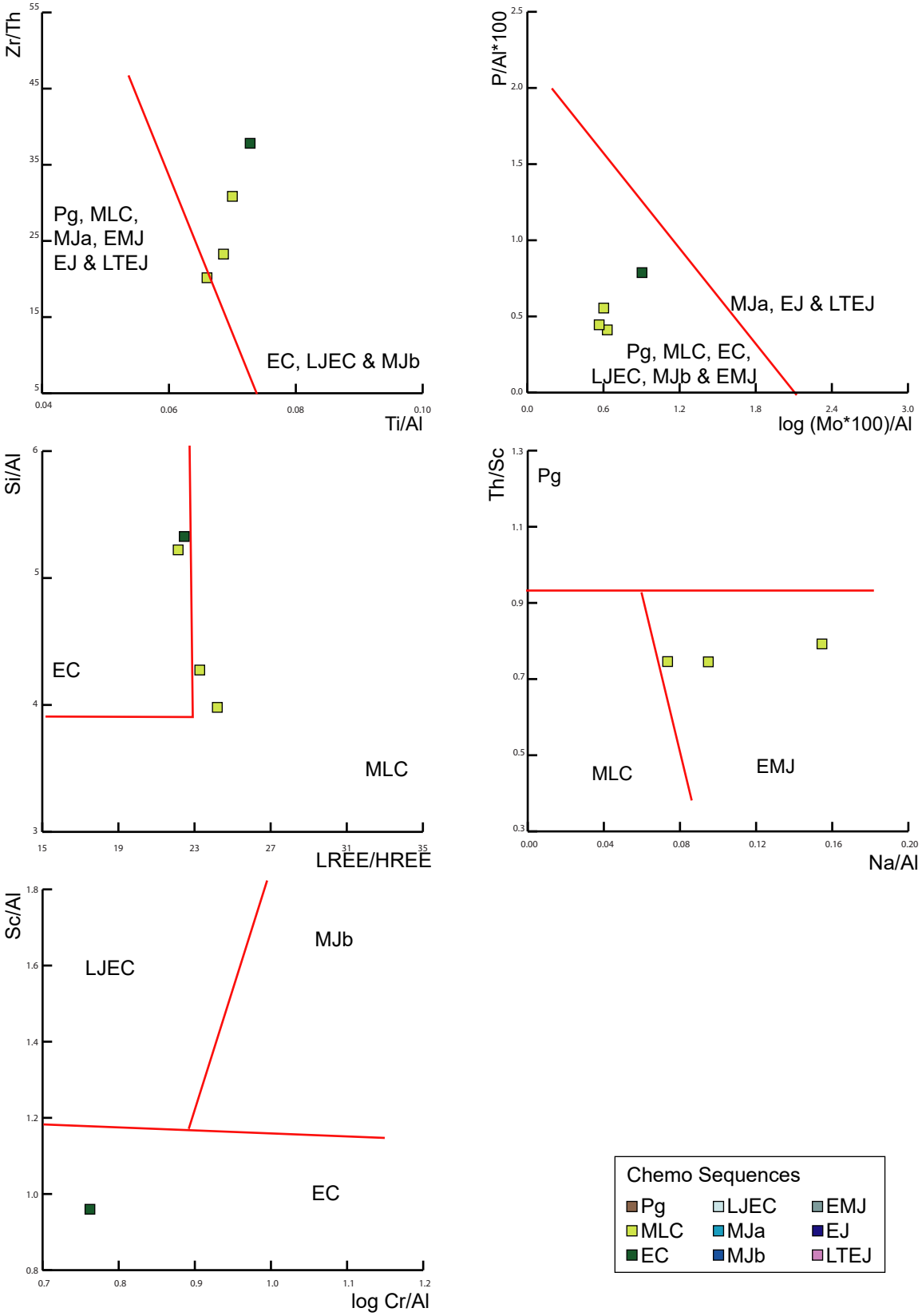

Figure A5.26. Sandstone-based binary diagram distinguishing the chemostratigraphic sequences encountered at outcrop along South Mandawa Transect-6: samples colour coded by the lithostratigraphic assignment of Hudson (2010) and chemostratigraphic assignment made in this thesis.

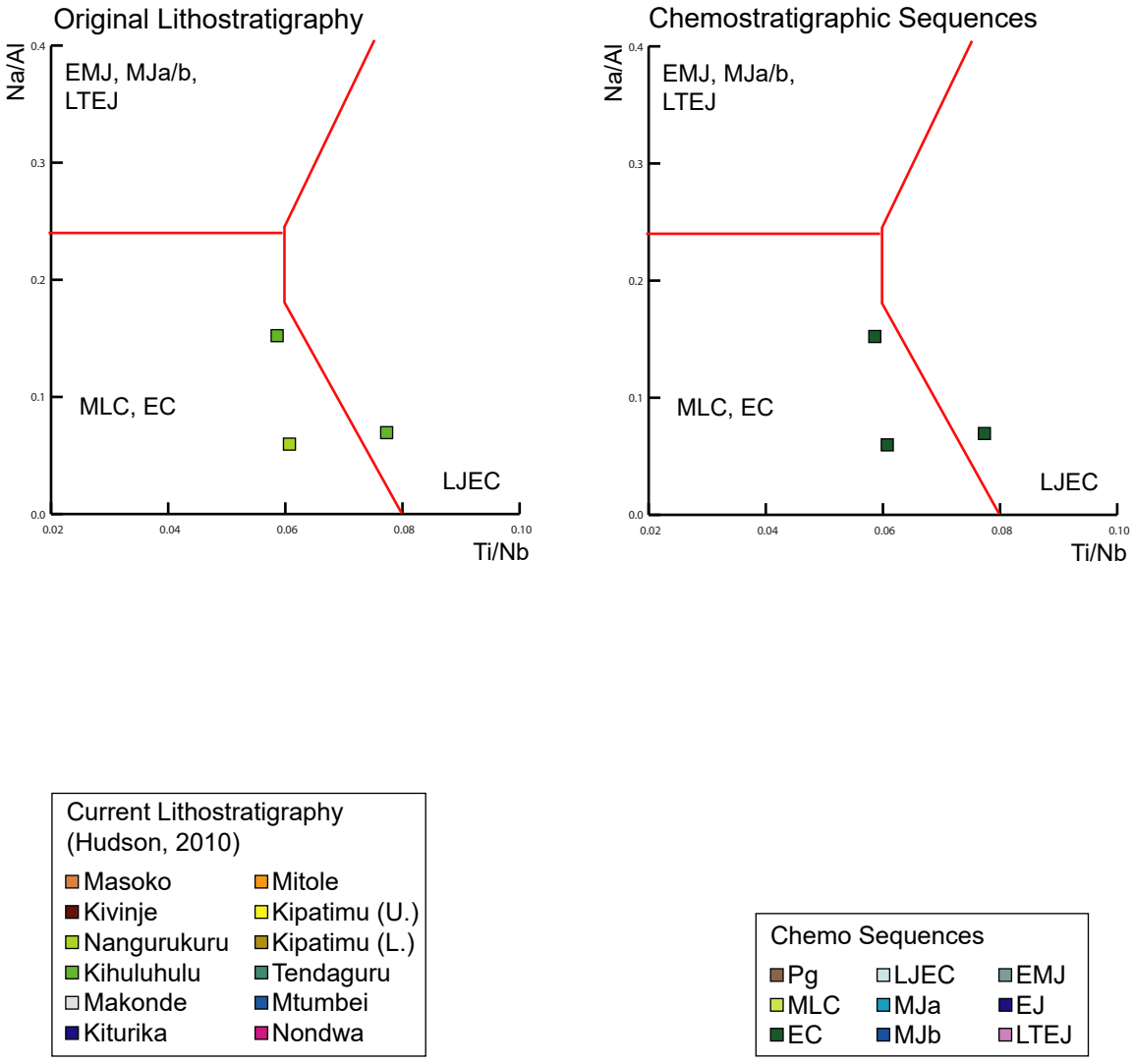

Figure A5.27. Claystone-based binary diagrams distinguishing the chemostratigraphic sequences encountered at outcrop along South Mandawa Transect-7: samples colour coded by the lithostratigraphic assignment of Hudson (2010).

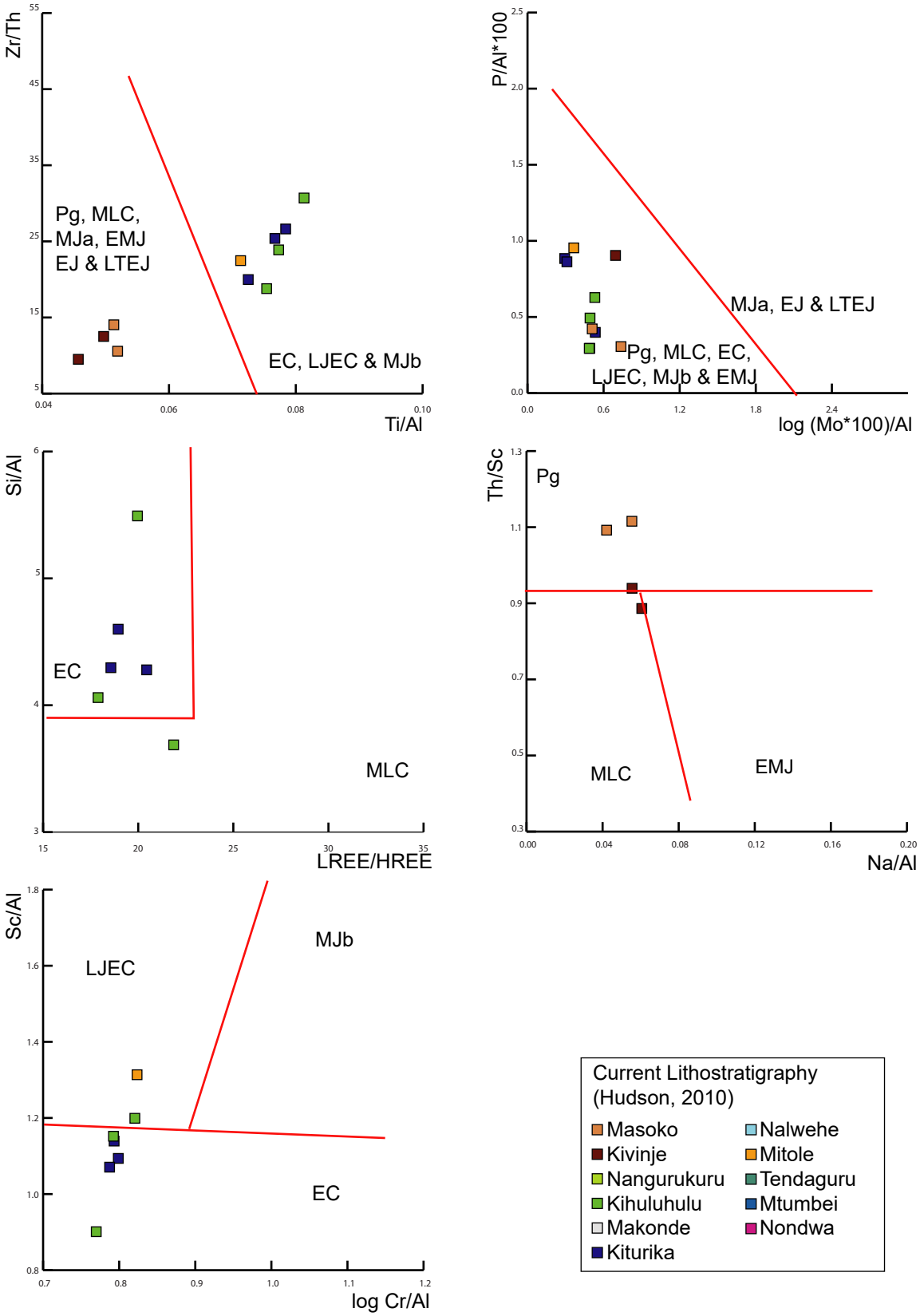

Figure A5.28. Claystone-based binary diagrams distinguishing the chemostratigraphic sequences encountered at outcrop along South Mandawa Transect-7: samples colour coded by the chemostratigraphic assignment made in this thesis.

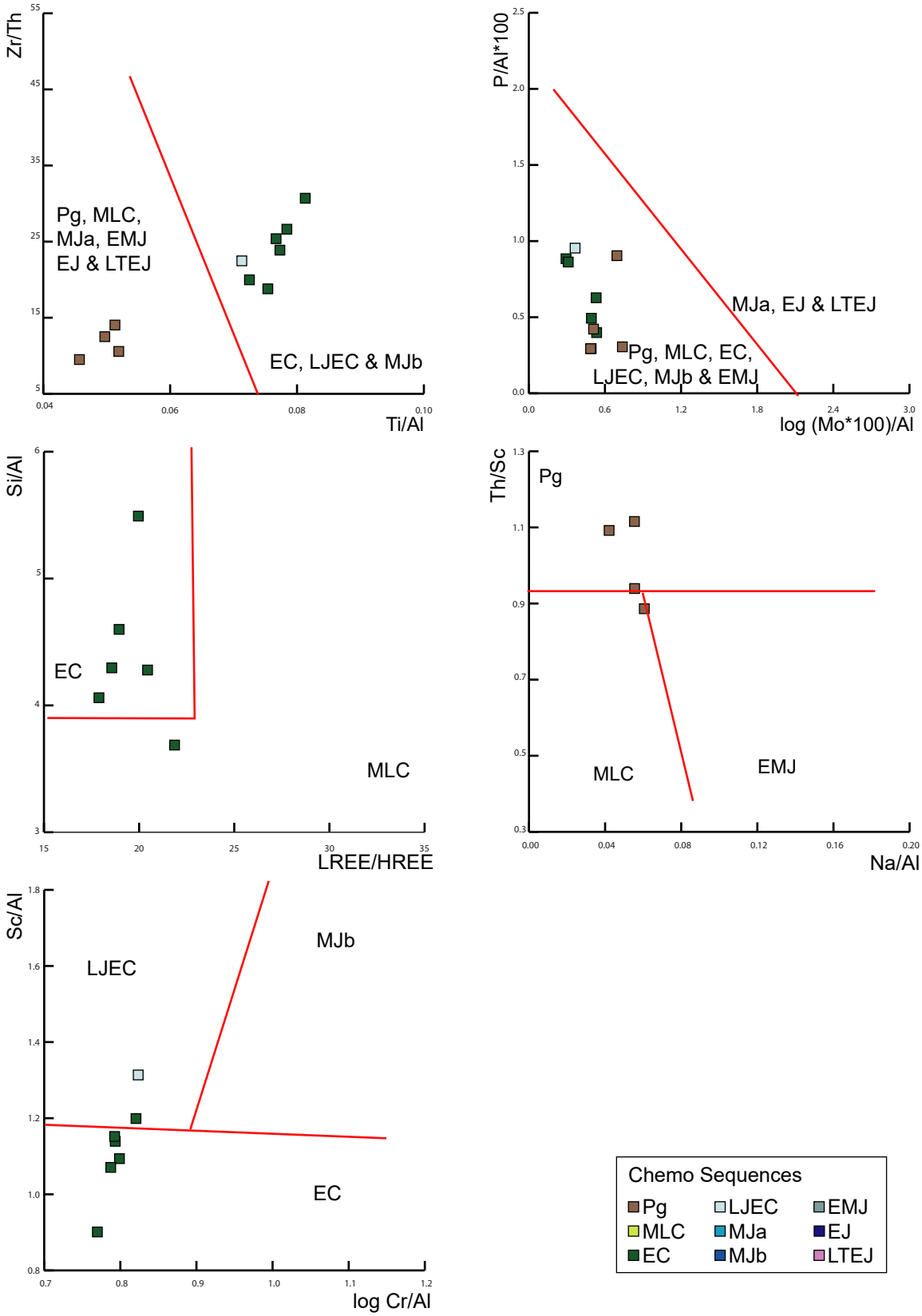

Figure A5.29. Sandstone-based binary diagram distinguishing the chemostratigraphic sequences encountered at outcrop along South Mandawa Transect-7: samples colour coded by the lithostratigraphic assignment of Hudson (2010) and chemostratigraphic assignment made in this thesis.

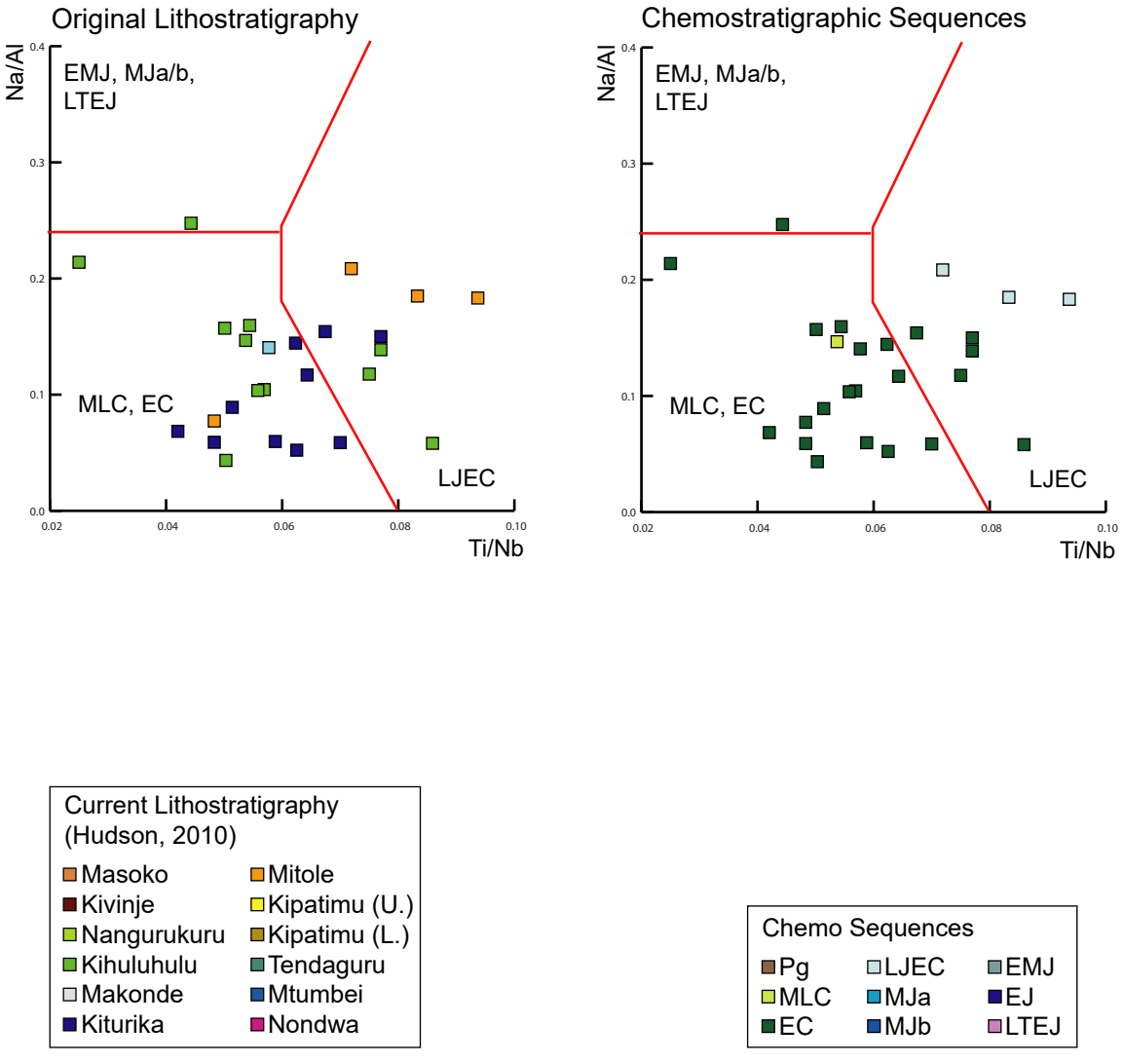

Figure A5.30. Claystone and sandstone-based binary diagrams distinguishing the chemostratigraphic sequences encountered at outcrop along South Mandawa Transect-8: samples colour coded by the lithostratigraphic assignment of Hudson (2010).

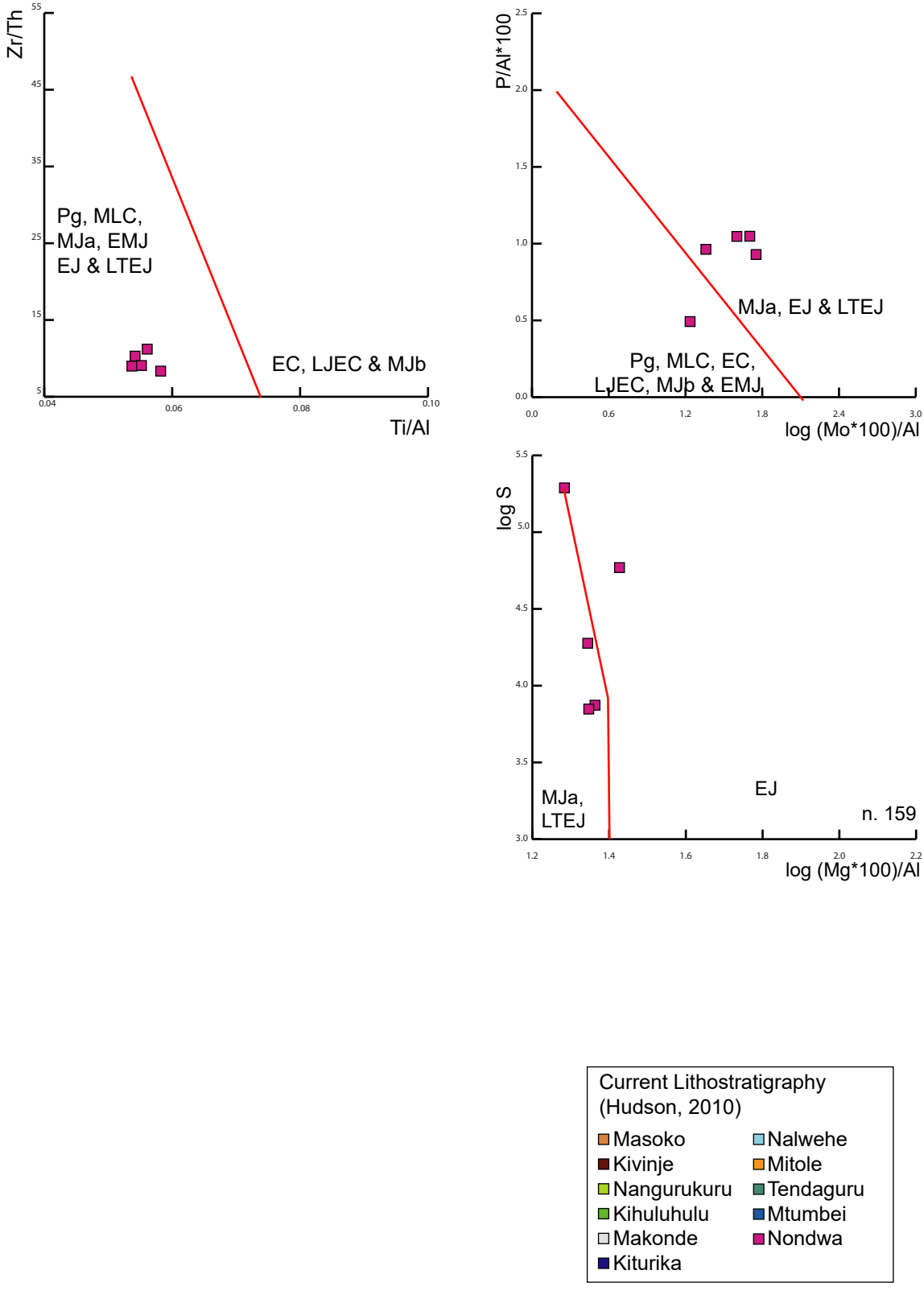

Figure A5.31. Claystone and sandstone-based binary diagrams distinguishing the chemostratigraphic sequences encountered at outcrop along South Mandawa Transect-8: samples colour coded by the chemostratigraphic assignment made in this thesis.

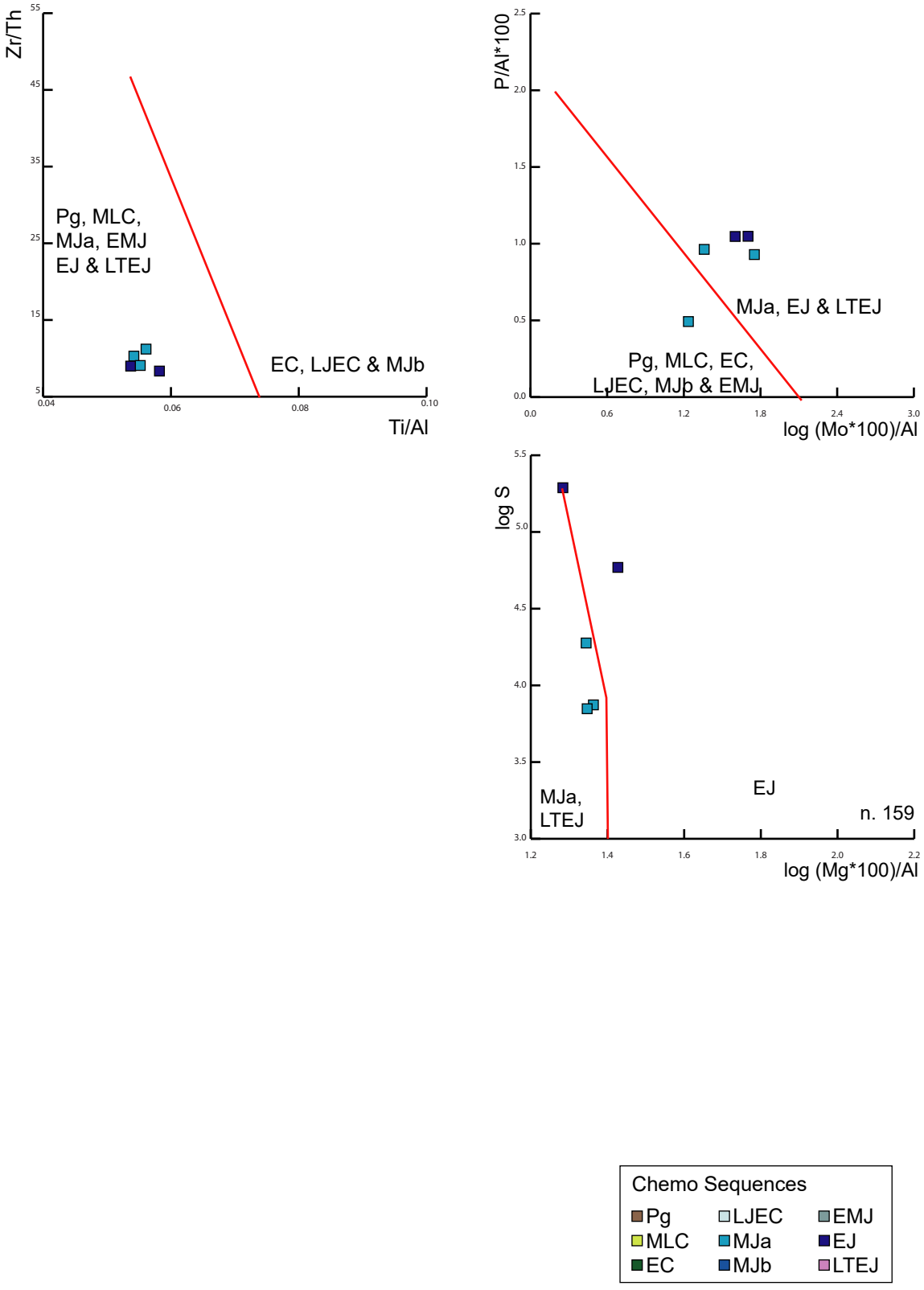

Figure A5.32. Claystone and sandstone-based binary diagrams distinguishing the chemostratigraphic sequences encountered at outcrop along South Mandawa Transect-9: samples colour coded by the lithostratigraphic assignment of Hudson (2010).

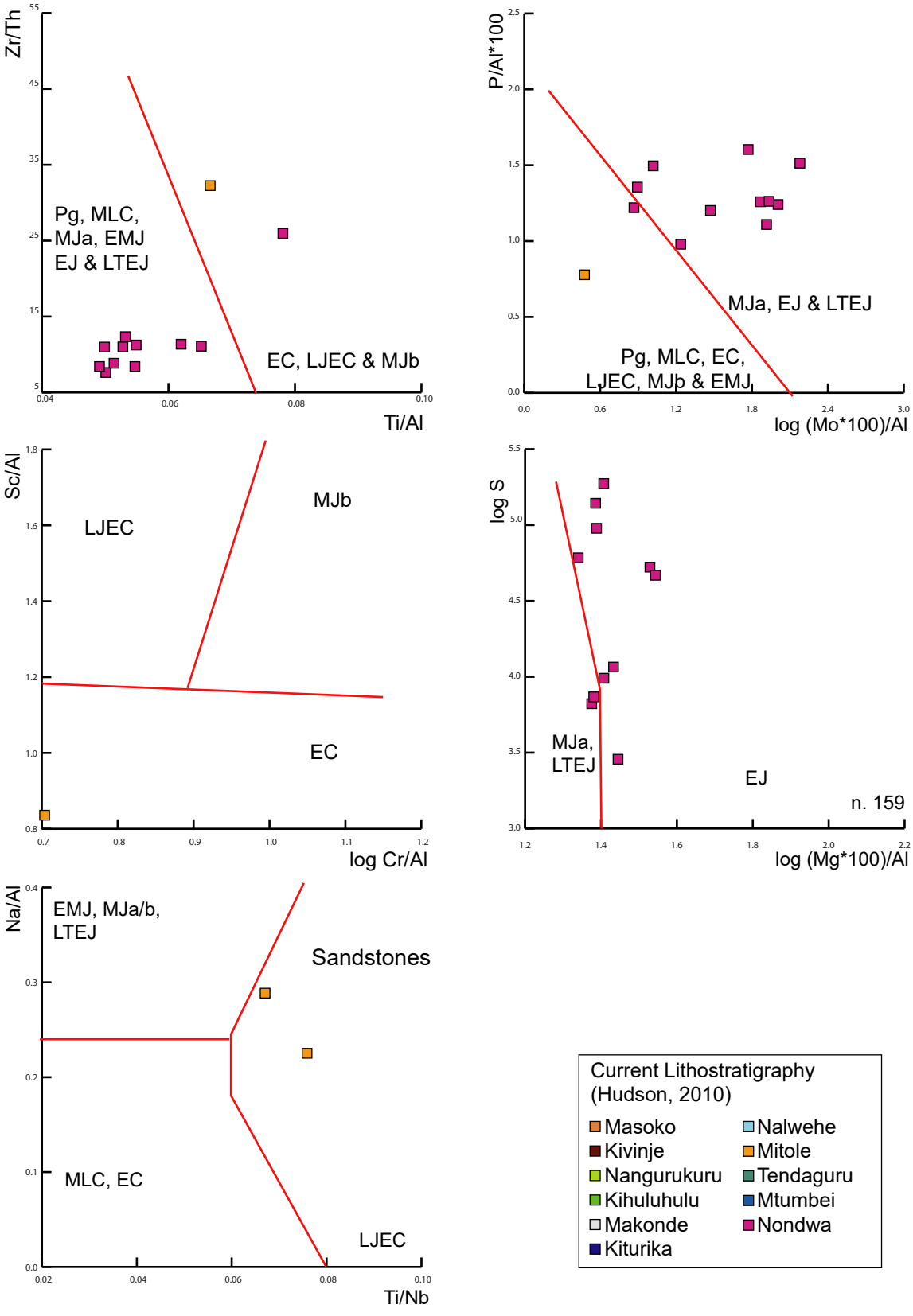

Figure A5.33. Claystone and sandstone-based binary diagrams distinguishing the chemostratigraphic sequences encountered at outcrop along South Mandawa Transect-9: samples colour coded by the chemostratigraphic assignment made in this thesis.

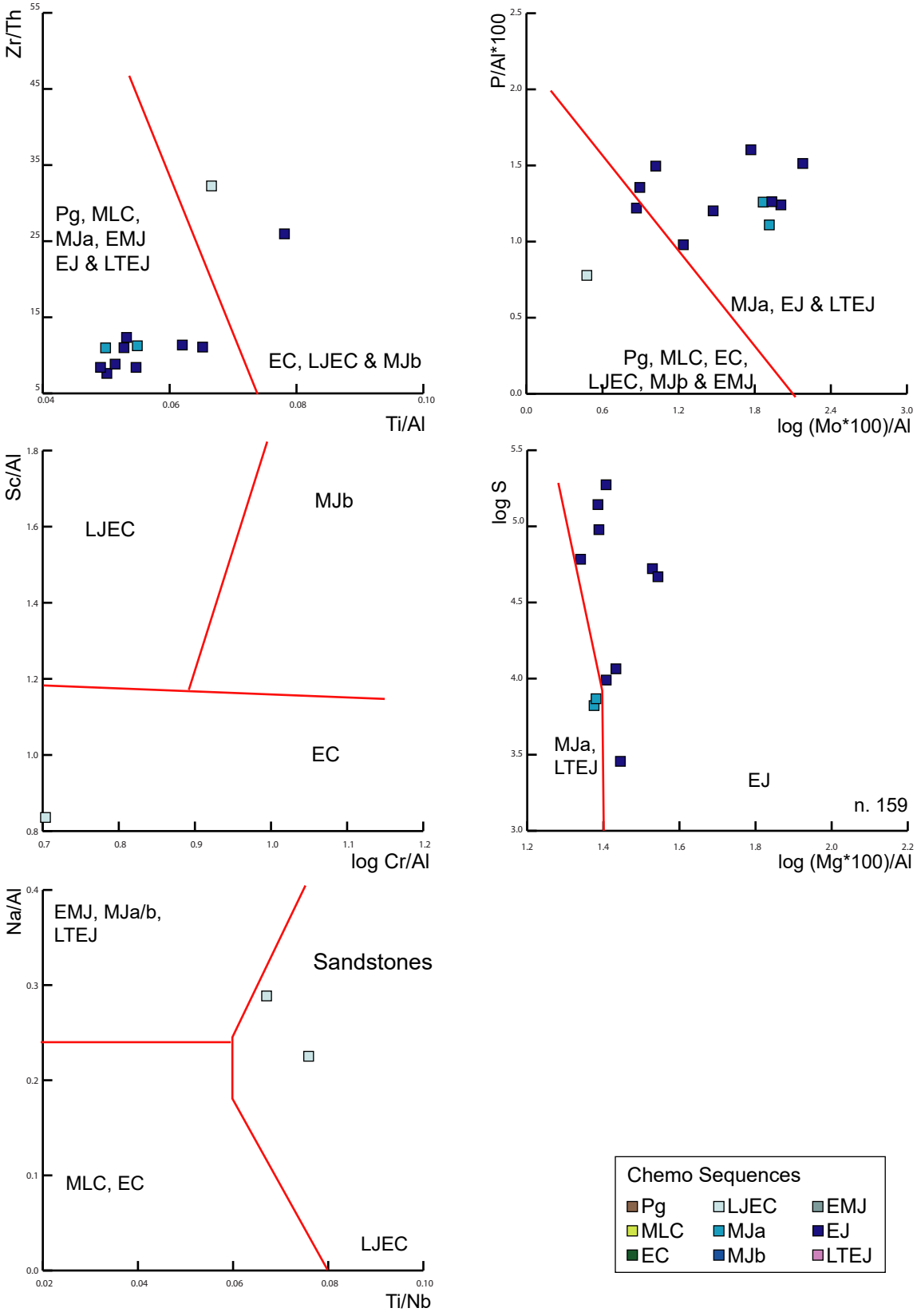

Figure A5.34. Claystone and sandstone-based binary diagrams distinguishing the chemostratigraphic sequences encountered at outcrop along South Mandawa Transect-10: samples colour coded by the lithostratigraphic assignment of Hudson (2010).

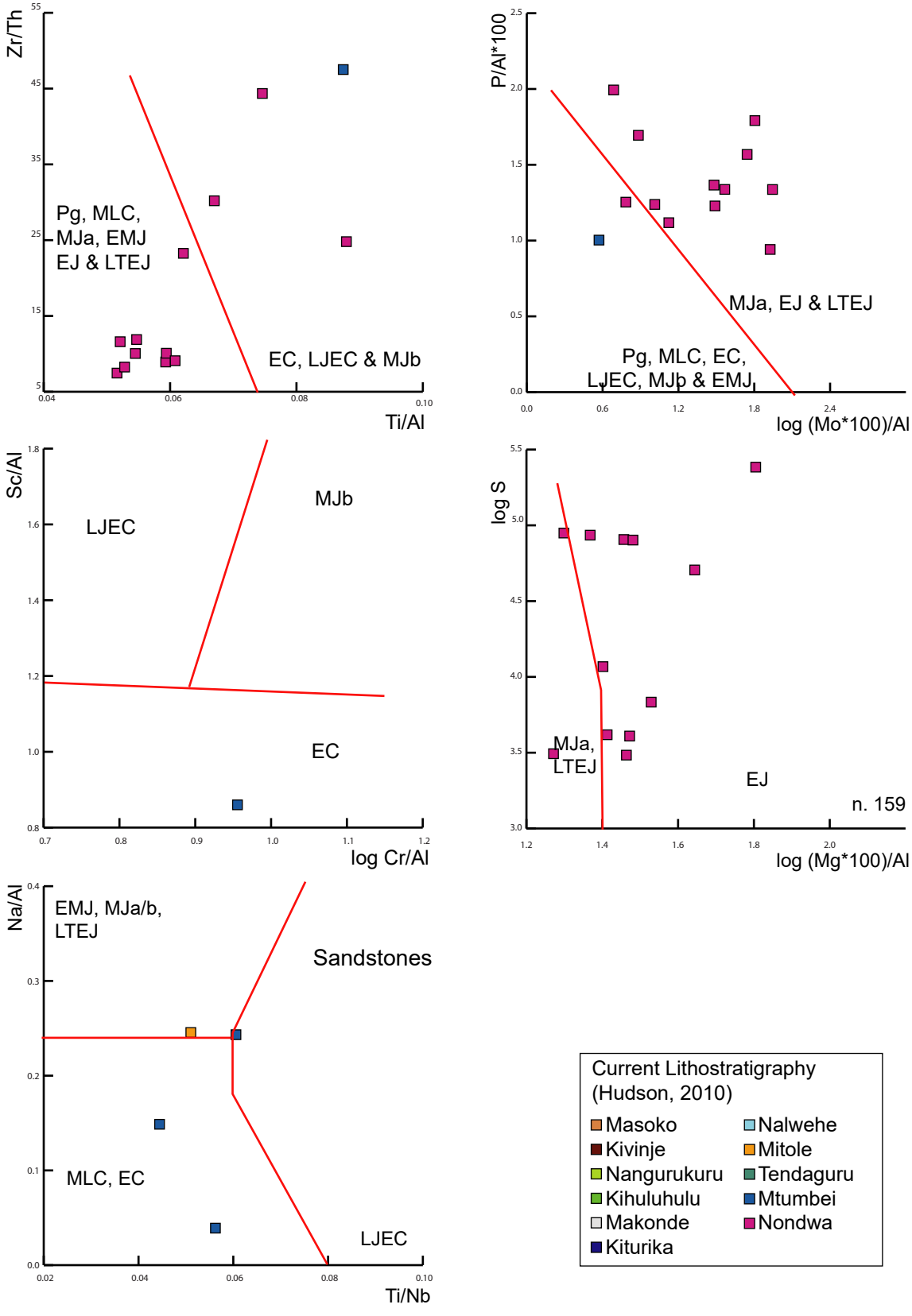

Figure A5.35. Claystone and sandstone-based binary diagrams distinguishing the chemostratigraphic sequences encountered at outcrop along South Mandawa Transect-10: samples colour coded by the chemostratigraphic assignment made in this thesis.

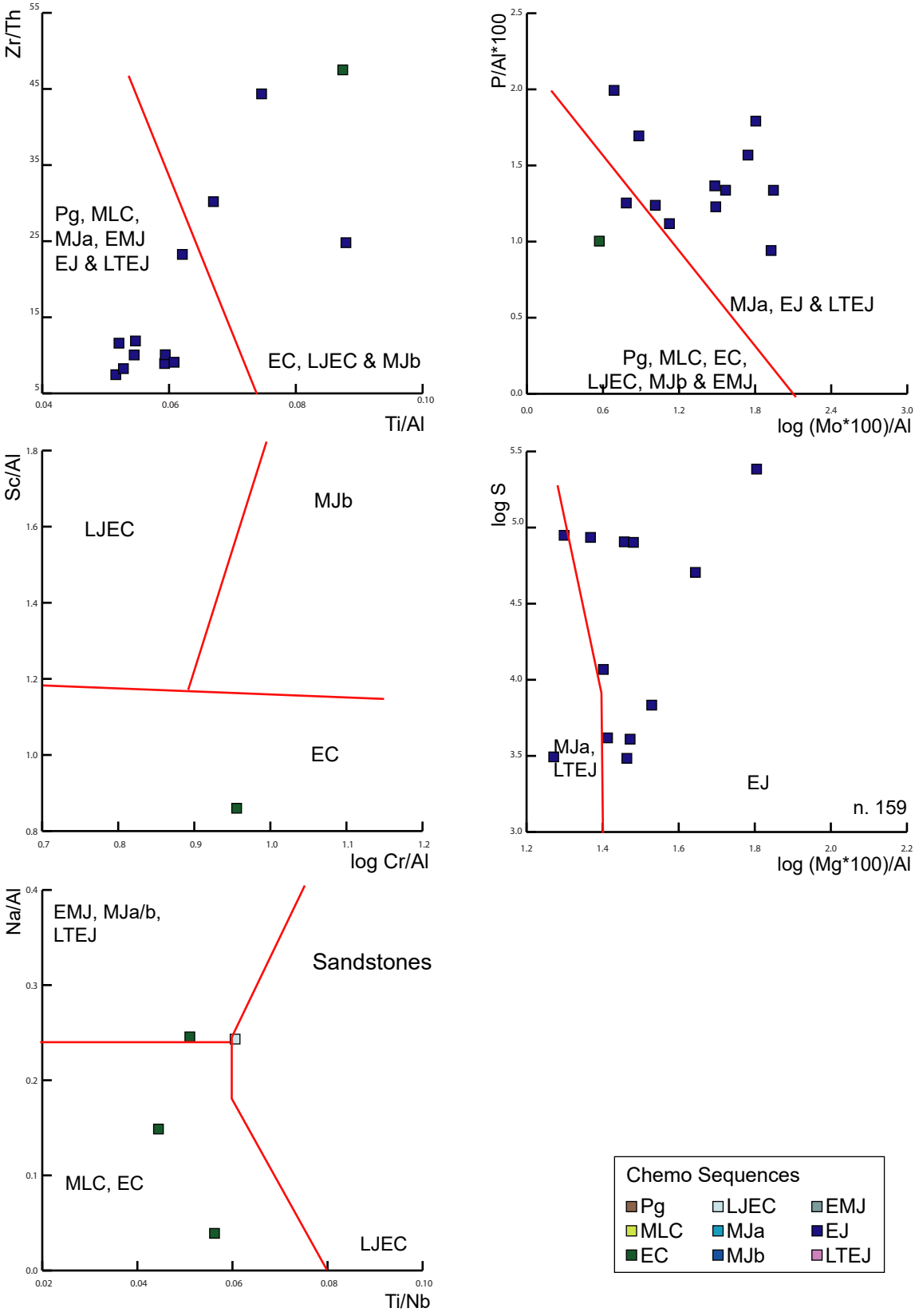

Figure A5.36. Claystone-based binary diagrams distinguishing the chemostratigraphic sequences encountered at outcrop along South Mandawa Transect-11: samples colour coded by the lithostratigraphic assignment of Hudson (2010).

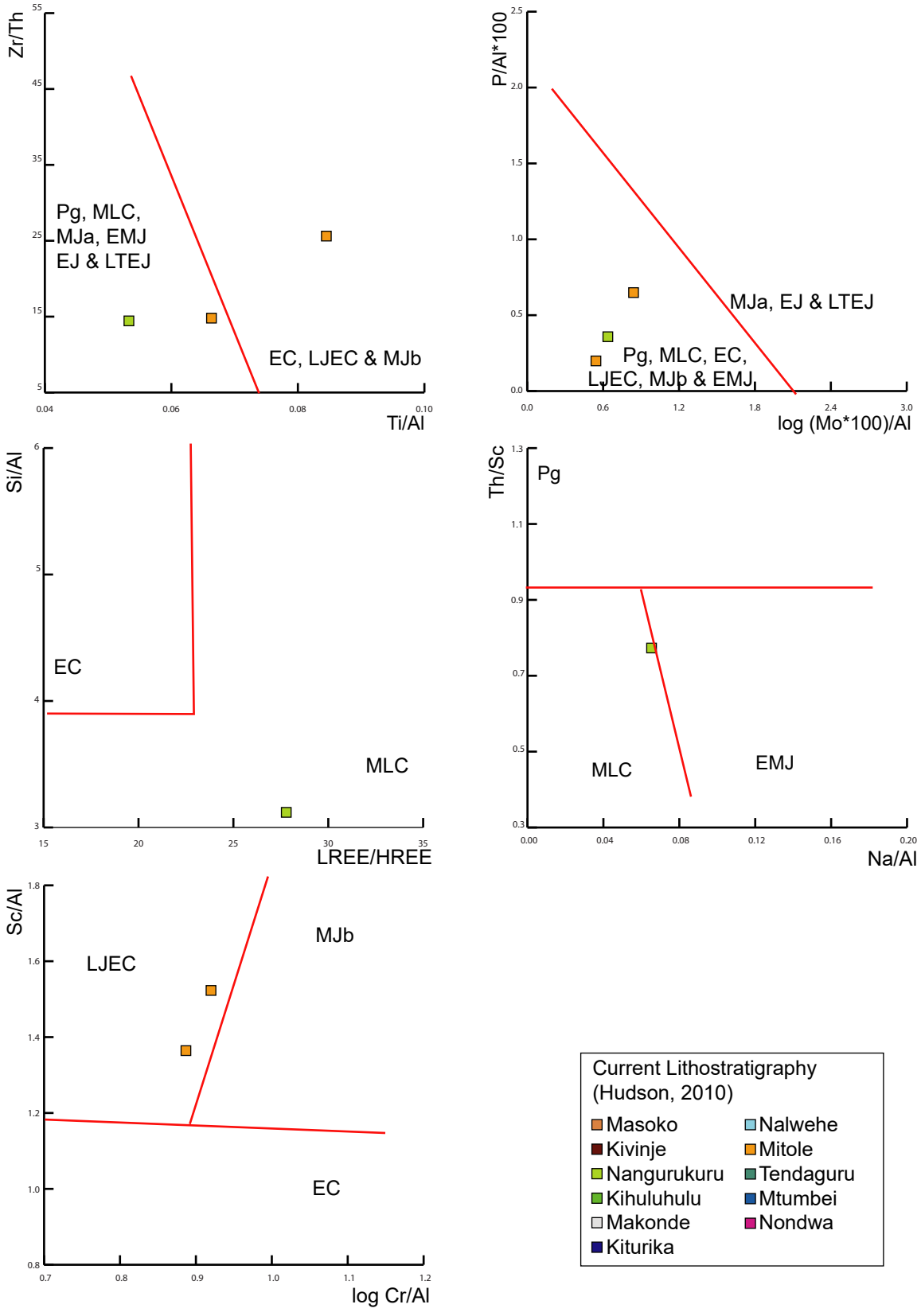

Figure A5.37. Claystone-based binary diagrams distinguishing the chemostratigraphic sequences encountered at outcrop along South Mandawa Transect-11: samples colour coded by the chemostratigraphic assignment made in this thesis.

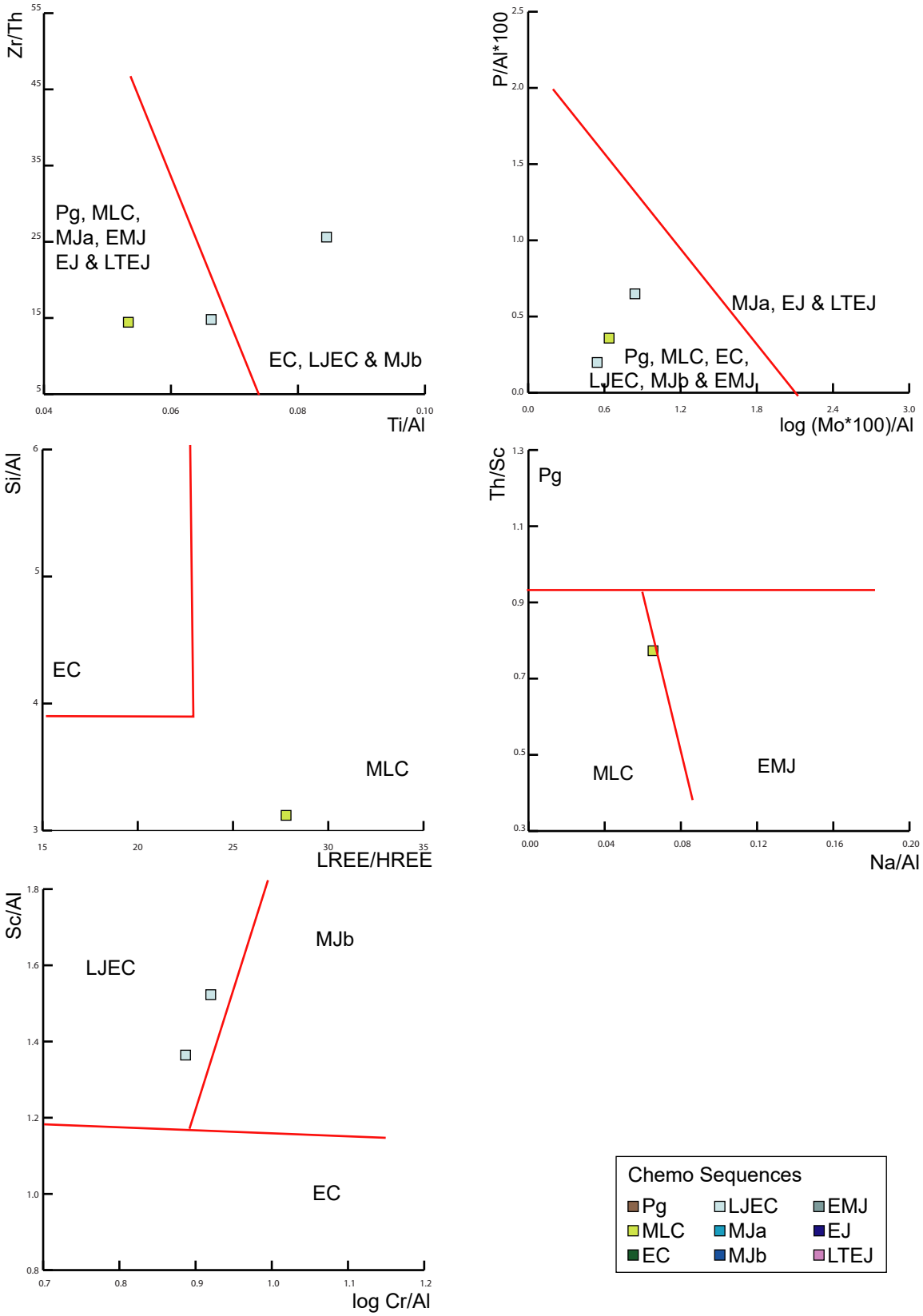

Figure A5.38. Sandstone-based binary diagram distinguishing the chemostratigraphic sequences encountered at outcrop along South Mandawa Transect-11: samples colour coded by the lithostratigraphic assignment of Hudson (2010) and chemostratigraphic assignment made in this thesis.

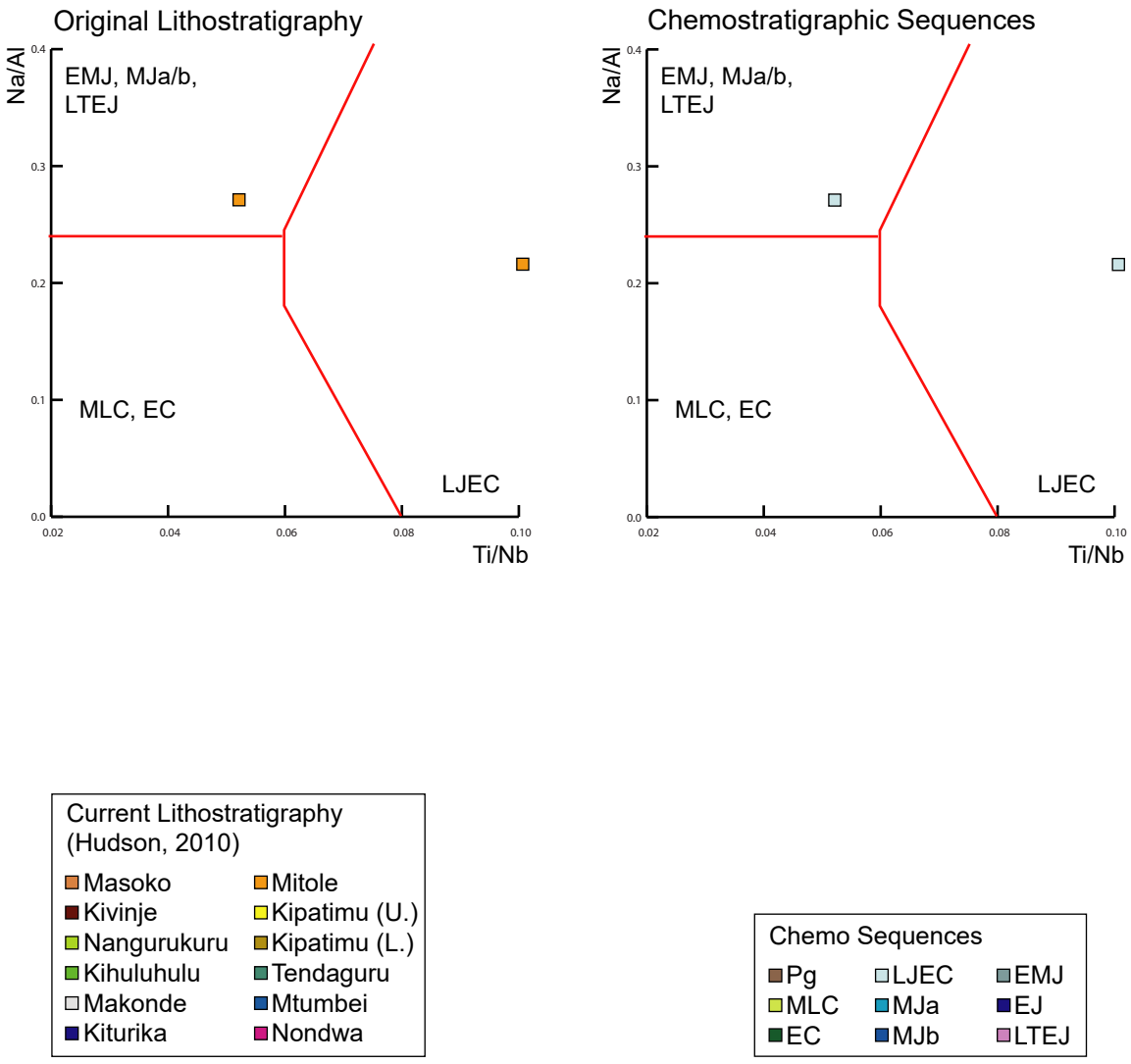

Figure A5.39. Claystone and sandstone-based binary diagrams distinguishing the chemostratigraphic sequences encountered at outcrop along South Mandawa Transect-12: samples colour coded by the lithostratigraphic assignment of Hudson (2010).

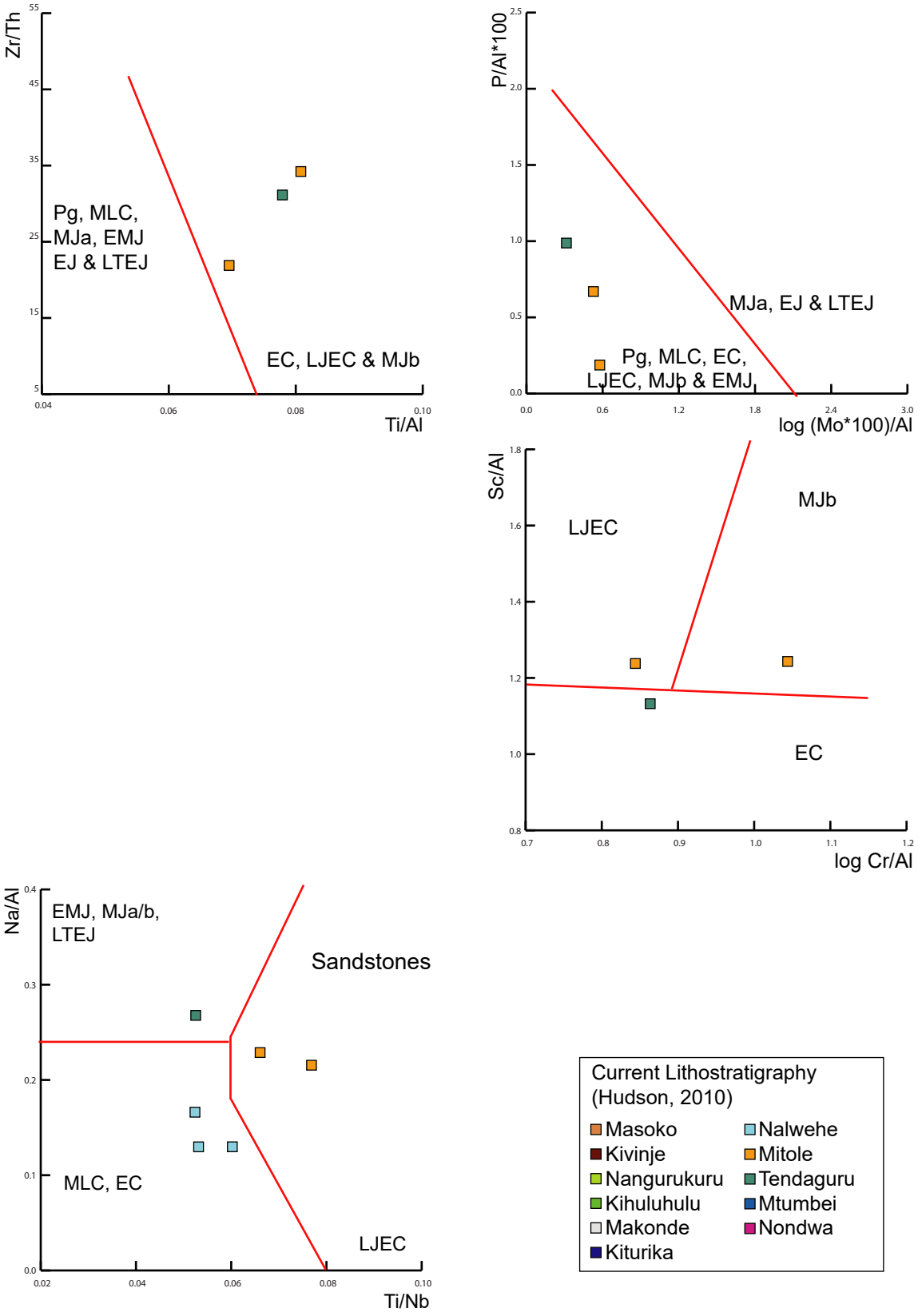

Figure A5.40. Claystone and sandstone-based binary diagrams distinguishing the chemostratigraphic sequences encountered at outcrop along South Mandawa Transect-12: samples colour coded by the chemostratigraphic assignment made in this thesis.

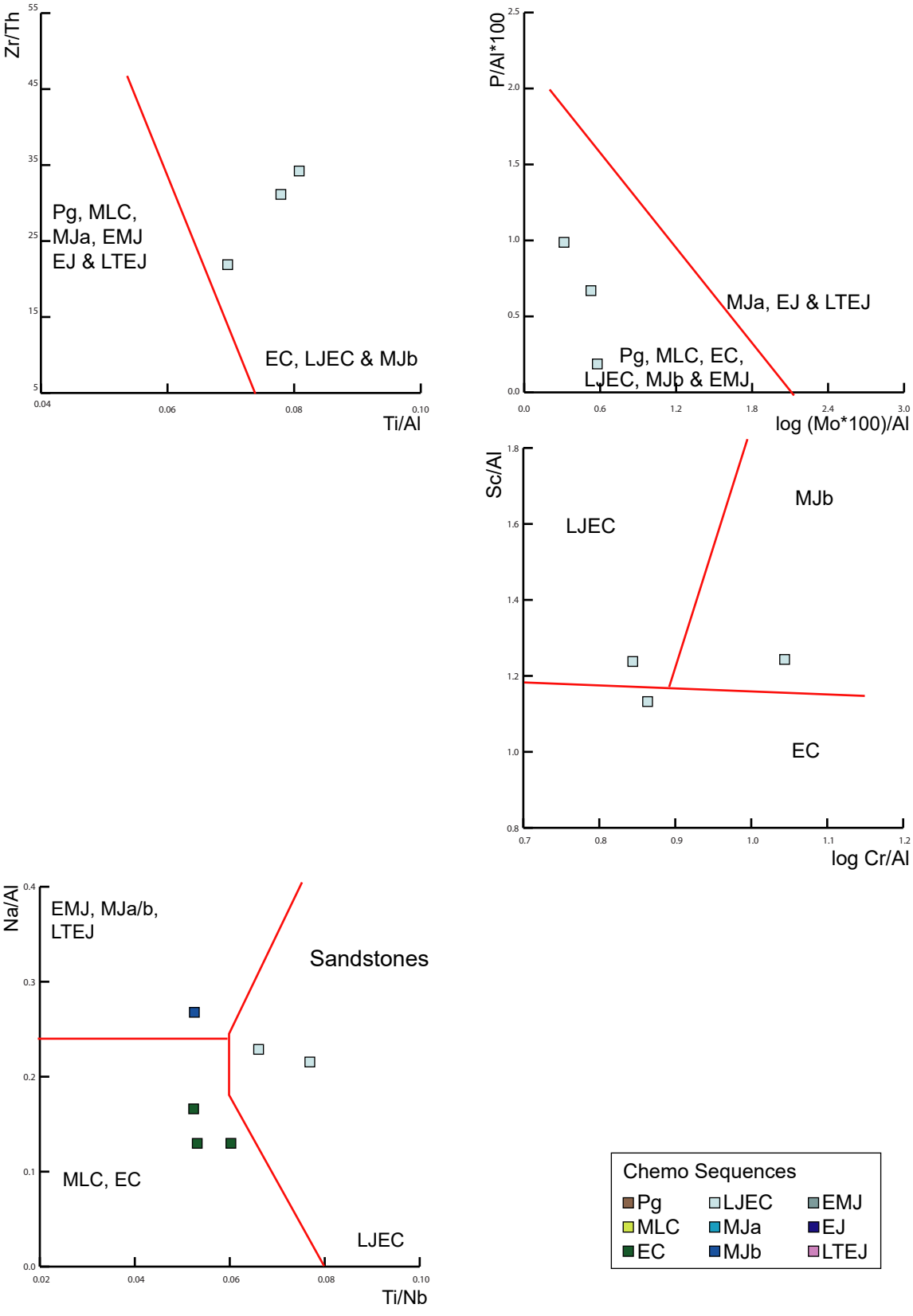

Figure A5.41. Claystone-based binary diagrams distinguishing the chemostratigraphic packages encountered at outcrop along North Mandawa Transect-1: samples colour coded by the chemostratigraphic assignment made in this thesis.

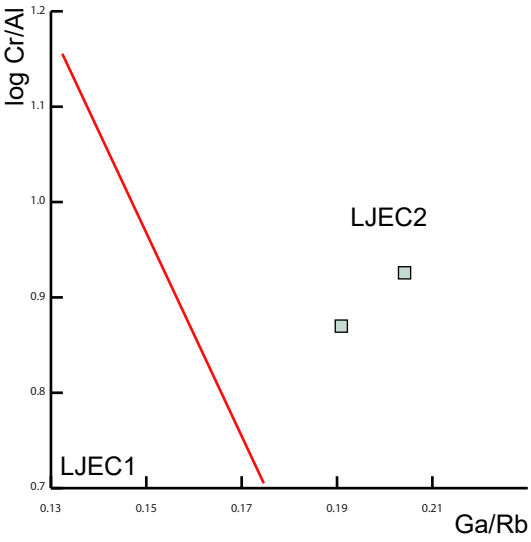

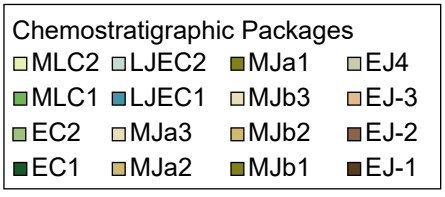

Figure A5.42. Claystone-based binary diagrams distinguishing the chemostratigraphic packages encountered at outcrop along North Mandawa Transect-2: samples colour coded by the chemostratigraphic assignment made in this thesis.

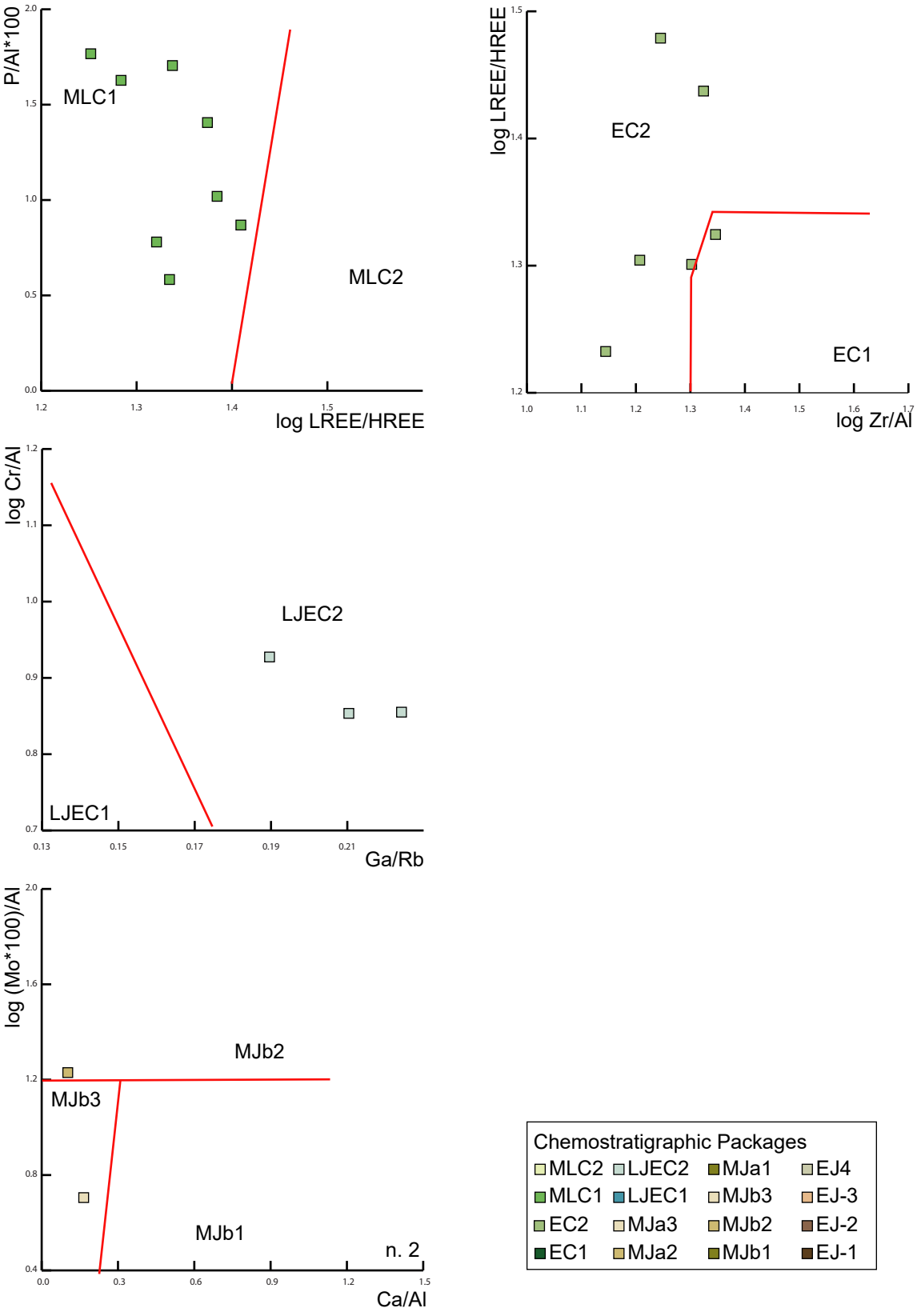

Figure A5.43. Claystone-based binary diagrams distinguishing the chemostratigraphic packages encountered at outcrop along North Mandawa Transect-3: samples colour coded by the chemostratigraphic assignment made in this thesis.

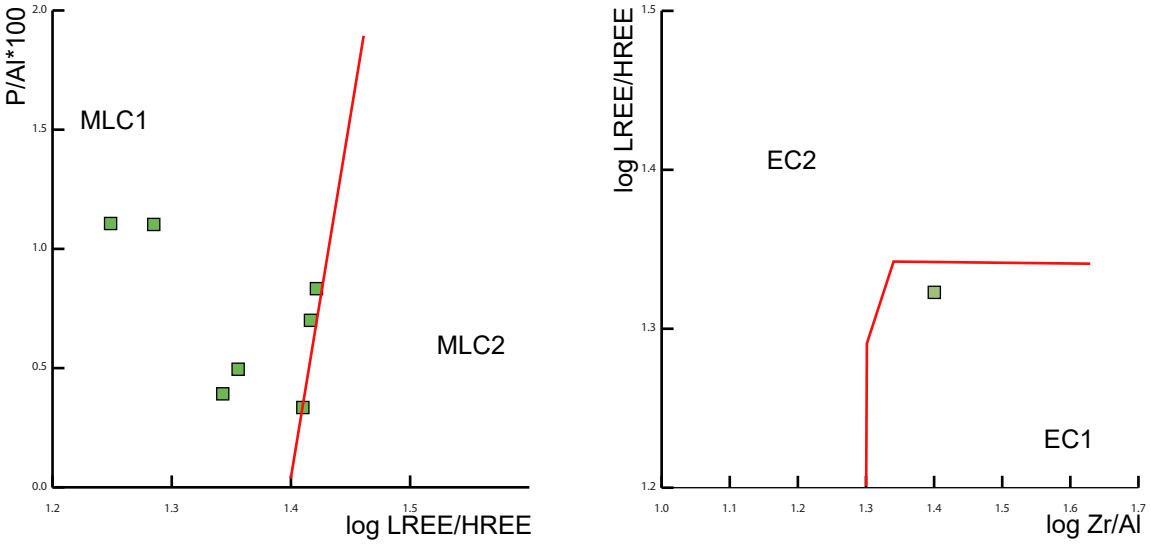

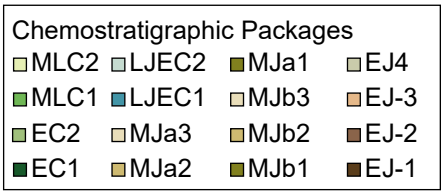

Figure A5.44. Claystone-based binary diagrams distinguishing the chemostratigraphic packages encountered at outcrop along South Mandawa Transect-1: samples colour coded by the chemostratigraphic assignment made in this thesis.

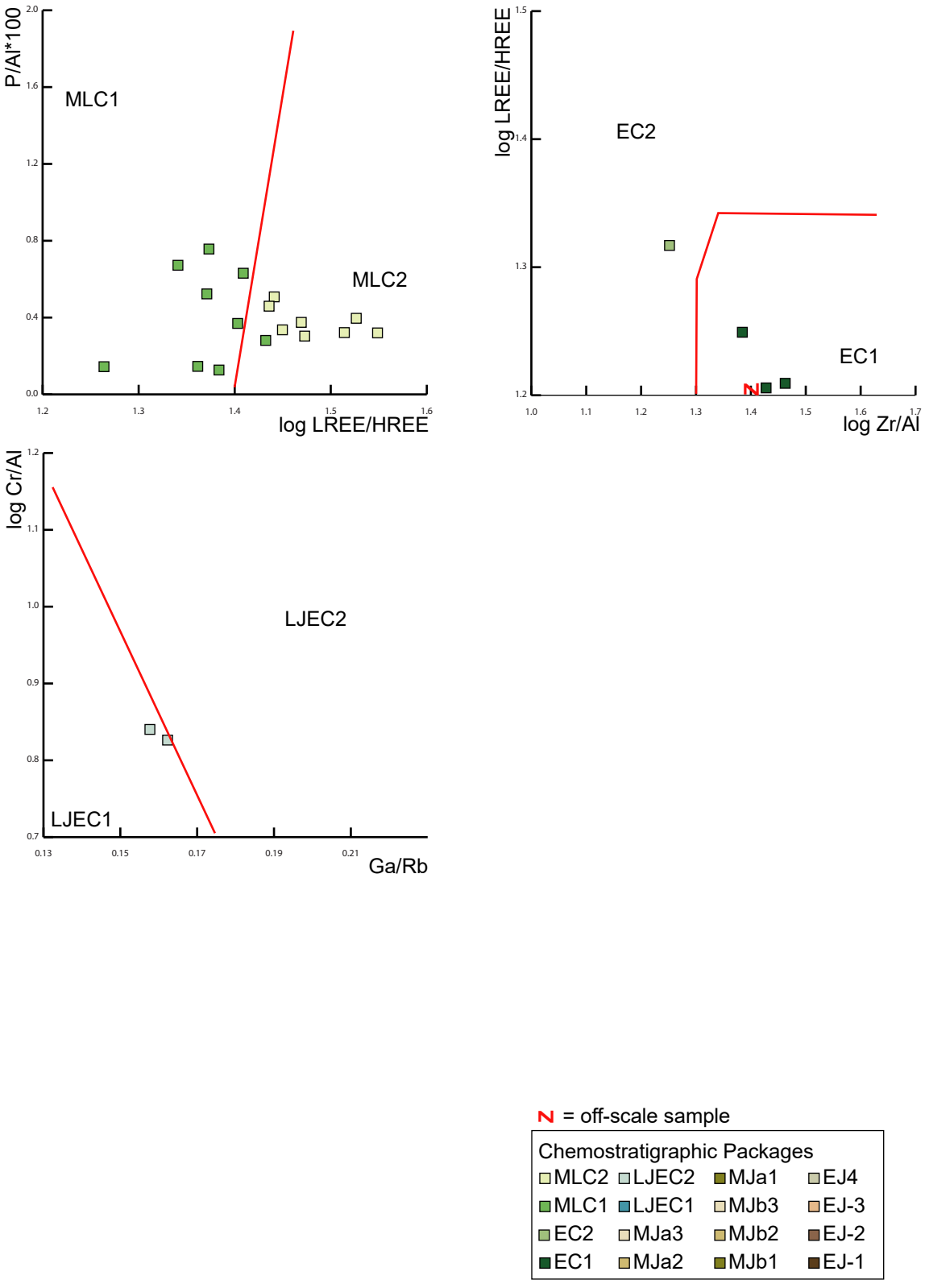

Figure A5.45. Claystone-based binary diagrams distinguishing the chemostratigraphic packages encountered at outcrop along South Mandawa Transect-2: samples colour coded by the chemostratigraphic assignment made in this thesis.

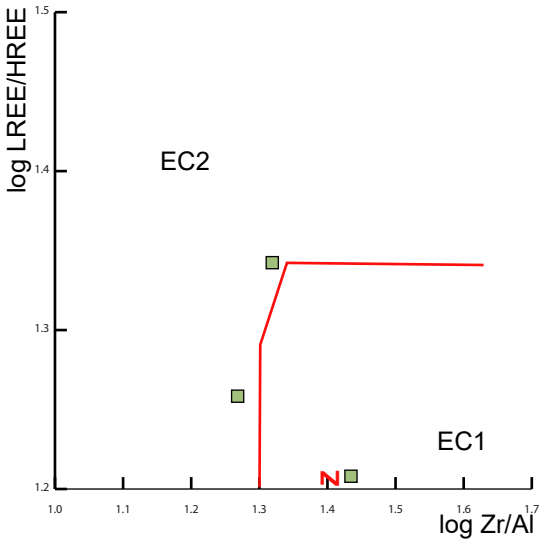

N = off-scale sample

Chemostratigraphic Packages

MLC2	LJEC2	MJa1	EJ4
MLC1	LJEC1	MJb3	EJ-3
EC2	MJa3	MJb2	EJ-2
EC1	MJa2	MJb1	EJ-1

Figure A5.46. Claystone-based binary diagrams distinguishing the chemostratigraphic packages encountered at outcrop along South Mandawa Transect-3: samples colour coded by the chemostratigraphic assignment made in this thesis.

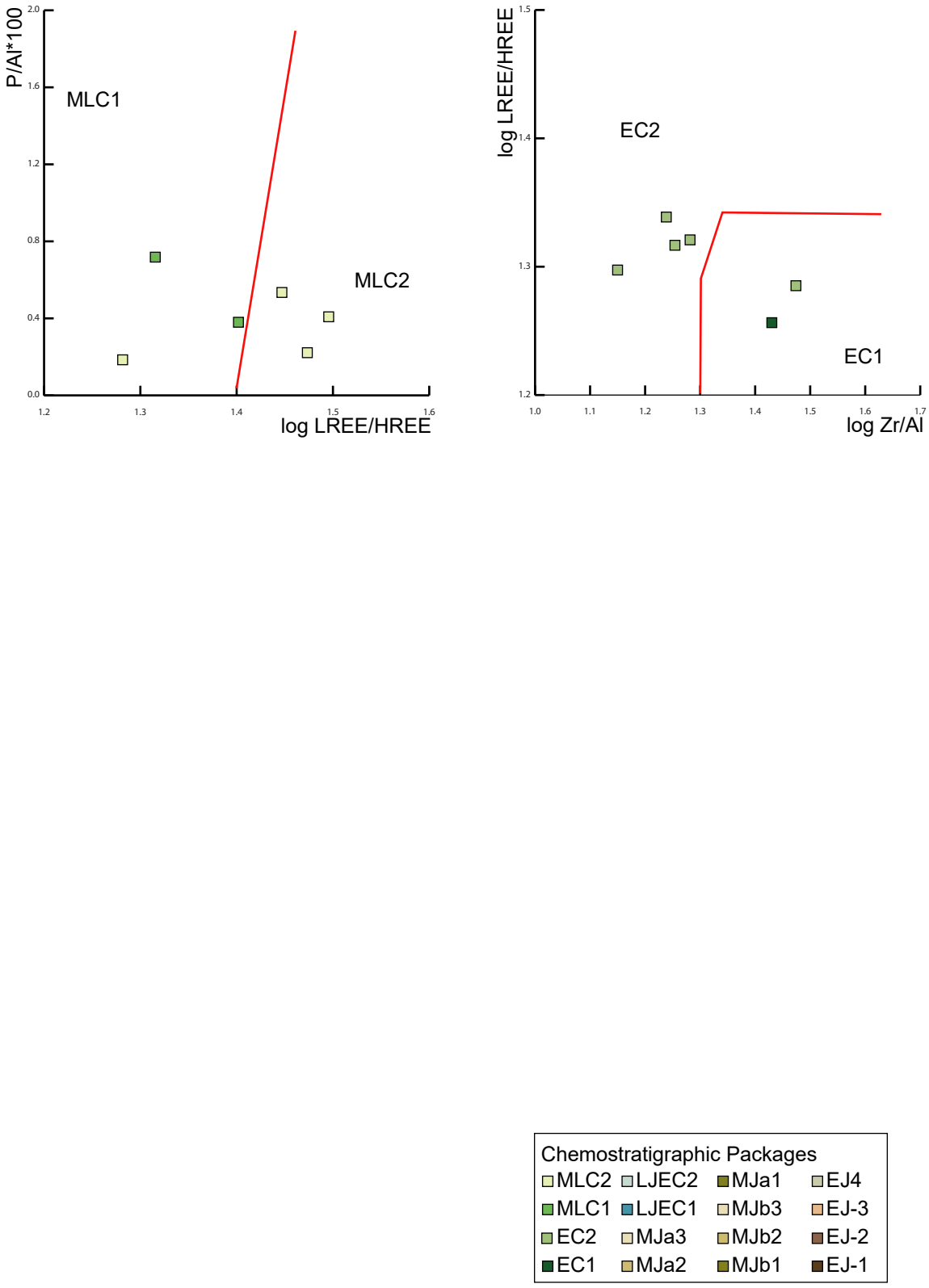

Figure A5.47. Claystone-based binary diagrams distinguishing the chemostratigraphic packages encountered at outcrop along South Mandawa Transect-4: samples colour coded by the chemostratigraphic assignment made in this thesis.

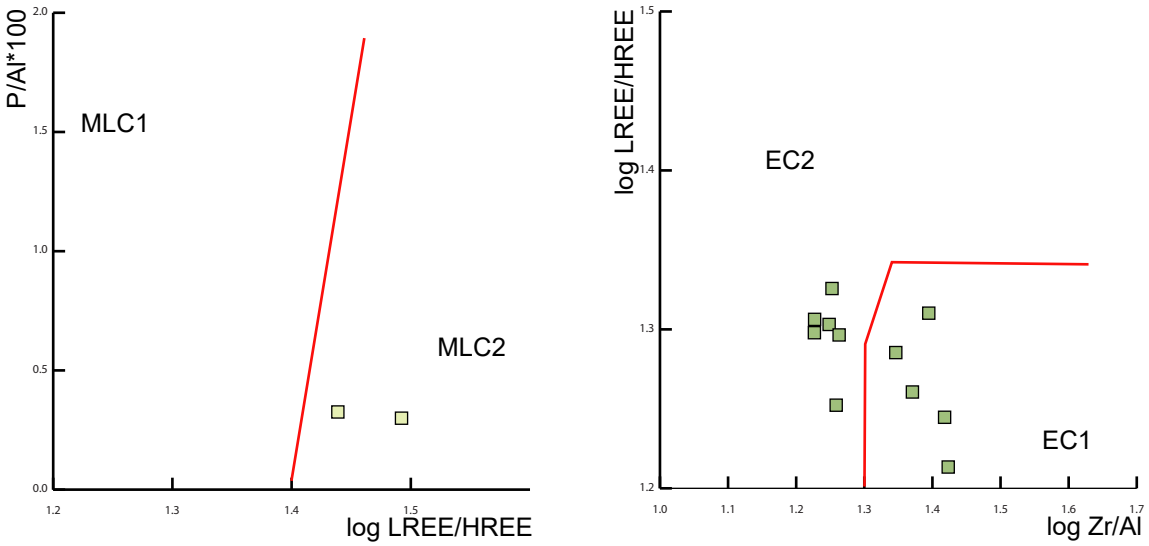

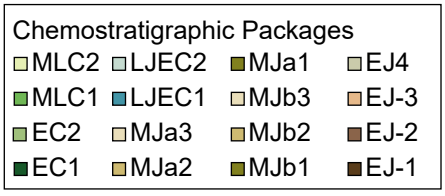

Figure A5.48. Claystone-based binary diagrams distinguishing the chemostratigraphic packages encountered at outcrop along South Mandawa Transect-5: samples colour coded by the chemostratigraphic assignment made in this thesis.

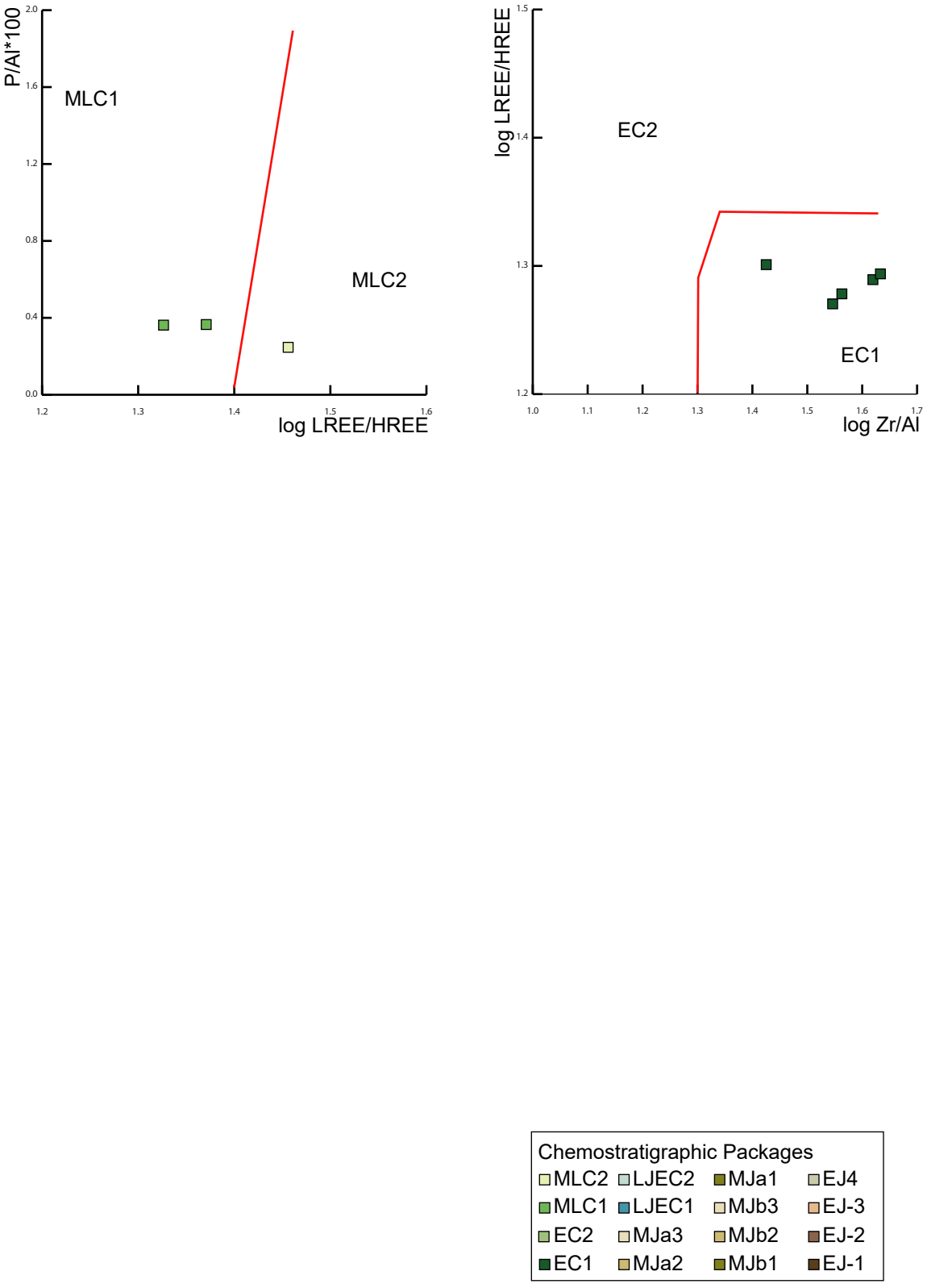

Figure A5.49. Claystone-based binary diagrams distinguishing the chemostratigraphic packages encountered at outcrop along South Mandawa Transect-6: samples colour coded by the chemostratigraphic assignment made in this thesis.

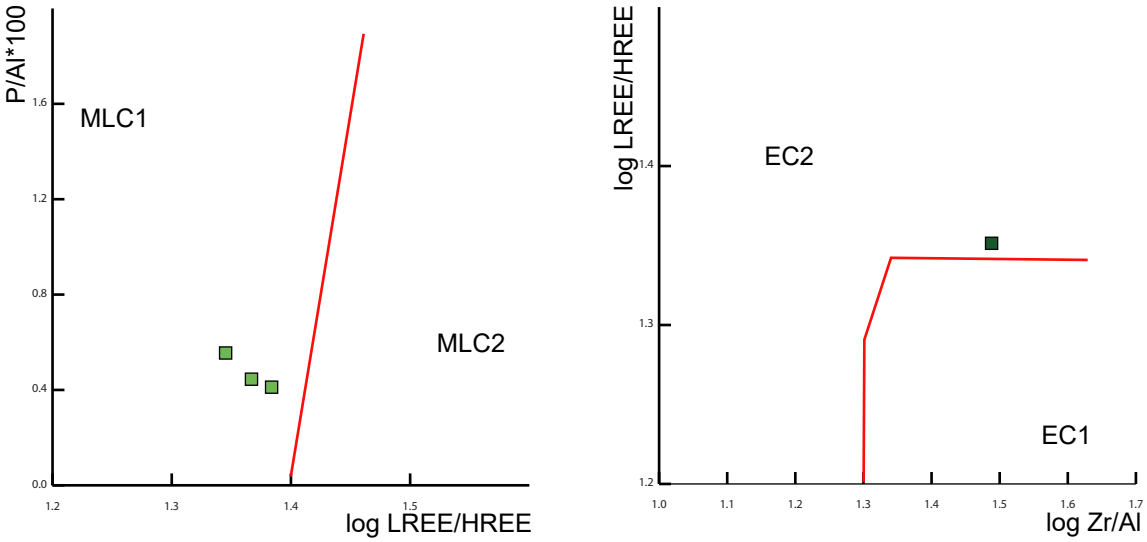

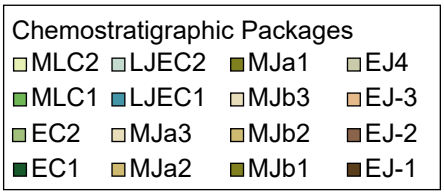

Figure A5.50. Claystone-based binary diagrams distinguishing the chemostratigraphic packages encountered at outcrop along South Mandawa Transect-7: samples colour coded by the chemostratigraphic assignment made in this thesis.

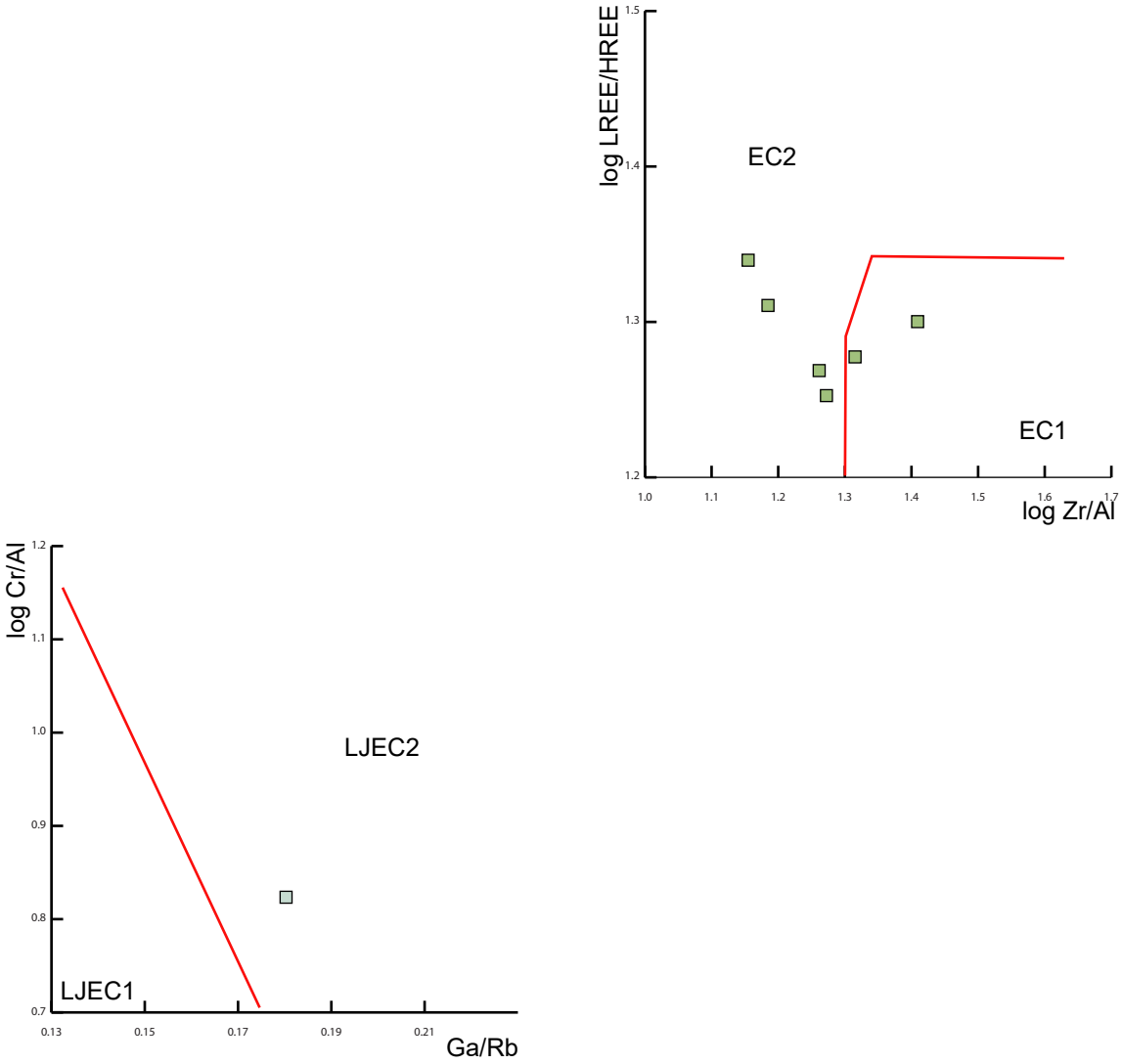

Figure A5.51. Claystone-based binary diagrams distinguishing the chemostratigraphic packages encountered at outcrop along South Mandawa Transect-8: samples colour coded by the chemostratigraphic assignment made in this thesis.

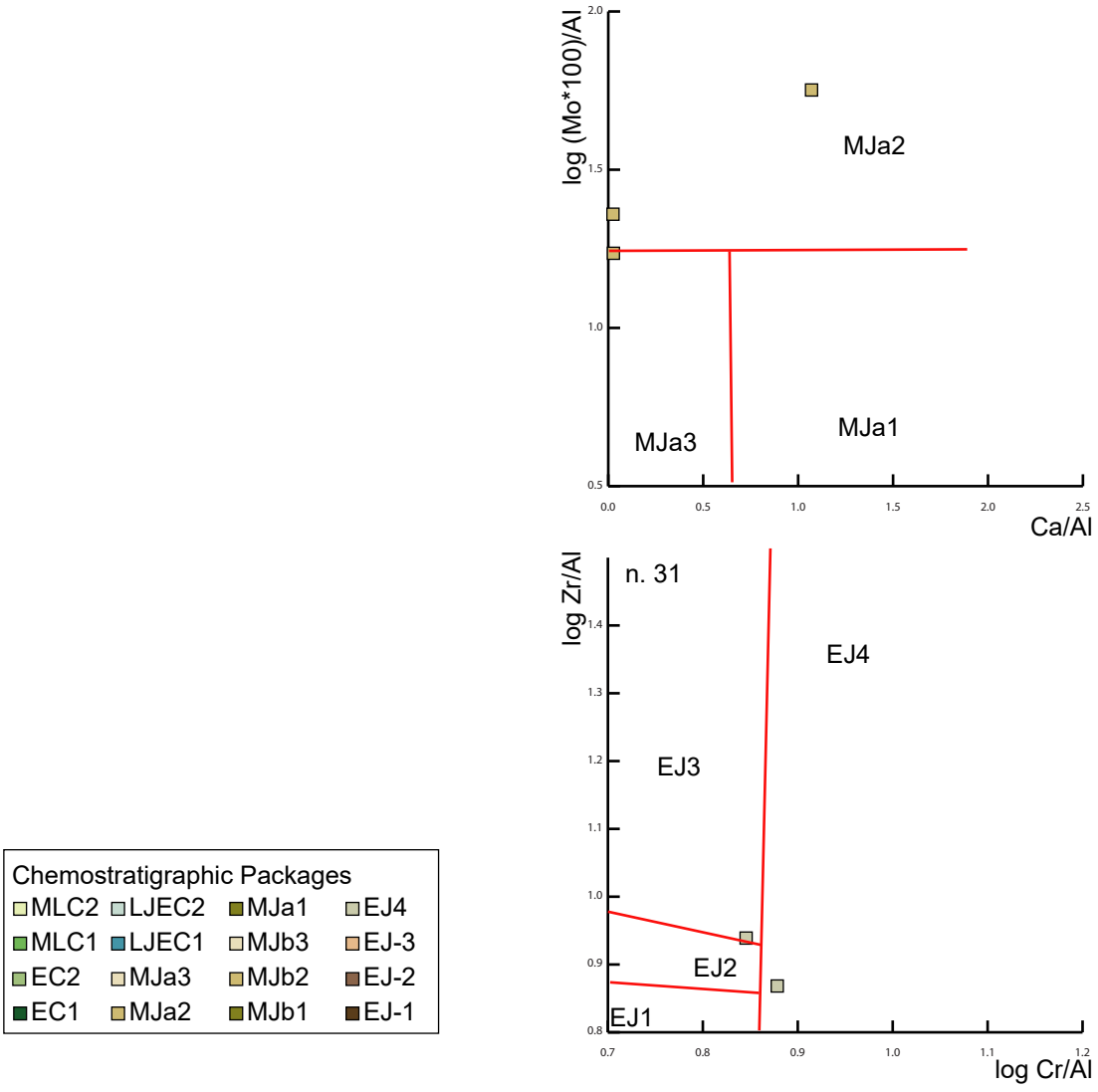

Figure A5.52. Claystone-based binary diagrams distinguishing the chemostratigraphic packages encountered at outcrop along South Mandawa Transect-9: samples colour coded by the chemostratigraphic assignment made in this thesis.

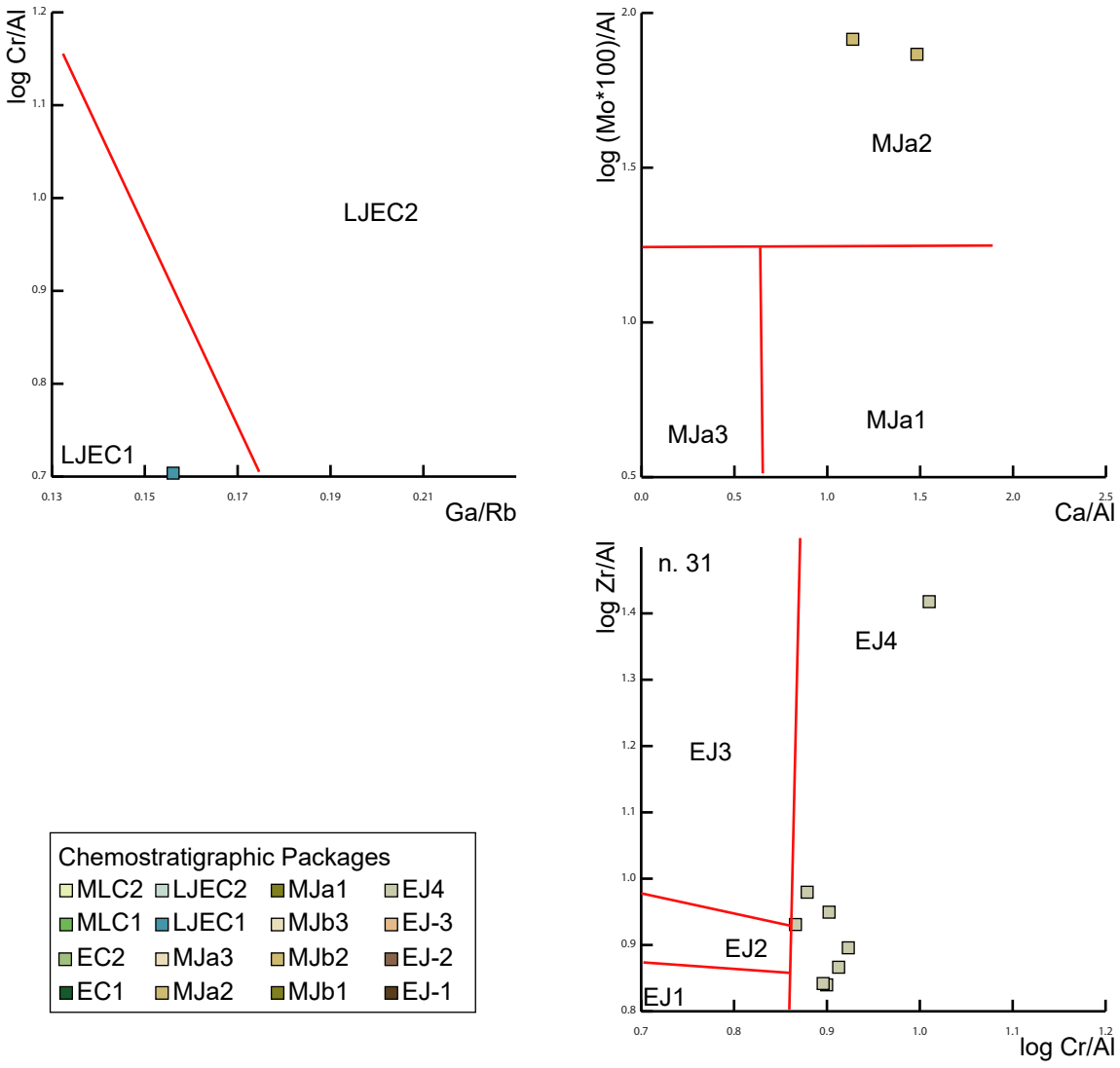

Figure A5.53. Claystone-based binary diagrams distinguishing the chemostratigraphic packages encountered at outcrop along South Mandawa Transect-10: samples colour coded by the chemostratigraphic assignment made in this thesis.

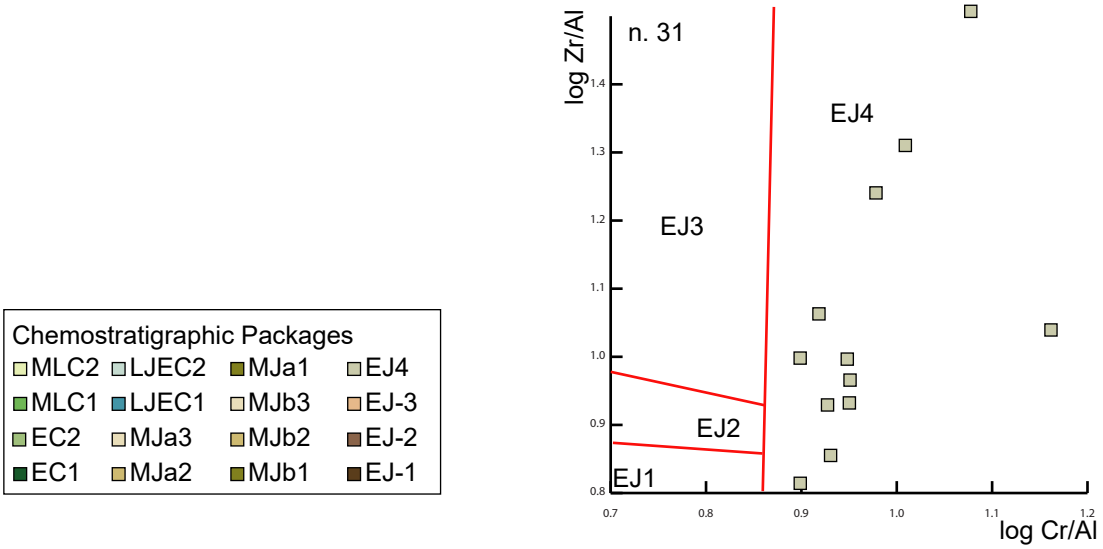

Figure A5.54. Claystone-based binary diagrams distinguishing the chemostratigraphic packages encountered at outcrop along South Mandawa Transect-11: samples colour coded by the chemostratigraphic assignment made in this thesis.

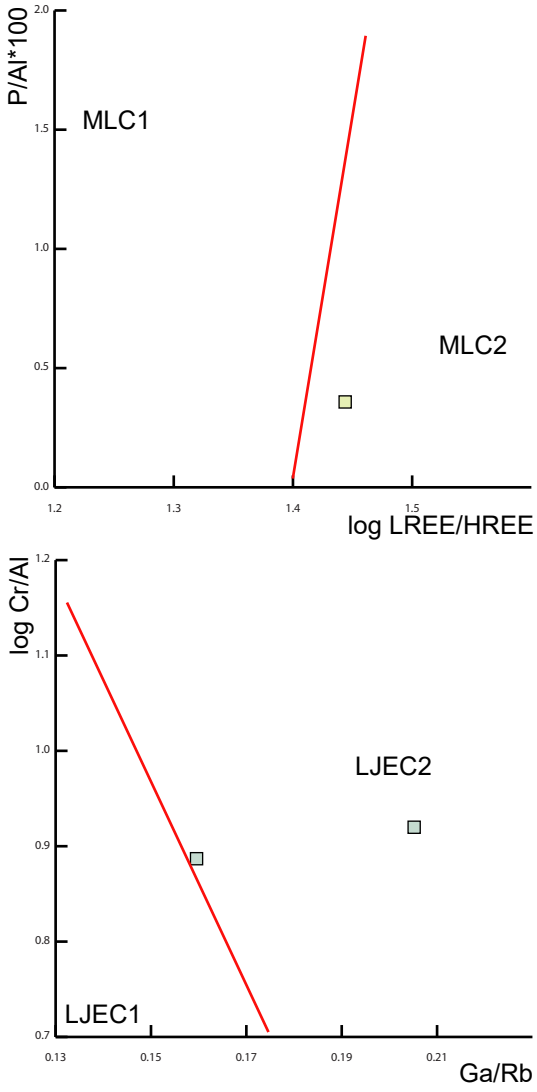

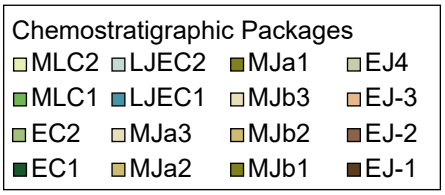

Figure A5.55. Claystone-based binary diagrams distinguishing the chemostratigraphic packages encountered at outcrop along South Mandawa Transect-12: samples colour coded by the chemostratigraphic assignment made in this thesis.

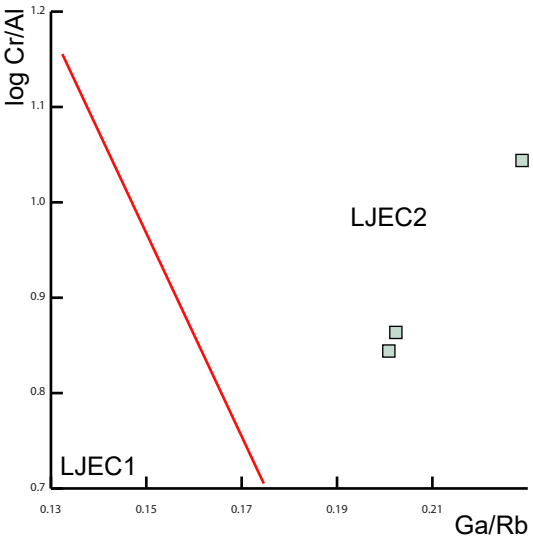

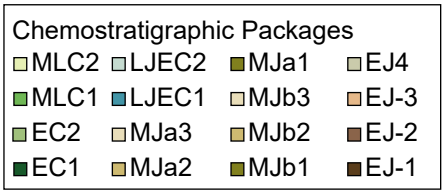

APPENDIX 6: RECOGNISING REDOX STATES AND POTENTIAL ORGANIC MATTER-RICH SEDIMENTS IN THE MANDAWA BASIN USING INORGANIC GEOCHEMICAL DATA

Tribovillard *et al.* (2006) consider that employing inorganic geochemical data to determine the redox state of the depositional environment and to recognise sediments that are (or were) organic matter-rich should only be made if the authigenic hydrogenous control on key elements can be distinguished from detrital controls. Tribovillard *et al.* suggest that the simplest way to determine the degree to which key elements with the potential to be employed for redox and organic matter determinations is to cross plot against Al, which is commonly of detrital origin and usually immobile during diagenesis. If a positive linear relationship is observed, it is likely that the element under inspection has a strongly detrital provenance. Conversely, if there are enrichments in the element without a concomitant Al enrichment, or even an Al decrease, then it is likely that the element under inspection has a dominantly authigenic provenance.

Following this simple procedure, elements Cr, Mo, U, V, Ni and Cu are cross plotted against Al on **Figures A6.1** to **A6.6** for all claystone samples examined in this study. Five of the six elements employed here are the five that Tribovillard *et al.* (2006) suggest are the preferred elements for determining redox and organic matter enrichments. Cr is also included here as it is a key element employed to define part of the chemostratigraphic model in the Mandawa Basin (**Chapter 5**). Therefore, improving the understanding of the mineralogical and geological affinity(s) of Cr is of critical importance in this study to better understand the evolution of the Mandawa Basin during the Mesozoic Era.

Figures A6.1 to **A6.6** reveal that for most claystones under examination, there is a strong positive linear relationship between Al and the six selected trace elements. The result demonstrates that, for most samples, the six elements have a strong detrital, rather than authigenic provenance. Because of the inclusion of many claystones with a strong detrital mineralogy, a positive linear relationship between Al and the six trace elements is to be expected, even in the claystones that may have been deposited in anoxic / euxinic environments. The reason is that in claystones deposited across a range of aquatic environments Al is likely to be diluted by other major elements such as Si in quartz and Ca in carbonate. Both detrital quartz and carbonate are likely to be less

abundant in claystones deposited in low energy, anoxic environments, which means that in these environments, Al and the redox-sensitive elements will be naturally higher in abundance. Thus, when all claystone samples of all depositional environments are compared with each other, a positive linear relationship between Al and the redox-sensitive elements may be apparent. This is not to say that the authigenic signature cannot be identified. Rather that when examining claystone data from a wide range of depositional environments together the authigenic enrichment of key redox-sensitive elements may be subtle. Thus, the simple screening procedure described by Tribovillard *et al.* (2006) to determine the degree to which the key elements have an authigenic, or detrital provenance needs to be used with caution and not arbitrarily applied.

Nevertheless, it is clear on **Figures A6.1** to **A6.6** that various trends exist when the six key redox-sensitive elements in the claystone samples are compared to Al. For example, the degree of the linearity is different in each of the chemostratigraphic sequences and in general the trend lines of all elements skews to the right with each progressively older sequence (i.e. claystones of older sequences are more enriched in the redox-sensitive elements than the younger ones). The chemostratigraphic sequences most consistently enriched in all redox-sensitive elements are Sequences MJa and EJ (**Figures A6.1** to **A6.6**). Moreover, in every element under examination most claystones of Sequence MJa plot on a different alignment to the claystones of Sequence MJb.

Figure A6.1. Per chemostratigraphic sequence Cr vs. Al binary diagrams of the Mandawa Basin claystones.

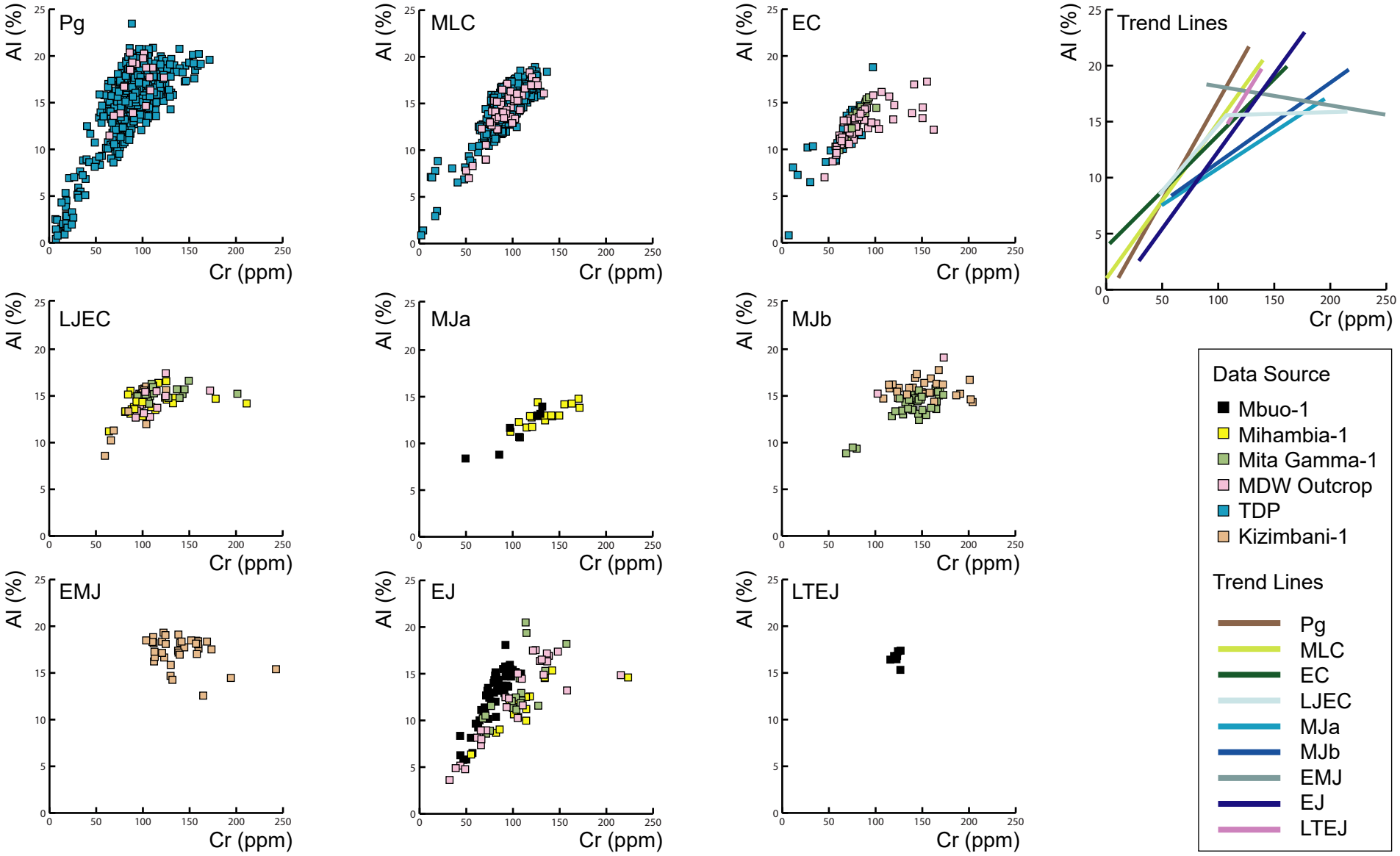

Figure A6.2. Per chemostratigraphic sequence Mo vs. Al binary diagrams of the Mandawa Basin claystones.

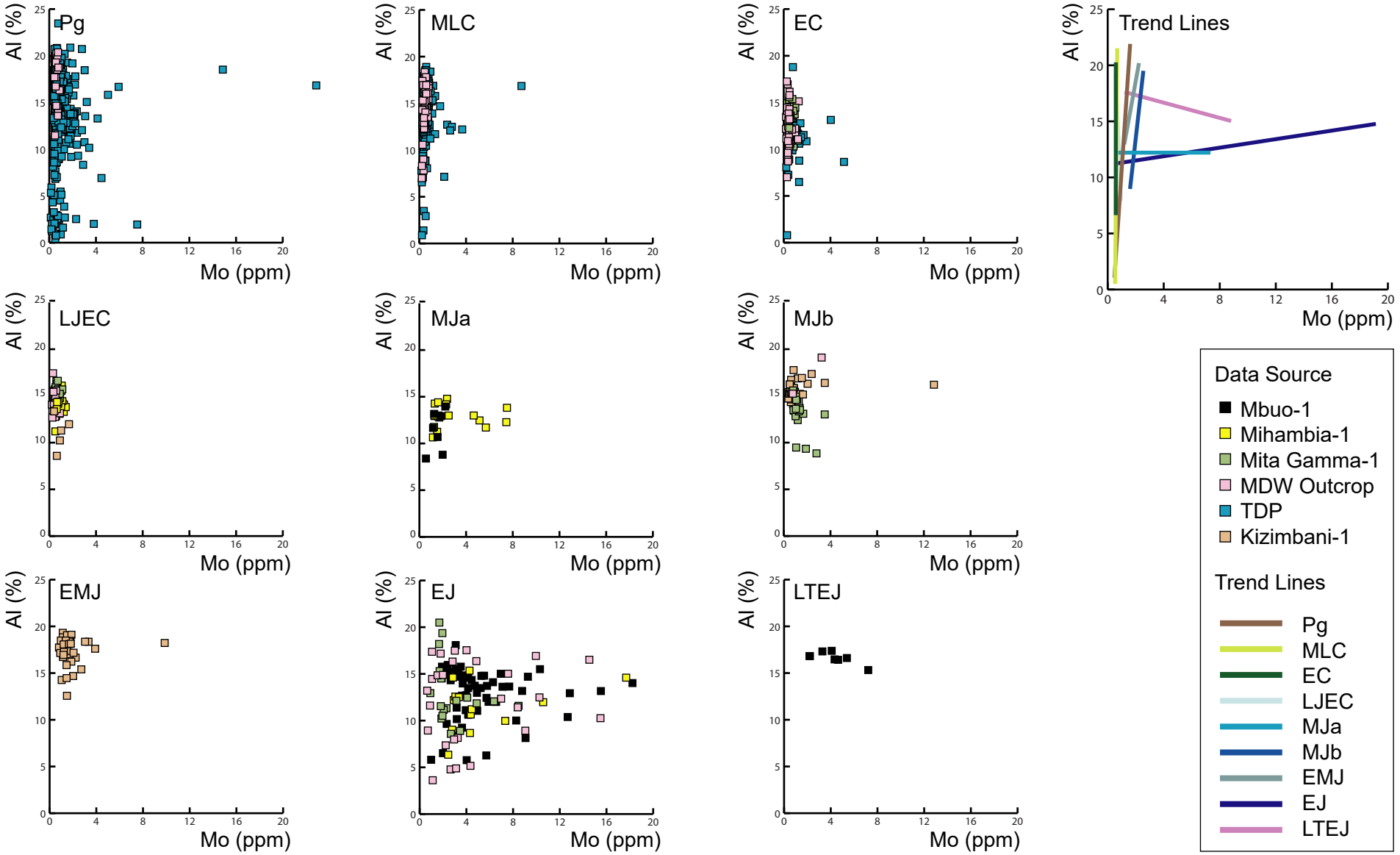

Figure A6.3. Per chemostratigraphic sequence U vs. Al binary diagrams of the Mandawa Basin claystones.

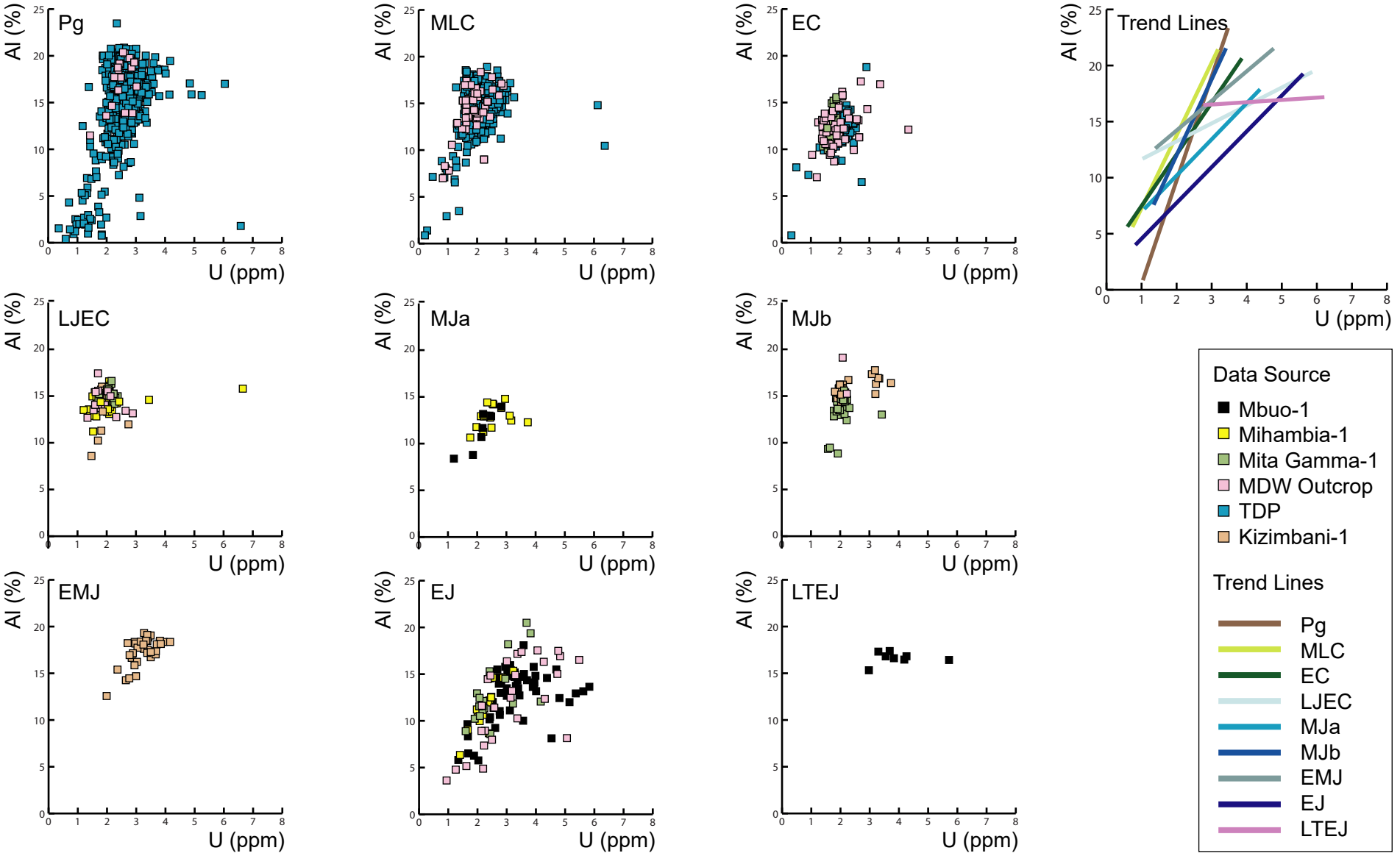

Figure A6.4. Per chemostratigraphic sequence V vs. Al binary diagrams of the Mandawa Basin claystones.

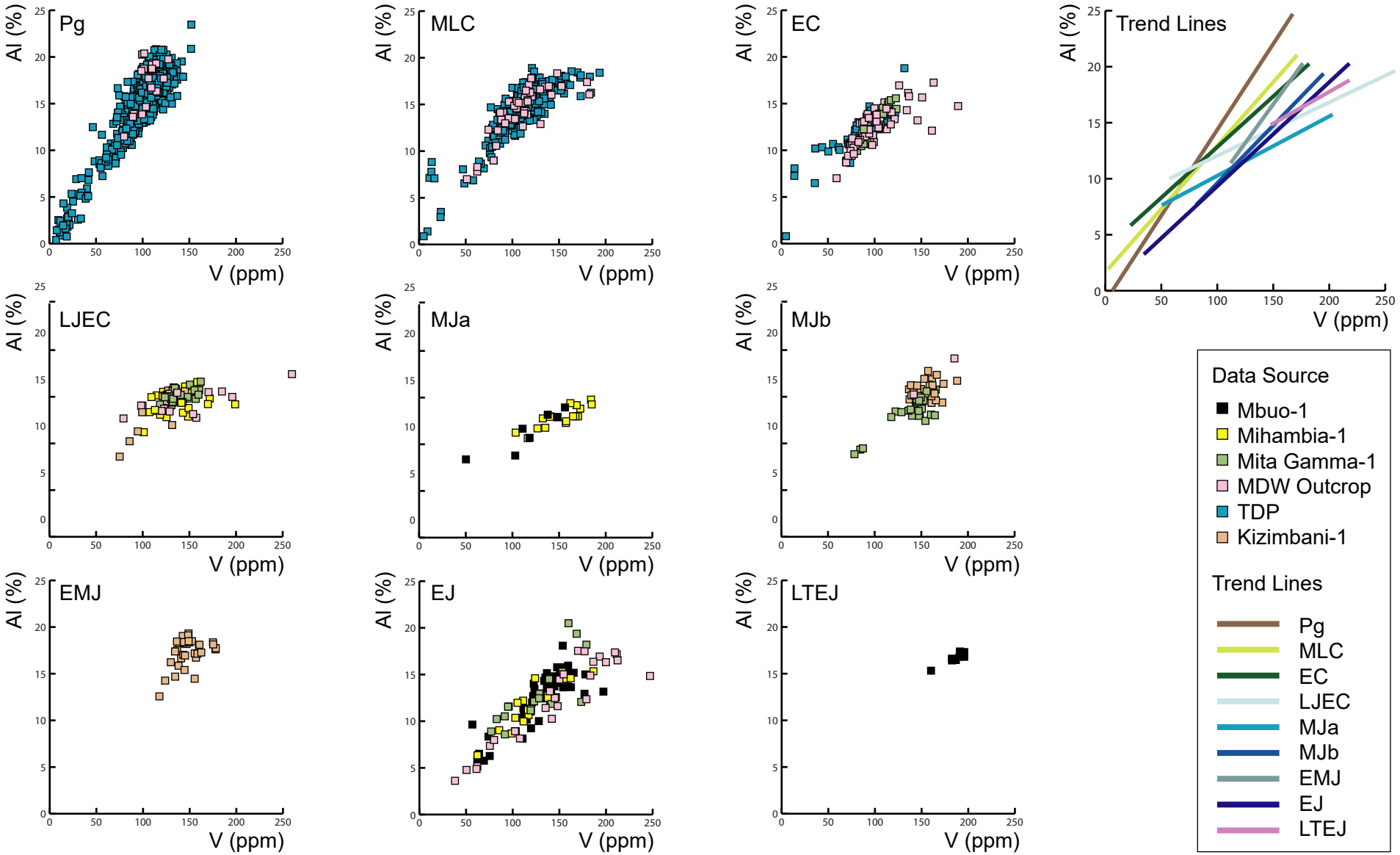

Figure A6.5. Per chemostratigraphic sequence Ni vs. Al binary diagrams of the Mandawa Basin claystones.

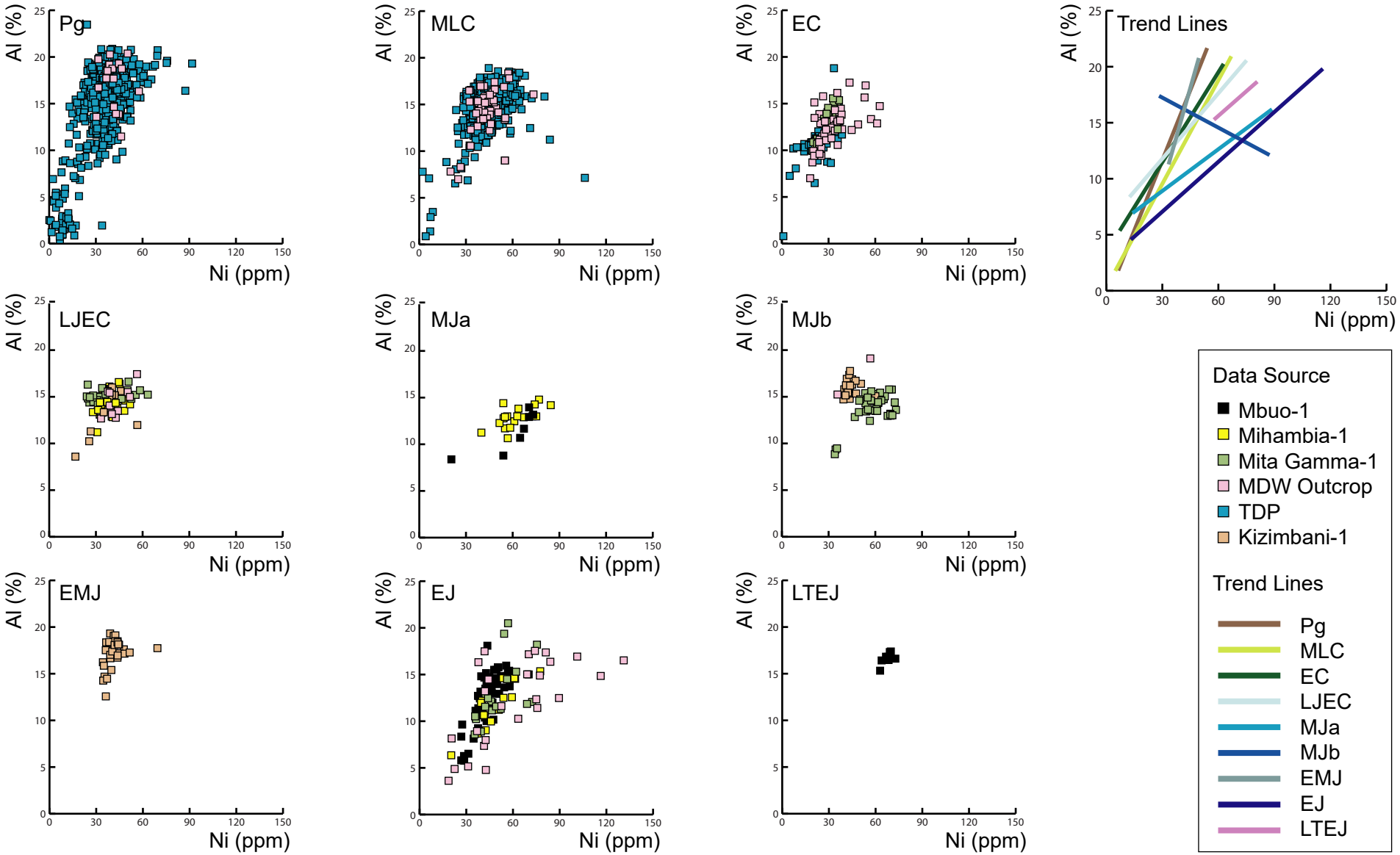

Figure A6.6. Per chemostratigraphic sequence Cu vs. Al binary diagrams of the Mandawa Basin claystones.

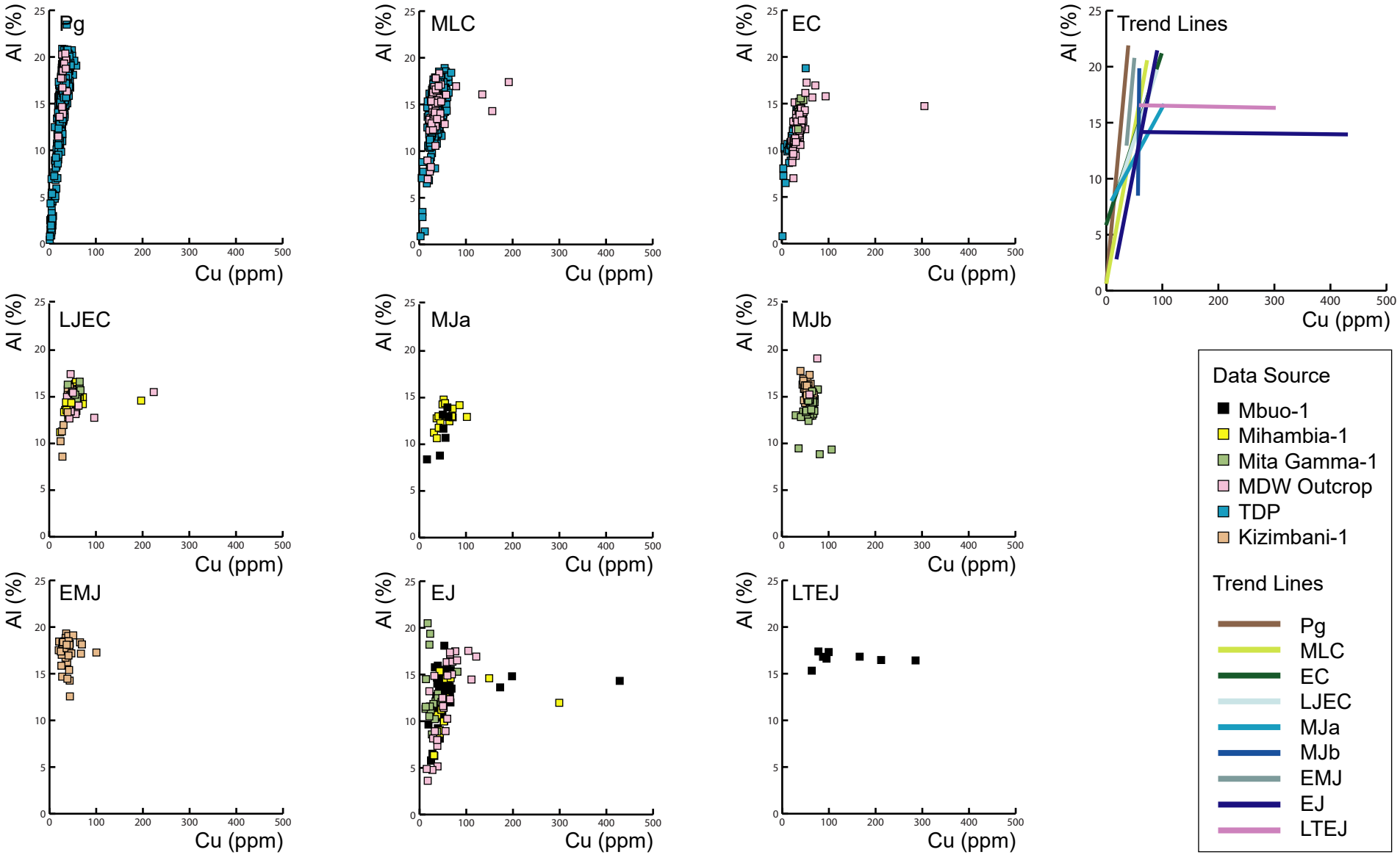

Figure A6.7. Per chemostratigraphic sequence Cu vs. Al binary diagrams of the Mandawa Basin claystones with all samples with >150ppm Cu removed.

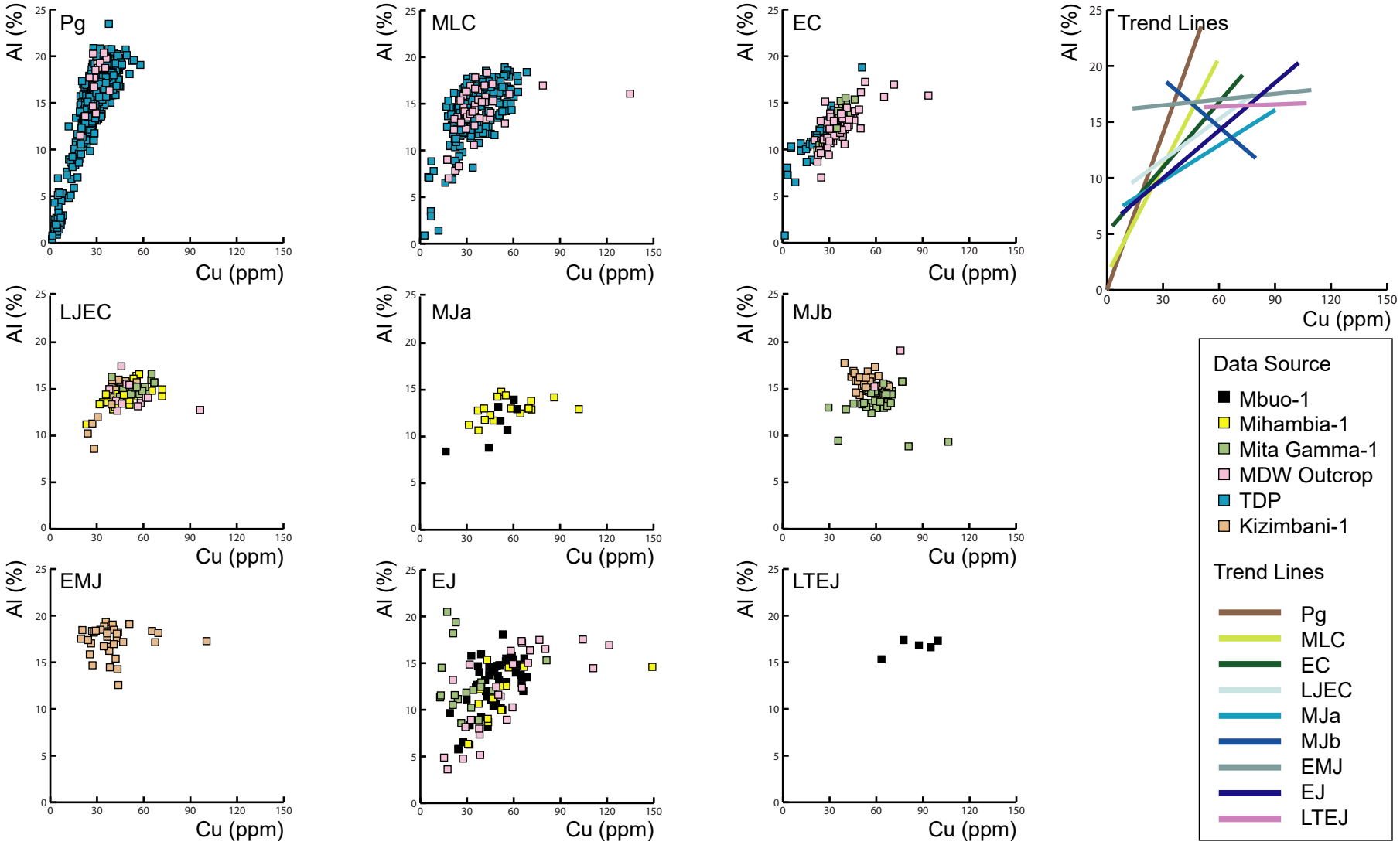

In most chemostratigraphic sequences, Cr exhibits a strong linear relationship with Al. Again, the claystones generally become more enriched relative to Al in progressively older sequences (**Figure A6.1**). In **Chapters 5** and **6**, Cr (indeed, the Cr/Al ratio) is employed to define higher-resolution chemostratigraphic packages within the LJEC Sequence. The Cr vs. Al binary diagram of the LJEC Sequence claystones in **Figure A6.1** exhibits a bimodal linear relationship, with many samples exhibiting a Cr enrichment with no concomitant enrichment in Al. As per the guidelines set out by Tribovillard *et al.* (2006), this type of element enrichment independently of Al is exactly what should be expected if the element under scrutiny has an authigenic provenance. However, and with the possible exception of V, no other redox-sensitive element exhibits a similar enrichment relative to Al within the LJEC Sequence **(Figures A6.1** to **A6.6**). Therefore, it is likely that the Cr enrichments may be related to geological controls other than authigenic enrichment during anoxic / euxinic conditions and are probably related to source area composition of the detrital material in the hinterland. As such, Cr cannot be confidently used for determining redox states within the Mandawa Basin.

Two elements that appear to demonstrate a degree of authigenic enrichment relative to Al are Mo and U (**Figures A6.2** and **A6.3**). The enrichments are largely restricted to claystones in Sequences MJa, MJb, EJ and LTEJ, although a few claystone samples in Sequences Pg and MLC are also enriched in both Mo and U. Unlike Mo and U, there do not appear to be any particularly strong enrichments in V relative to Al in the claystones of any chemostratigraphic sequence (**Figure A6.4**). Subtle enrichments are observed in the claystones of Sequences MJa and EJ and to an even lesser extent in the LJEC Sequence. The result may suggest that authigenic enrichments of V have less of an impact on the general abundance of this element than either Mo, or U.

As mentioned in **Section 7.3**, Tribovillard *et al.* (2006) report that Ni and Cu have the potential to be used as tracers for organic matter abundance in sediments and sedimentary rock and can be retained in sediments and sedimentary rock even if the original organic matter that transported these elements has been destroyed. The Ni vs. Al and Cu vs. Al binary diagrams are plotted on

Figures A6.5 and **A6.6**, respectively. Some claystone samples are extremely enriched in Cu (between 200 and 500ppm, whereas most other samples have <150ppm). The Cu enriched samples are present in some claystones of wells Mihambia-1 and Mbuo-1, particularly in Sequences MJa and EJ, as well as some Mandawa Basin outcrop samples assigned to Sequence MJEC (**Figure A6.6**). It is possible that these samples are, or were, enriched in organic matter. However, similar extreme Ni enrichments are not observed in the same (or any) samples (**Figure A6.5**), which may indicate that organic matter is not an influence on these samples. Thus, the extreme enrichments in Cu are considered with a strong degree of caution.

The extremely high Cu values of some claystone samples overpowers the more common Cu vs. Al trends in the rest of the dataset (**Figure A6.6**). With the X axis of the Cu. vs. Al binary diagrams scaled to 500ppm, it is difficult to compare the Cu trends with the Ni trends. However, when the extremely high Cu samples are removed from the diagram and the X axis is re-scaled to 150ppm (**Figure A6.7**), very similar trends in Ni and Cu relative to Al are observed. Very few claystone samples from Sequences Pg or MLC exhibit any Cu and Ni enrichments independently of Al (**Figures A6.5** and **A6.7**). Enrichment in both Ni and Cu relative to Al starts in many claystones of the LJEC Sequence, particularly in wells Mita Gamma-1 and Mihambia-1 and many Mandawa Basin outcrop samples. Once again however, the strongest enrichments in Ni and Cu relative to Al are in the claystones of Sequences MJa and EJ.

In summary, by following the procedure outlined by Tribovillard *et al.* (2006) to determine the suitability of key elements for redox and organic matter determinations and applying to all claystones analysed in the Mandawa Basin, it is observed that the overwhelming majority of claystones have a strong detrital provenance and show little or no enrichments of the key elements under examination relative to Al. Nevertheless, enrichments in Mo, U, Cu and Ni relative to Al are observed in some claystones that may indicate that they were deposited in an anoxic / euxinic marine environment and in association with organic matter. The strongest enrichments in these

elements relative to Al occur in Sequences MJa, EJ and to a lesser extent MJb which suggests that the claystones within these sequences are the most likely candidates to explore for good quality source rocks. Anomalies in some elements are observed, particularly for Cr, the abundance of which is deemed to be controlled by processes other than redox. The conclusion that Cr abundance is probably not influenced by redox conditions was not based on the trends of this element in isolation, rather by comparing its trends to the other redox-sensitive elements, which highlights the necessity to look at multiple element proxies when assessing their geological controls.

Tribovillard *et al.* (2006) report that the trace element composition of organic matter-rich sediments may be diluted by other mineral phases such as carbonate and biogenic Si. Consequently, viable samples may be overlooked if absolute trace element abundances are considered. To negate any effects of trace element dilution by other phases it is common practice to normalise the trace elements to Al, which is considered as an indicator of the aluminosilicate fraction of the sediment and is regarded as being diagenetically immobile (Tribovillard *et al.*). Taking the concept of normalisation further, enrichment factors (EF) of the element(s) under investigation can be employed to determine their abundance (enrichment) in a sample compared to a standard claystone reference geochemical dataset (also known as 'average shale'), the elements of which have also been normalised. Put simply, the EF equation is as follows:

$$(\text{Element}_{\text{sample}} / \text{Al}_{\text{sample}}) / (\text{Element}_{\text{average shale}} / \text{Al}_{\text{average shale}})$$

If the EF of any element is greater than 1 then it is regarded as being enriched relative to average shale.

Numerous average shale datasets for claystones have been published (see Gromet *et al.*, 1984; McLennan & Taylor, 1985; Condie, 1993 and McDonough & Sun, 1995). In general the datasets record the average chemical compositions of oxygenated marine grey shale in the sedimentary record, which themselves are interpreted to reflect the average composition of the upper

continental crust. Common average shale datasets include the Post Archaean Australian Shale (PAAS) and the North American Shale Composite (NASC).

Van der Weijden (2002) and Tribovillard *et al.* (2006) highlight potential pitfalls with using average shale datasets to create EF plots. The most pertinent is that the chemical composition of the study area may be somewhat atypical when compared to average shale values, which would potentially lead to over or underestimated EFs for some elements. To address this potential issue, the average values of all elements analysed in the Mandawa Basin claystones have been calculated and compared to both PAAS and NASC on **Figure A6.8**. The figure reveals a good match in most elements between all three sources, which suggests that either PAAS or NASC can be used for calculating EFs. Of the elements under examination in this chapter, Mo demonstrates the greatest difference, with slightly higher values recorded in the Mandawa Basin average shale dataset than PAAS (Mo values are not available for NASC). The higher Mo values in the Mandawa Basin average shale may be due to the fact that all claystone samples have been included in the average, and not just those that were deposited in well oxygenated marine environments. However, if this factor was entirely the cause, then it is likely that U would also be enriched relative to PAAS and NASC, which it is not. Whatever the control(s) it is likely that using PAAS to calculate EFs for the Mandawa Basin claystones will lead to a higher abundance of samples having EF values >1 than perhaps there should be. Nevertheless, PAAS values are employed for this purpose in this study.

As Mo, U, Ni and Cu exhibit the strongest enrichments relative to Al, the EF Mo vs. EF U and EF Ni vs. EF Cu cross plots for all available claystone samples examined in this study are plotted by chemostratigraphic sequence on **Figures A6.9** and **A6.10**. Statistical information relating to the EF plots are presented on **Table A6.1**. In all sequences, there are claystones that are enriched in all four elements relative to PAAS. The percentage of claystones enriched in all four elements are highest in Sequences LTEJ, EJ, MJa and MJb. Mo exhibits the highest enrichment in the

Mandawa Basin claystones relative to PAAS with mean average EF values between 1.7 and 8.5 but decreasing to 1.1 or less in the other four sequences. The mean average EF values for all other elements in all other sequences are around 2 or less and although the decrease is not as extreme as that observed with Mo, average EF values for the other three elements generally decrease in the progressively younger sequences.

Figure A6.8. Comparison of the average element values calculated from all the Mandawa Basin claystone samples and the average shale values of PAAS and NASC.

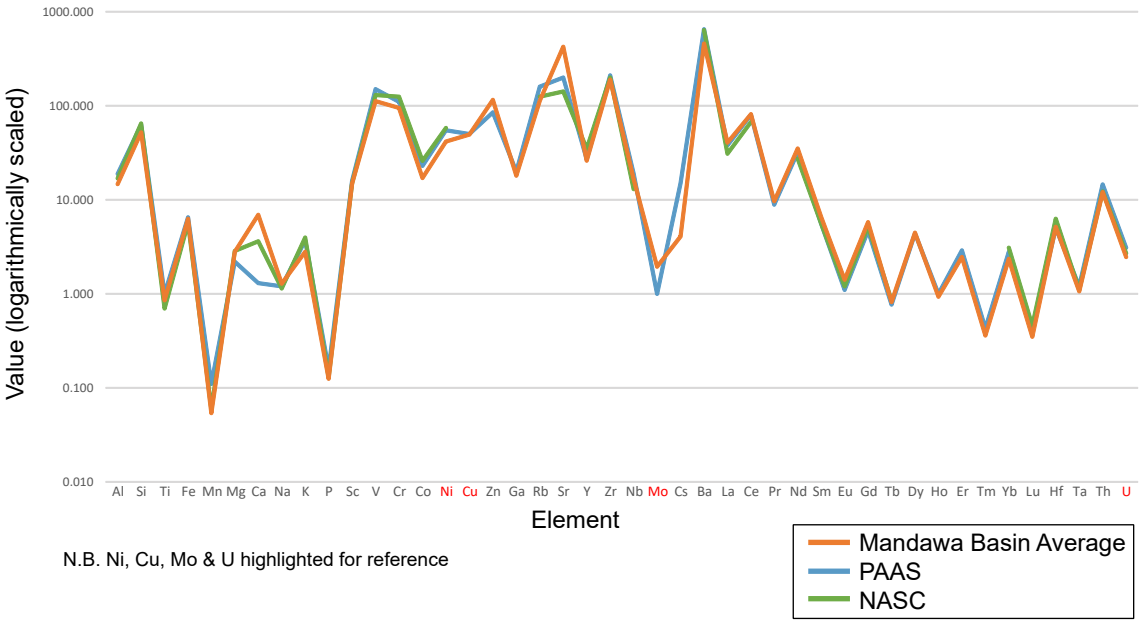

In Sequences LTEJ, EJ, MJa and MJb, a positive linear relationship is observed between the EF Mo vs. EF U values and the EF Ni vs. EF Cu values of the Mandawa Basin claystones (**Figures A6.9** and **A6.10**). These are the only sequences where positive linear relationships in all four elements are observed. A positive linear relationship between the EF Ni and EF Cu values of the Sequence Pg, MLC and EC claystones is observed (**Figure A6.10**), but a similar relationship is not observed between Mo and U in these sequences (**Figure A6.9**). Indeed, within Sequences Pg, MLC and EC, there appears to be a largely bimodal relationship between Mo and U where enrichments >1 occur, with some claystones being enriched in one element, but not the other (and vice versa).

Figure A6.9. Per chemostratigraphic sequence EF Mo vs. EF U binary diagrams of the Mandawa Basin claystones.

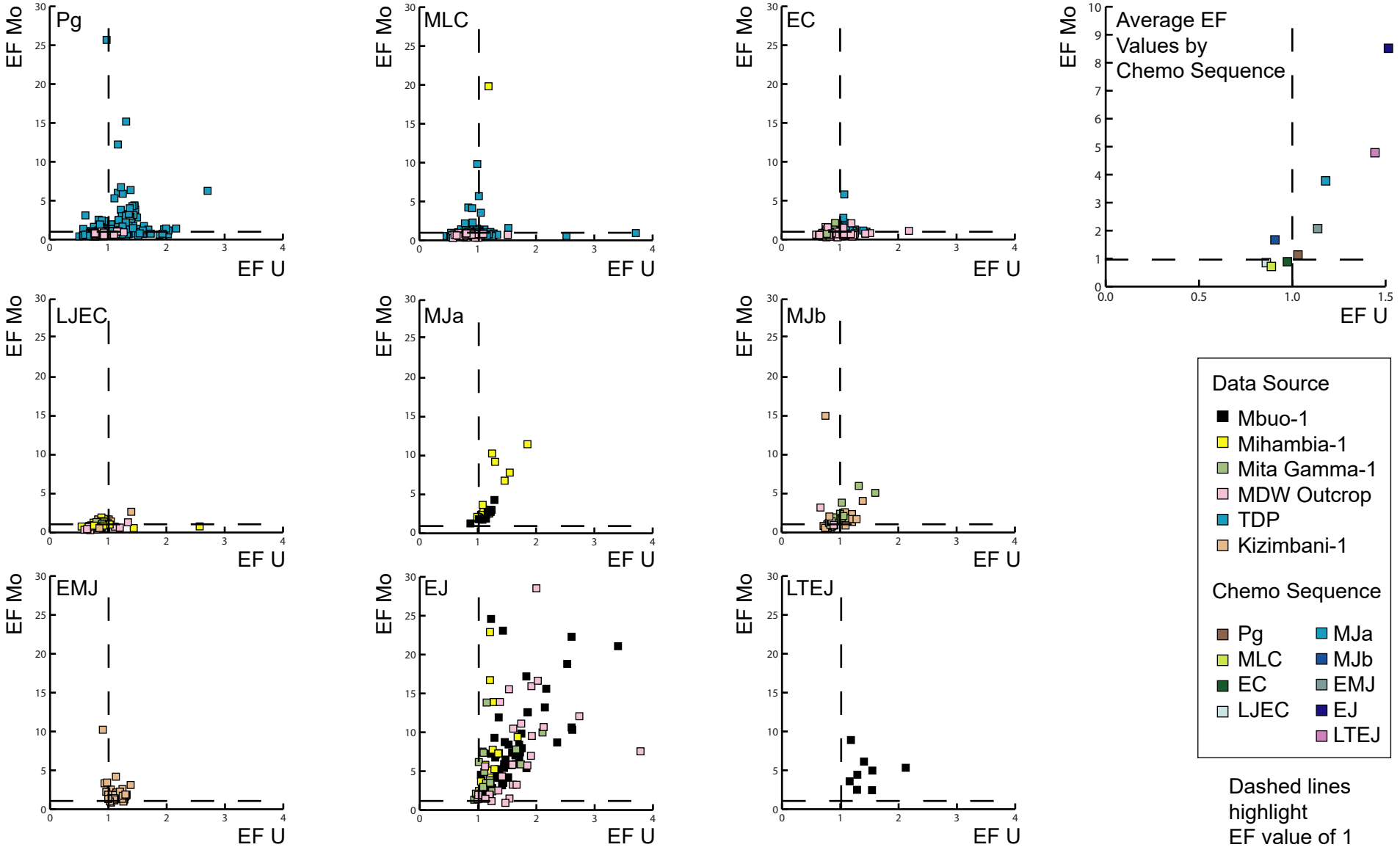

Figure A6.10. Per chemostratigraphic sequence EF Ni vs. EF Cu binary diagrams of the Mandawa Basin claystones.

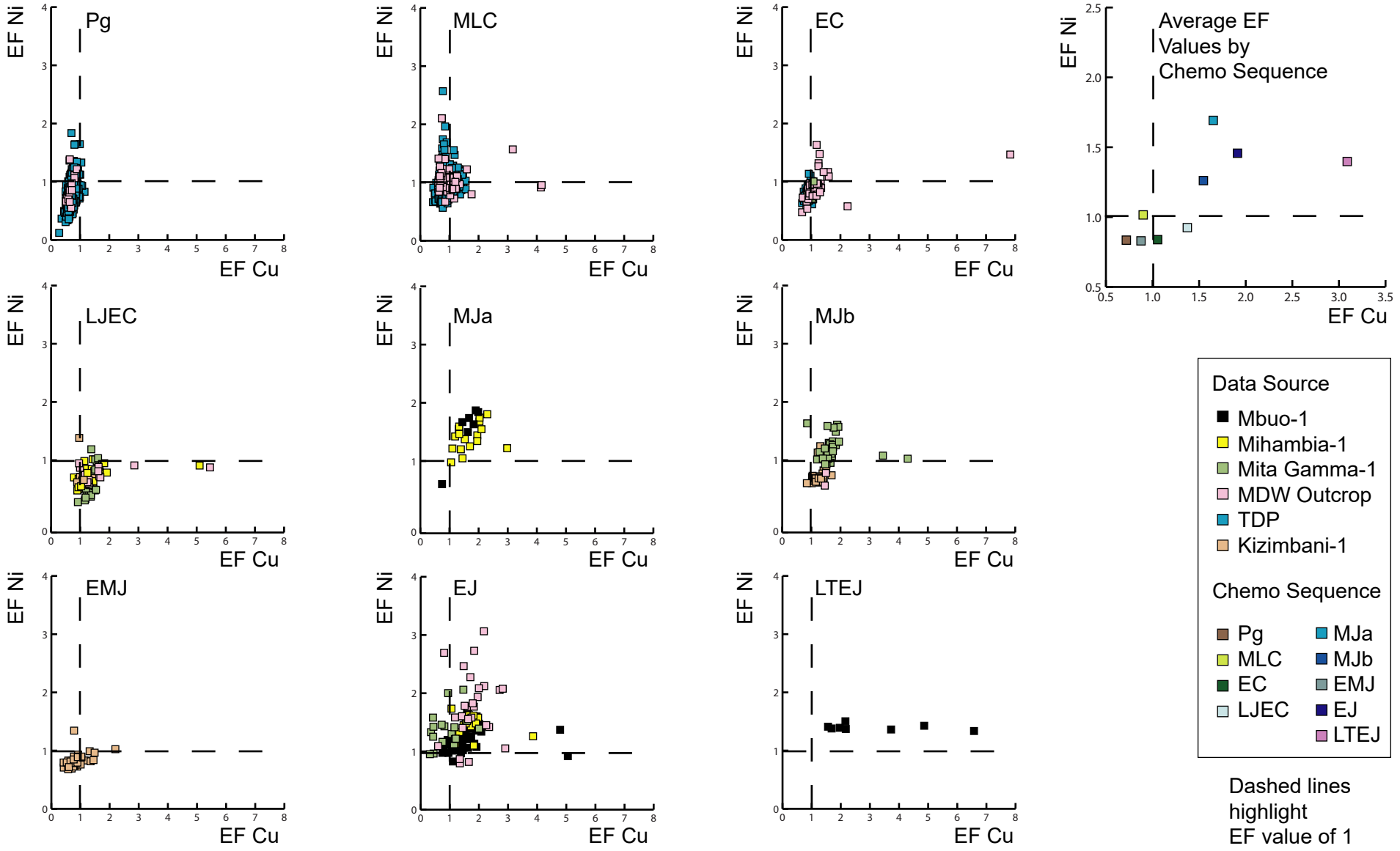

Table A6.1. Per sequence statistical information derived from the EF of Mo, U, Ni and Cu.

Element	Chemostratigraphic Sequence	No. of samples	No. samples with EF values <1	% samples with EF values <1	Max EF Value	Min EF Value	Mean Average EF Value
Mo	Pg	581	169	29	25.6	0.3	1.1
	MLC	412	32	8	9.8	0.3	0.7
	EC	142	35	25	5.8	0.3	0.9
	LJEC	86	20	23	2.7	0.3	0.9
	MJa	25	25	100	11.5	1.3	3.8
	MJb	68	43	63	15.0	0.5	1.7
	EMJ	35	33	94	10.0	0.9	2.1
	EJ	112	111	99	93.0	0.9	8.5
	LTEJ	8	8	100	8.9	2.5	4.8
U	Pg	581	279	48	2.7	0.5	1.0
	MLC	412	99	24	3.7	0.5	0.9
	EC	142	62	44	2.2	0.6	1.0
	LJEC	86	10	12	2.5	0.5	0.9
	MJa	25	23	92	1.9	0.9	1.2
	MJb	68	14	21	1.6	0.7	0.9
	EMJ	35	29	83	1.4	0.9	1.1
	EJ	112	109	97	3.8	0.9	1.5
	LTEJ	8	8	100	2.1	1.2	1.4
Ni	Pg	581	125	22	1.8	0.1	0.8
	MLC	412	195	47	2.7	0.6	1.0
	EC	142	13	9	1.6	0.5	0.8
	LJEC	86	28	33	1.6	0.5	0.9
	MJa	25	24	96	2.0	0.8	1.7
	MJb	68	47	69	1.9	0.8	1.3
	EMJ	35	2	6	1.3	0.7	0.8
	EJ	112	102	91	8.0	0.8	1.5
	LTEJ	8	8	100	1.5	1.3	1.4
Cu	Pg	581	6	1	1.1	0.3	0.7
	MLC	412	98	24	4.2	0.4	0.9
	EC	142	62	44	7.8	0.7	1.1
	LJEC	86	73	85	5.5	0.8	1.4
	MJa	25	24	96	3.0	0.7	1.7
	MJb	68	66	97	4.3	0.8	1.5
	EMJ	35	9	26	2.2	0.4	0.9
	EJ	112	96	86	26.0	0.3	1.9
	LTEJ	8	8	100	6.6	1.6	3.1

REFERENCES

Andò, S. & Garzanti, E. 2013. Raman spectroscopy in heavy-mineral studies. In: Scott, R. A., Smyth, H. R., Morton, A. C. & Richardson, N. (eds), Sediment Provenance Studies in Hydrocarbon Exploration and Production. *Geological Society of London Special Publication,* 386.

Andrews, D. L., 2017. Rayleigh scattering and Raman effect, theory. In: Lindon, J. C. (eds), Encyclopedia of Spectroscopy and Spectrometry. *Academic Press, Oxford,* 924 - 930.

Carvajal-Ortiz, H., & Gentzis, T. 2015. Critical considerations when assessing hydrocarbon plays using Rock-Eval pyrolysis and organic petrology data: data quality revisited. *International Journal of Coal Geology*, 152, 113 - 122.

Chou, I-M., & Wang, A., 2017. Application of laser Raman micro-analyses to Earth and planetary materials. Journal *of Asian Earth Sciences*, 145, 309 - 333.

Gromet, P. L., Dymek, R. F., Haskin, L. A., & Korotev, R. L. 1984. The "North American shale composite": its compilation, major and trace element characteristics. *Geochemica et Cosmochemica Acta*, 48, 2469 - 2482.

Jarvis, K. E., 1990. A critical evaluation of two sample preparation techniques for low-level determination of some geologically incompatible elements by inductively coupled plasma-mass spectrometry. *Chemical Geology,* 83, 89 - 103.

Jarvis, I. & Jarvis, K. E., 1992a. Inductively coupled plasma-atomic emission spectrometry in exploration geochemistry. In: Hall, G. E. M. (ed.), Geoanalysis. *Journal of Geochemical Exploration,* 44, 139 - 200.

Jarvis, I. & Jarvis, K. E., 1992b. Plasma spectrometry in the earth sciences, techniques, applications and future trends. In: Jarvis, I. & Jarvis, K. E. (eds), Plasma Spectrometry in the Earth Sciences. *Chemical Geology*, 95, 1 - 33.

John, N., & George, S. 2017. Raman spectroscopy. In: Thomas, S., Thomas, R., Zachariah, A., K., & Mishra, R. K. (eds), Spectroscopic Methods for Nanomaterials Characterization. *Elsevier*, 95 - 127.

Kamber, B. S., 2009. Geochemical fingerprinting: 40 years of analytical development and real world applications. *Applied Geochemistry*, 24, 1074 - 1086.

Lafargue, E., Espitalié, J., Marquis, F., & Pillot, D., 1998. Rock-Eval 6 applications in hydrocarbon exploration, production and in soil contamination studies. *Institut Français du Pétrole*, **3**, 421 - 437.

Longerich, H. P., Jenner, G. A., Fryer, B. J. & Jackson, S. E., 1990. Inductively coupled plasma-mass spectrometric analysis of geological samples: a critical evaluation based on case studies. *Chemical Geology*, 83, 105 - 118.

Mange, M. A., & Maurer, H. F. W., 1992. Heavy minerals in colour. *Springer*. 101-124.

McDonough, W. F., & Sun, S. -S. 1995. The composition of the Earth. *Chemical Geology* 120, 223 - 253.

McLennan, S. M., & Taylor, S. R. 1985. The continental crust: its composition and evolution. *Blackwell*. 9 - 52.

Morton, A. C. & Hallsworth, C., 1994. Identifying provenance-specific features of detrital heavy mineral assemblages in sandstones. *Sedimentary Geology*, 90, 241 - 256.

Nasdala, S. M., Smith, D. C., Kaindl, R., & Ziemann, M. A., 2004. Raman spectroscopy: analytical perspectives in mineralogical research. In: Beran, A., & Libowitzky, E. (eds), Spectroscopic Methods in Mineralogy. *European Mineralogical Union Notes in Mineralogy*, 6, 281 - 343.

Norwegian Petroleum Directorate, Norsk Hydro, Statoil, Geolab Nor, & Sintef Petroleum Research, 2000. Nigoga - The Norwegian industry guide to organic geochemical analysis. www.npd.no/Global/Norsk/5-Regelverk/Tematiskeveiledninger/Geochemicalanalysis_e.PDF

Peters, K. E. 1986. Guidelines for evaluating petroleum source rock using programmed pyrolysis. *American Association of Petroleum Geologists Bulletin*, 70 (3) 318 - 329.

Peters, K. E., Walters, C. C., & Moldowan, J. M. 2005. The Biomarker Guide Volume 1: Biomarkers and isotopes in the environment and human history (2nd ed.). *Cambridge University Press* 3 - 118.

Potts, P. J., & Webb, P. C., 1992. X-ray fluorescence spectrometry. *Journal of Geochemical Exploration*, 44, 251 - 296.

Totten, M. W. & Hanan, M. A. 2007. Heavy minerals in shales. In: Mange, M. A., & Wright, D. T. (eds) 2007. Heavy minerals in use. *Developments in sedimentology*, 58, 323 - 341. Elsevier.

Tribovillard, N., Alego, T. J., Lyons, T., & Riboulleau, A. 2006. Trace metals as paleoredox and paleoproductivity proxies: an update. *Chemical Geology* 232, 12 - 32.

Van Der Weijden, C. H. 2002. Pitfalls of normalisation of marine geochemical data using a common divisor. *Marine Geology*, 184, 167 - 187.

Waples, D. W. 2013. Geochemistry in petroleum exploration. *Reidel*. 89 - 90.